HYDRODYNAMIC PARAMETERS OF MICRO POROUS MEDIA FOR STEADY AND OSCILLATORY FLOW: APPLICATION TO CRYOCOOLER REGENERATORS

A Dissertation
Presented to
The Academic Faculty

by

Jeesung Jeff Cha

In Partial Fulfillment
of the Requirements for the Degree
Doctor of Philosophy in the
School of Mechanical Engineering

Georgia Institute of Technology
August 2007

HYDRODYNAMIC PARAMETERS OF MICRO POROUS MEDIA FOR STEADY AND OSCILLATORY FLOW: APPLICATION TO CRYOCOOLER REGENERATORS

Approved by:

Dr. S. Mostafa Ghiaasiaan, Advisor
School of Mechanical Engineering
Georgia Institute of Technology

Dr. Kurt D. Pennell
School of Civil and Environment Engineering
Georgia Institute of Technology

Dr. Prateen V. Desai
School of Mechanical Engineering
Georgia Institute of Technology

Dr. Jeremy P. Harvey
Reservoir Completion
Schlumberger Company

Dr. Sheldon M. Jeter
School of Mechanical Engineering
Georgia Institute of Technology

Dr. Carl S. Kirkconnell
Opto-Mechanical Department
Raytheon Space and Airborne Systems

Date Approved: June, 27, 2007

Dedicated to my parents, Jung E and Myung Hwa

ACKNOWLEDGEMENTS

I am most indebt to my advisor Dr. S. Mostafa Ghiaasiaan for taking a chance on me and picking me in spring of 2003 to perform cryocooler research at Georgia Institute of Technology. With his guidance and support I was able to successfully finish my graduate studies. I have been very fortunate to work with Dr. Ghiaasiaan and any individual or graduate student who works with/for him in the future is very fortunate. G.W.W School of Mechanical Engineering is very fortunate to have Dr. Ghiaasiaan as a dedicated professor. Dr. Prateen V. Desai, a retired ME emeritus professor, has been a vital contributor to my research for the past four years. His support and endless advices have provided many solutions to my research problems. Dr. Carl S. Kirkconnell of Raytheon Space and Airborne Systems deserves special thanks for continuously motivating me in the field of cryocoolers and supporting me through GT and Raytheon Cryocooler Research Foundation. Dr. Kirkconnell's vision of future cryocoolers and Dr. Ghiaasiaan's vision of fundamental research together has put GT cryogenic research laboratory on the same level as other well recognized cryocooler research laboratories in the country.

Dr. Jeremy P. Harvey, a friend, deserves my biggest sincere thanks. During my rough times, he has been available either by phone or in person to offer me tremendous amounts of help. This research would have not been possible without your advice and supports. Thanks Jeremy.

I would also like to thank my other committee members Dr. Sheldon M. Jeter of Mechanical Engineering Department and Dr. Kurt D. Pennell of Civil and Environment Engineering Department for sharing their breadth of expertise.

In ME School Ms. Glenda Johnson and Ms. Terri Keita deserve recognition for guiding me through a long graduate program. Mr. John Graham, the head of the ME Machine Shop also deserves recognition for being so kind and allowing me to work in his machine shop and fabricating my experimental parts. Talking to you about life and SEC football was very enjoyable.

Outside of academic world, there are a few colleagues whom I met through Raytheon summer internships that deserve thanks. They are William “Bill” Croft, Thomas Pollack, and Melina Pillar.

I would also like to thank Cryogenic Engineering Conference Timmerhaus Scholarship Fund, for partially supporting my research at Georgia Institute of Technology.

I also have been fortunate to work with a couple of graduate student in the GT cryogenic research laboratory. They are Mr. Will Clearman and Mr. Ted Conrad, the next torch bearer for the GT Cryogenic Laboratory (GTCL). Outside of GTCL there are few ME graduate students that deserve special thanks. They are Keunhan Park, Hyunjin Lee, and Bongjae Lee.

The people whom I am most thankful to are members of my family. Especially my parents Jung E and Myung Hwa, and my brother and sister, Jason and Jessica, through their endless supports and advices I was able to successfully finish my graduate studies.

TABLE OF CONTENTS

LIST OF TABLES

Page

LIST OF FIGURES

Page

NOMENCLATURE

Variables

A	Length of pore unit cell (m), flow area (m^2)
A_f	Regenerator flow area, $A\alpha$, (m^2)
a_λ	Surface area per unit volume (m^{-1})
A_{int}	Total interface area between the fluid and solid (m^2)
B	Height of square rod (m)
c	Specific heat $(J/kg\bullet^o K)$
$\overline{\overline{C}}$	Fluent's inertial resistance coefficient tensor (m^{-1})
$\overline{\overline{c_f}}$	Forchheimer inertial coefficient tensors $(--)$
$c_{f,j}$	Directional Forchheimer inertial coefficient $(--)$
d	Diameter of regenerator (m)
$d\vec{A}$	Vector oriented outward from fluid side (m^2)
e	Fluid total energy per unit volume (J/m^3)
f	Friction factor $(--)$, Frequency (Hz)
G_1, G_2	Integration constant
h	Enthalpy (J/kg)
H	Convective heat transfer coefficient $(W/m^2\bullet^o K)$
I	Unit tensor (--)

k	Thermal conductivity $(W/m\bullet^{o}K)$
$\overline{\overline{K}}$	Darcy permeability tensors, (m^2)
K_j	Directional Darcy permeability, (m^2)
l	Length of annular regenerator (m)
m	Total mass of regenerator (kg)
$\dot{m}$	Mass flow rate (kg/s)
N_k	Axial conductivity enhancement factor $(--)$
P	Microscopic fluid pressure (N/m^2)
r	Radial coordinate (m)
T	Local instantaneous temperature, Volume average temperature in porous media (^{o}K)
$T'\vec{u}'$	Dispersion vector
t	Time *(s)*
$\vec{u}$	Local instantaneous velocity vector, Volume average intrinsic velocity (m/s)
V	Volume (m^3)
x	Axial coordinate (m)
$\langle\ \rangle$	Volume average quantity
$\langle\ \rangle^{f}$	Fluid volume average quantity
$\|\ \|$	Magnitude of the quantity

Notations

CHX	Cold heat exchanger
ff	Friction factor
HX1	Compressor side warm heat exchanger
HX2	Buffer volume side compressor heat exchanger
i	1,2
n	1, 2, 3
*Pc	Inner diameter location pressure of annular regenerator
P_1	Regenerator inlet pressure
P_2	Regenerator exit pressure
P_3	Buffer volume pressure
V1	Valve 1
V2	Valve 2
RTS1	Axial test apparatus regenerator housing module
RTS2	Axial test apparatus regenerator housing module for micro machined disks

Symbols

α	Regenerator porosity (--)
β	Fluent's viscous resistance permeability tensor, (m^2)
η_s	Solid tortuosity
μ	Dynamic viscosity $(kg/m \cdot \mathrm{s})$
θ	Macroscopic flow angle

ρ	Density (kg/m^3)
$\bar{\bar{\tau}}$	Stress tensors (N/m^2)
ξ	Macroscopic flow direction in a lattice unit cell (m)
ψ	Height of pore unit cell (m)
∇	Gradient operator
Γ_n	Pressure amplitude (N/m^2)
Δ_n	Pressure phase angle $(Degree)$

Subscripts

annular	Annular porous medium
atm	Atmospheric conditions
axial	Axial direction
c	Copper heat exchangers
comp	Compressor heat rejection
disp	Dispersion
e	Effective, regenerator exit location
f	Fluid
H	High pressure
i	Regenerator inlet location, inner
L	Low Pressure
p	Local instantaneous fluid pressure
o	Outer

osc	Oscillating flow conditions
r, x	Radial and axial coordinate directions
radial	Radial direction
refrig	Refrigeration
s	Solid
Solid cylinder	Cylindrical regenerator
steady	Steady flow condition
t	Turbulent
tort	Tortuosity
total	Total volume

SUMMARY

Pulse Tube Cryocoolers (PTC) are a class of rugged and high-endurance refrigeration systems that operate without a moving part at their low temperature ends, and are capable of easily reaching *120* ^{o}K. These devices can also be configured in multiple stages to reach temperatures below 10 ^{o}K. PTCs are particularly suitable for applications in space, missile guiding systems, cryosurgery, medicine preservation, superconducting electronics, magnetic resonance imaging, weather observation, and liquefaction of nitrogen. Although various designs of PTCs have been in use for a few decades, they represent a dynamic and developmental field. PTCs ruggedness comes at the price of relatively low efficiency, however, and thus far they have been primarily used in high-end applications. They have the potential of extensive use in consumer products, however, should sufficiently higher efficiencies be achieved. Intense research competition is underway worldwide, and newer designs are continuously introduced. Some of the fundamental processes that are responsible for their performance are at best not fully understood, however, and consequently systematic modeling of PTC systems is difficult. Among the challenges facing the PTC research community, besides improvement in terms of system efficiency, is the possible miniaturization (total fluid volume of few cubic centimeters (cc)) of these systems.

The operating characteristics of a PTC are significantly different from the conventional refrigeration cycles. A PTC implements the theory of oscillatory compression and expansion of the gas within a closed volume to achieve desired refrigeration. Regenerators and pulse tubes are often viewed as the two most complex

and essential components in cryocoolers. An important deficiency with respect to the state of art models dealing with PTCs is the essentially total lack of understanding about the directional hydrodynamic and thermal transport parameters associated with periodic flow in micro-porous structures. This is particularly troubling with regards to the regenerator, where friction and thermal non-equilibrium between the fluid and the structure play crucial roles. Little attention has been paid to this issue primarily because of the difficulty of experimental measurements. Multi-dimensional modeling of a regenerator is very complex and requires knowledge about the anisotropic hydrodynamic parameters in various components, in particular the regenerator.

In view of the above, this investigation was aimed at: a) experimental measurement and correlation of the steady and periodic flow directional Darcy permeability and Forchheimer's inertial hydrodynamic parameters for some widely-used regenerator fillers; b) system-level parametric CFD-based analyses of entire PTC systems; and c) a preliminary CFD-based assessment of the effect of direct and linear scale-down of current Inertance Tube Pulse Tube Cryocooler (ITPTCs) on their thermal performance.

Modular experimental apparatuses were designed and built for the measurement of pressure drops across five different and widely-used regenerator fillers, under steady-state and steady periodic flow conditions. Separate test sections were used so that the pressure drops in axial and lateral directions could be measured. The fillers that were investigated included 325 mesh stainless steel screens, 400 mesh stainless steel screens, sintered 400 mesh stainless steel screens, stainless steel metal foam, and stacked nickel micro-machined disks.

The parametric effects that were addressed in the experiments included the porosity in the range of 26.8% to 69.2 %, and frequency in the range of 5 Hz to 60 Hz for the periodic flow tests. A CFD-assisted method was developed, which allowed for obtaining the directional permeability and Forchheimer coefficients from the experimental data in a rigorous manner and without any arbitrary assumption.

Using the Fluent code, parametric CFD analyses were performed in which entire ITPTC systems were simulated. The simulations were initiated from room temperature thermal equilibrium, and were continued until steady-periodic conditions were obtained. It was shown that the CFD simulations, when correctly set up, can provide valuable information (multi-dimensional flow effects and transient local instantaneous thermo-fluidic properties), about the component and system-level phenomena. The hydrodynamic and thermal performances of the five tested regenerator filler matrices were then compared based on CFD-assisted system-level simulations. The hydrodynamic parameters representing steady and periodic flow conditions in the five tested regenerator filler matrices were also compared. It was thus shown that the hydrodynamic parameters representing steady flow are in general different from the hydrodynamic parameters associated with periodic flow (e.g. oscillatory to steady friction factor ratio f_{osc} / f_{steady} of 1.3 was obtained at Reynolds number of approximately 29 for SS 325 mesh regenerator) .

The effect of direct miniaturization on the performance of a linearly-configured ITPTC system was also examined in a preliminary, CFD-assisted analysis. It was shown that direct and linear miniaturization, when all the dimensions of a current conventional-

scale ITPTC system are proportionately reduced, leads to significant deterioration of the performance of the cryocooler.

CHAPTER 1

INTRODUCTION

1.1 Introduction Remarks and Objectives

Cryogenics is the branch of physics that studies the phenomena that occur at extremely low temperatures, close to the lowest theoretically attainable temperature (absolute zero, 0 ^{o}K, or -273.15 ^{o}C, or -459.67 ^{o}F). In engineering, cryogenics can be best described as an application which operates in the temperature range from *0* ^{o}K to *120* ^{o}K.

One system that can provide cryogenic temperatures in engineering applications is the Pulse Tube Cryocooler (PTC). PTCs are a class of rugged and high-endurance refrigeration systems that operate without a moving part at their cold end, and are capable of easily reaching *120* ^{o}K or lower. These devices can also be configured in multiple stages to reach temperatures below *10* ^{o}K. PTCs are particularly suitable for applications in space, missile guiding systems, cryosurgery, superconducting electronics, magnetic resonance imaging, liquefaction of nitrogen, and liquid nitrogen transportation.

Although various designs of PTCs have evolved and been in use for a few decades, the field of pulse tube cryocooling represents a dynamic and developmental field. What makes PTCs particularly attractive is that they are extremely rugged since they do not have a moving part on their cold end. This ruggedness makes PTCs particularly suitable for space and military applications. It however comes at the price of

relatively low efficiency. Thus far, they have been primarily used in high-end applications. They have the potential of widespread use in consumer products, should sufficiently higher efficiencies be achieved. Intense international research and development, and indeed competition, are underway in the field of pulse tube cryocoolers, and newer designs are continuously introduced. Interestingly, despite extensive research in the past, some of the fundamental processes that are responsible for PTC performance are not fully understood, and consequently systematic modeling of PTC systems has been difficult. Early models have primarily been lumped parameter-type, and semi-mechanistic models based on the numerical solution of relevant differential conservation equations have been reported only in the last several years. Very recently, CFD analyses of entire PTC systems have been successfully performed and demonstrated.

The advent of miniature sensors and engineering systems has now introduced a new and exciting potential field of application for rugged cryocoolers. Thus, among the challenges facing the PTC research community, besides improvement in terms of system efficiency, is the possible miniaturization of these systems.

The generic structures of PTCs and their operation principles will be discussed in the next chapter. Generally speaking, PTCs are typically composed of a compressor, heat exchangers, a regenerator, a pulse tube, one or more orifice valves or an inertance tube, and a buffer volume. The operating characteristics of a PTC are significantly different from the conventional refrigeration cycles which utilize the vapor compression cycle as described in classical thermodynamics. A PTC implements the theory of oscillatory compression and expansion of the gas within a closed volume to achieve desire refrigeration. Regenerators and pulse tubes are often viewed as the two most

complex and essential components of cryocoolers. Their design parameters such as aspect ratios (length-to-diameter ratio), physical dimensions, pore structure, and regenerator materials, have a significant impact on the coolers' overall performance. In the past the selection and/or optimization of these design parameters have been either empirical, or based on relatively crude lumped parameter or one-dimensional semi-mechanistic models. Recent CFD analyses, although still limited in scope and depth, have shown that much improvement can be achieved with respect to the design and optimization of PTCs. An example to this point is the aspect ratio (length-to-diameter ratio) of various components of a PTC. Most regenerators and pulse tubes are currently designed with large aspect ratios (L/D >>1), and as a result, one-dimensional models have been utilized to analyze the flow phenomena and predict the overall system performances. However, it is now recognized that certain future application may require small-aspect-ratio components, and recent CFD-based investigations have shown that multi-dimensional effects can be significant for abovementioned components with small aspect ratios (L/D < 2). These multi-dimensional effects, needless to say, bring the reliability of current one-dimensional models under serious question.

The need for ultra-sensitive sensors in areas such as deep space research has recently created new challenges for cryocoolers. There is now much demand for cryocoolers operating at *10 ^{o}* K *or below* temperature range for military defense and space applications, and consequently the major industrial players are building large scale cryocoolers to meet these requirements. These physically large cryocoolers require extremely large compressor input power, on the order of kilowatts, and are often accompanied by larger regenerator and pulse tube diameters, resulting in smaller aspect

ratios (L/D < 2). The design specifications of these large PTCs are unprecedented and the established empirical and semi-analytical methods may not be applicable for them. The afore-mentioned multi-dimensional flow phenomena will evidently be important. Multi-dimensional modeling is therefore needed to accurately analyze the complex fluid flow phenomena and predict the overall system performance for large diameter regenerators and pulse tubes.

An important deficiency with respect to the state of art models dealing with PTCs, which applies to well-established as well as novel and forthcoming designs, is the essentially total lack of understanding about the hydrodynamic and thermal transport parameters associated with periodic flow in micro-porous structures. This is particularly troubling with regards to the regenerator, where friction and thermal non-equilibrium between the fluid and the structure may play crucial roles. Little attention has been paid to this issue primarily because of the difficulty of experimental measurements. Multi-dimensional modeling of a regenerator is very complex and requires knowledge about the anisotropic hydrodynamic parameters in various components, in particular the regenerator.

In view of the above, this investigation is aimed at a) developing a CFD-assisted methodology for the unambiguous quantification of the directional Darcy permeability and Forchheimer's inertial hydrodynamic parameters, using experimentally-measured steady and periodic pressure drops in porous structures b) experimentally measuring and correlating the steady and periodic flows directional Darcy permeability and Forchheimer's inertial hydrodynamic parameters for several widely-used regenerator fillers, c) carrying out CFD simulations addressing PTC systems in their entirety, and

thereby performing a system-level parametric studies, d) conducting a preliminary, simulation-based assessment of the effect of miniaturization on the performance of PTCs.

1.2 Descriptions of Pulse Tube Cryocoolers or Refrigerators

Pulse Tube Coolers have been classified into two distinct categories based on the type of heat exchange process: recuperative and regenerative. In a regenerative type the heat exchange process is performed by fluid–solid interactions in a non steady flow environment [1].

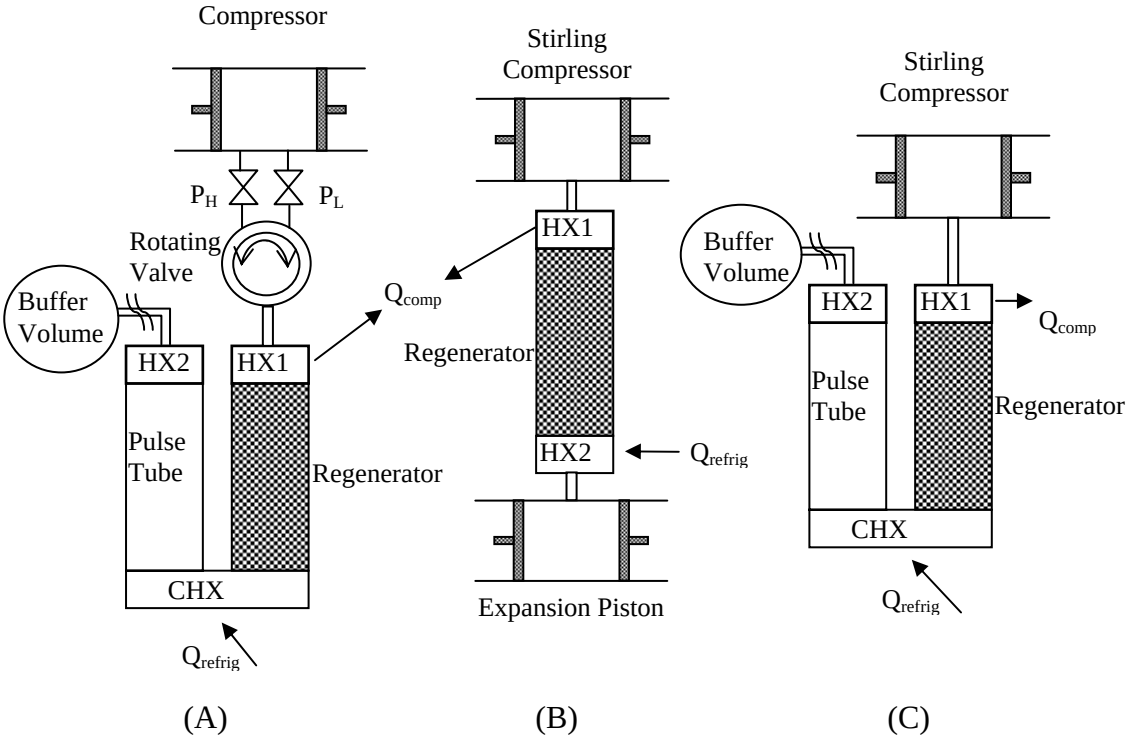

Figure 1: Schematic of Gifford-MacMahon (A), Stirling (B), and Pulse Tube (C) regenerative cryocoolers.

Three most common types of regenerative cryocooler are shown in Figure 1. They are, Gifford-McMahon, Stirling, and Pulse Tube Cryocoolers, and they are all modified versions of a well-known Stirling Thermodynamic Cycle (STC). The working fluid in regenerative cryocooler undergoes a series of compressions and expansions to complete its thermodynamic cycle. In these systems the flow is periodic.

Two common examples of recuperative cryocoolers are Joule-Thompson Cryocooler (JTC) and Brayton Cryocooler, or BC (also known as reverse Brayton Cycle). In JTC, cooling is produced by expanding a working gas from very high pressure (~20

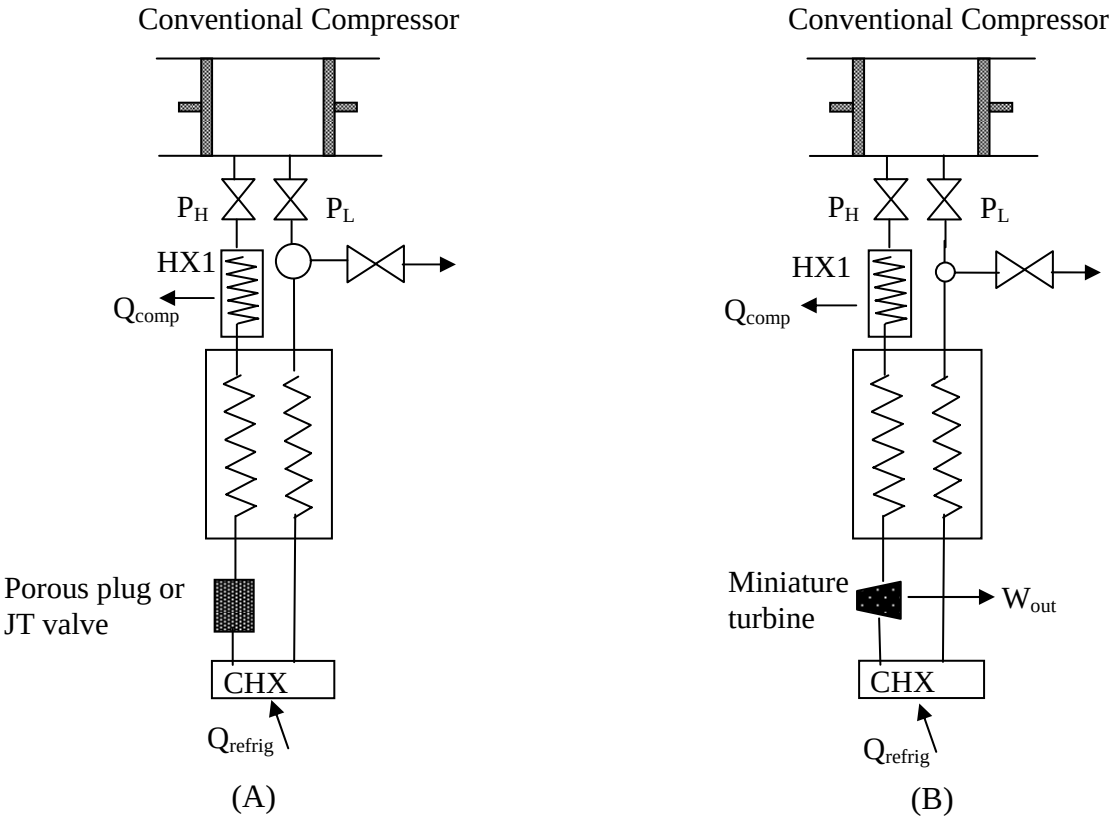

Figure 2: The schematics of Joule-Thompson (A) and Reverse-Brayton (B) recuperative cycle cryocooler.

MPa is typical) through a flow impedance such as porous plug or Joule Thompson valves [2]. The operating principles of BC are very similar to JTC; however, in BC the gas expansion is done through a miniature turbine. During the expansion process the fluid does work on the turbine and work is recovered and cooling is produced [2]. The schematics of JTC and BC are shown in Figure 2.

1.3 Application of Pulse Tube Cryocoolers

One of the earliest applications, and one that appeared about 50 years ago, was for cooling infrared sensors to about 80 ^{o}K for night vision capability of the military [2]. In this respect, over 125,000 Stirling cryocoolers for this tactical military application have been produced [2, 3]. In the space satellite applications, PTCs are mainly used for cooling of infrared focal plane arrays and its associated optics. The cooling of superconducting circuits in space application is also suitable for PTC systems. For the former applications space certified PTC can cost anywhere from $1M to $2M. The impetus behind these high prices is mainly the requirement of long life reliability, (typically 7 to 10 years without failure) in earth's orbit.

Apart from space and military applications, PTCs are also suitable for application in high-temperature superconductors, superconducting magnets of Magnetic Resonance Imaging (MRI) systems, superconductor in wireless communication bases, storage of medical specimens, cryosurgery, gas liquefaction, and Liquid Nitrogen Gas (LNG) transportations, only to name a few. PTCs have not been used in mass-produced

consumer products yet, primarily due to their low coefficients of performance. Future break-through may soon bring about significant improvements in PTC performance parameters, and lead to their application in common consumer products.

CHAPTER 2

BACKGROUND

In this chapter a brief history of pulse tube cryocoolers and some important attributes of regenerator are discussed. A method and theory for determining steady incompressible fluid hydrodynamic and heat transfer parameters using pore level direct simulation is then described in some detail. A discussion of the relevant oscillatory experimental measurements performed by other investigators will then follow.

2.1 History of Pulse Tube Cryocoolers

Gifford and Longsworth from Syracuse University in 1963 pioneered the application of pulse tube cryocoolers [4]. Their first design was based on a hollow cylindrical tube with one end open and the other end closed. The closed end was exposed to an ambient temperature heat exchanger, while the open end represented the cold end. As a result of the oscillatory flow field caused by a compressor piston, the open end was subjected to an oscillating pressure from the regenerator, causing the open end to cool [5]. A heat exchanger was later on added to the open end of the pulse tube, making the cryocooler a closed system. This refrigerator is commonly known as the Basic Pulse Tube Cryocooler, or BPTC, and is shown in Figure 3 (A).

In 1984, a Russian researcher by the name Mikulin added an orifice valve and a buffer volume to the closed end of the BPTC, as shown in Figure 3 (B) [6]. The purpose behind these additional components was to create a more appropriate phase relationship

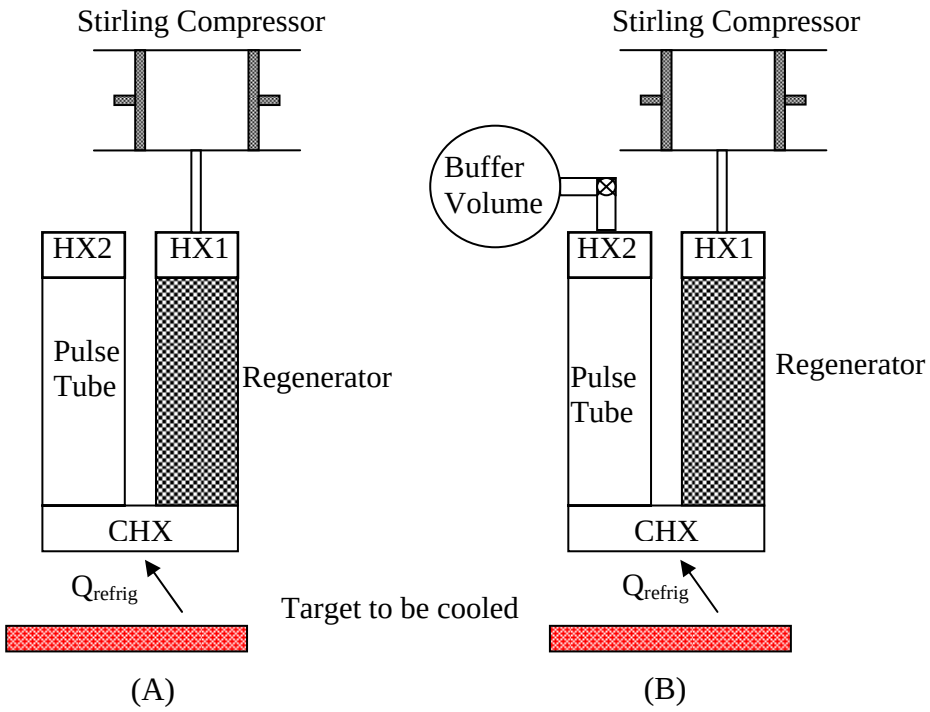

Figure 3: The Schematic of Basic Pulse Tube (A) and Orifice Pulse Tube Cooler (B).

between the oscillatory pressure and the mass flow rate. By this favorable in-phase relationship, the Orifice Pulse Tube Cryocooler (OPTC) achieved higher performance efficiency than the BPTC. This type of refrigerator could lead to temperatures as low as *60-120* ^{o} K [7], and later became the modern PTC, commonly known as orifice PTC, or OPTC, as shown in Figure 3 (B). Multiple-stage cooler and the GM (Gifford-McMahon) style cooler (operates at very low frequencies 1 Hz - 5 Hz), shown in Figure 4 and 1, respectively, have reached temperatures below *10* ^{o} K [8].

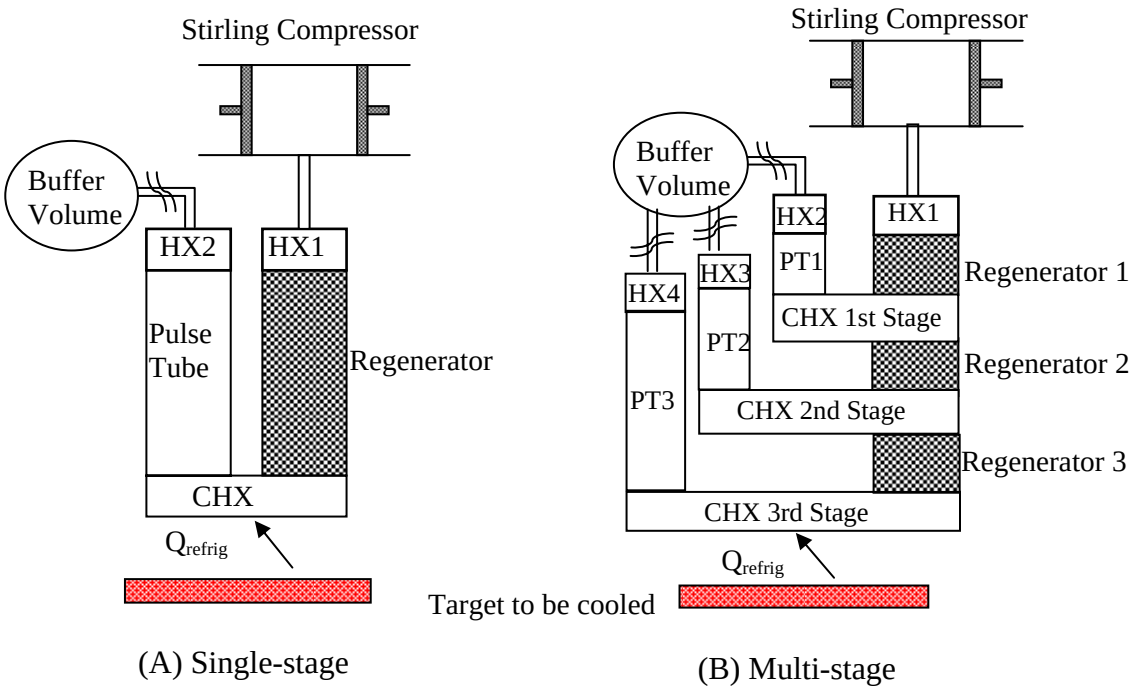

Figure 4. Schematic of single-stage and multi-stage Inertance Tube Pulse Tube Cryocooler (ITPTC).

In the mid 1990's, the orifice valve of the OPTC was replaced by a long tube called the inertance tube, shown in figure 4 (A), in some designs. In its most basic form, an inertance tube is simply a long and narrow tube that imposes a hydraulic resistance and causes an adjustable delay between the pressure responses of the pulse tube and the reservoir. In fact, by employing an electrical analogy, Roach and Kashani have shown why the inductance added by the inertance tube allows for an improved enthalpy transfer in the pulse tube [9].

There are many advantages associated with Pulse Tube Coolers. The main advantage is cooler reliability due to no moving parts at their cold end. Their cycle efficiency has improved and is nearly equal to the Stirling cycle efficiencies. Furthermore, absence of moving displacer at cold end minimizes potential vibrations [2].

2.2 Regenerators

2.2.1 Theory and Method of Determining Hydrodynamic and Heat Transfer Closure Relations

The regenerator is arguably the most important component in a PTC system. A regenerator is a micro porous structure that is subject to periodic flow of a fluid with which the regenerator should interact thermally. Flow and heat transfer in porous media constitute a mature branch of science, and a vast literature related to porous media exists. However, most of the existing literature is of little relevance to PTC regenerators due to the periodic working conditions of the latter. Mathematical and theoretical models dealing with periodic flow and heat transfer in porous media are few, and the state of knowledge about periodic flow heat transfer in porous media is relatively poor. In this respect, closure relations that accurately describe the momentum and energy transport in periodic flows are needed. Unfortunately, these periodic closure relations are not easy to obtain and pore-level numerical experiments or experimental measurements are needed.

Rigorous analysis of flow in porous media is in principle possible by pore level simulations. Such simulations are impractical for design purposes, however, and microscopic governing equations and boundary conditions can be transformed into macroscopic governing equations and boundary conditions by applying the volume averaging method [10-14]. Volumes averaging, and other similar methods, lead to macroscopic and tractable governing equations which are consistent with micro-scale conservation principles, although they mask much of the details related to pore-level processes. They also introduce constitutive relations that are needed for the closure of macroscopic conservation equations. Without pore-level direct simulation, these

macroscopic relations need to be specified empirically. Included among these are the Darcy permeability $\overline{\overline{K}}$, and Forchheimer's inertial coefficients $\overline{\overline{c_f}}$ tensors, which are needed for the closure of macroscopic momentum conservation equation.

Fluid-solid thermal interactions in porous media are even a bigger challenge than momentum interactions. Numerical experiments and theory both indicate the importance of thermal dispersion, a phenomenon resulting from the non-uniformity of the microscopic flow geometry that leads to an apparent increase in the fluid thermal conductivity [13, 15-17, 18]. For steady-state, the theory of volume averaging provides a framework for the calculation of dispersion coefficients using direct pore-level numerical simulation. A limited number of direct simulations have indeed been reported by Kuwahara et al. [19] and Nakayama et al. [21]. Kuwahara et al. have implemented 2-D pore level direct numerical simulation of macroscopic uniform flow through lattice square rods in an infinite space while imposing a linear macroscopic temperature gradient perpendicular to the flow direction to obtain the dispersion coefficient purely on a theoretical basis [19]. The schematic of Kuwahara's generic porous medium is shown in figure 5 (A) [19].

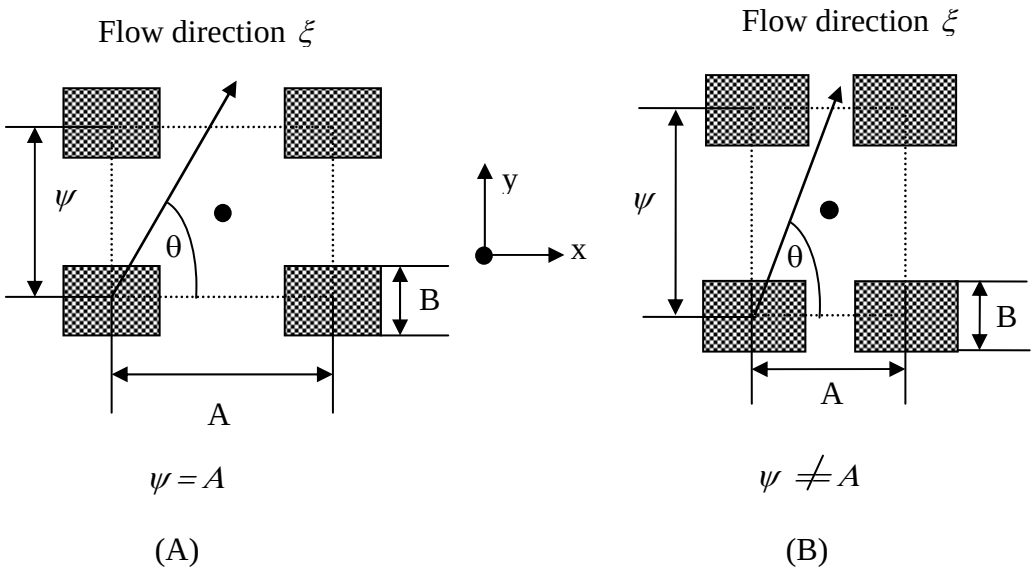

Figure 5. Control volume of isotropic (A) and anisotropic (B) square rods.

The microscopic mass, momentum, fluid-energy, and solid-energy conservation equations and boundary conditions used by Kuwahara et al. are, respectively [19]:

$$\nabla \cdot \vec{u} = 0 \tag{2-1}$$

$$\vec{u} \cdot (\nabla \cdot \vec{u}) = -\frac{1}{\rho}\nabla P + \frac{\mu}{\rho}\nabla^2 T \tag{2-2}$$

$$(\rho c)_f \nabla \cdot (\vec{u}T) = k_f \nabla^2 T \tag{2-3}$$

$$k_s \nabla^2 T = 0 \tag{2-4}$$

For boundary conditions, *on the walls:*

$$\vec{u} = 0 \tag{2-5}$$

$$T_s = T_f \tag{2-6}$$

$$k_s \left.\frac{\partial T}{\partial n}\right|_s = k_f \left.\frac{\partial T}{\partial n}\right|_f \tag{2-7}$$

On the periodic boundaries:

$$\vec{u}\big|_{x=-\psi/2} = \vec{u}\big|_{x=\psi/2} \tag{2-8}$$

$$\vec{u}\big|_{y=-A/2} = \vec{u}\big|_{y=A/2} \tag{2-9}$$

By numerical solution of the microscopic fluid and solid energy Eqs. (2-3) and (2-4), every single term in the forthcoming volume-averaged energy equation is rigorously obtained. The volume-averaged energy equation, in its general form, is:

$$[\alpha(\rho c)_f + \underline{(1-\alpha)(\rho c)_s}]\frac{\partial \langle T \rangle^f}{\partial t} + (\rho c)_f \langle \vec{u} \rangle \cdot \nabla \langle T \rangle^f = \nabla \cdot \left((\alpha k_f + \underline{(1-\alpha)k_s}) \nabla \langle T \rangle^f + \frac{1}{V} \int_{A_{\text{int}}} (k_f - k_s) T \, d\vec{A} - (\rho c)_f \langle T' \vec{u}' \rangle \right) \tag{2-10}$$

Note that the underlined terms in general should not be included unless thermal equilibrium between solid and fluid is assumed. For the case of steady state, Eqn. (2-10) can be recasts as [19]

$$(\rho c)_f \langle \vec{u} \rangle \cdot \nabla \langle T \rangle^f = \nabla \cdot \left((k_{eff} \overline{\overline{I}} + \overline{\overline{k}}_{tor} + \overline{\overline{k}}_{disp}) \cdot \nabla \langle T \rangle^f \right) \tag{2-11}$$

where

$$k_{eff} \equiv \alpha k_f + (1-\alpha) k_s \tag{2-12}$$

$$\overline{\overline{k}}_{tort} \cdot \nabla \langle T \rangle^f \equiv \frac{1}{V} \int_{A_{\text{int}}} (k_f - k_s) T d\vec{A} \tag{2-13}$$

$$\overline{\overline{k}}_{disp} \cdot \nabla \langle T \rangle^f \equiv -(\rho c)_f \langle T' \vec{u}' \rangle \tag{2-14}$$

$$\langle \xi \rangle^f = \frac{1}{V_f} \int_{V_f} \xi \, dV_f \qquad\qquad \langle \xi \rangle = \frac{1}{V} \int_V \xi \, dV \tag{2-15}$$

Note that $\langle \vec{u} \rangle^f = \alpha \langle \vec{u} \rangle$. Also note that the above equations, in general (i.e., when the underlined terms in Eqn. (2-10) are not included) do not address the solid side. A separate energy equation, or an assumed constant solid temperature, can be used. Kuwahara et al. [19] were interested in the tortuosity and dispersion terms, and for simplicity assumed thermal equilibrium between the solid and fluid. By solving conservation Eqs. (2-1) through (2-4) by the numerical algorithm proposed by Patankar and Spalding [20], and substituting the numerical results into Eqs. (2-13) and (2-14) Kuwahara et al. [19] were able to obtain tortuosity, $\overline{\overline{k}}_{tort}$, and thermal dispersion $\overline{\overline{k}}_{disp}$ over some flow parameter range. However, their volume averaged energy equations were strictly derived based on the assumptions of steady state and incompressible flow, and local thermal-equilibrium between the fluid and the solid structure.

More recently, Nakayama et al. [21] conducted a numerical experiment of porous media at a pore level using full Navier-Stokes and energy equations to obtain the interfacial heat transfer coefficient, permeability tensor, and Forchheimer tensor. Nakayama's investigation involved analyzing the generic porous medium of Kuwahara et al. [19] assuming an infinite space domain, based on varying the transverse center-to-center distance and fixing the longitudinal center-to-center distance of the unit cells (see Figure 5 (B)). As a result, an anisotropic porous media structure was replicated. The

microscopic governing equations solved by Nakayama are in fact identical to equations proposed by Kuwahara [19]; however, Nakayama implemented constant temperature thermal boundary conditions at the solid walls and also proposed obtaining the anisotropic permeability and Forchheimer tensors. In determination of permeability tensor, Nakayama incorporated Forchheimer [22] extended Darcy's law

$$-\frac{\partial \langle P \rangle^f}{\partial x_i} = (\mu_f K_{ij}^{-1} + \rho_f c_{f,ij} \left| \langle \vec{u} \rangle \right|) \langle u_j \rangle \tag{2-16}$$

where i and j represent the Cartesian second-order tensor indices, and Einstein's summation rule has been applied. In the limit of vanishing flow rate, Eqn. (2-16) simply reduces to Darcy's law as [21]

$$-\frac{\partial \langle P \rangle^f}{\partial x_i} = (\mu_f K_{ij}^{-1} + \rho_f c_{f,ij} \left| \langle \vec{u} \rangle \right|) \langle u_j \rangle \cong (\mu_f K_{ij}^{-1}) \langle u_j \rangle \tag{2-17}$$

The Darcy permeability tensor K_{ij} is determined from Eqn. (2-17), when the macroscopic intrinsic pressure gradient term on the left side of Eqn. (2-17) is replace by its numerical value found from the solution of the following equation (see Figure 5 (B)):

$$-\frac{\partial \langle P \rangle^f}{\partial \xi} = \frac{\cos\theta}{A(\psi - B)} \int_{-(\psi-B)/2}^{(\psi-B)/2} (P\big|_{x=-A/2} - P\big|_{x=A/2}) dy + \frac{\sin\theta}{\psi(A-B)} \int_{-(A-B)/2}^{(A-B)/2} (P\big|_{y=-\psi/2} - P\big|_{y=\psi/2}) dx \tag{2-18}$$

where $\partial\xi$ is a small element along the microscopic flow direction ξ, and θ is angle between the $\partial\xi$ and the x axis. The integral terms in Eqn. (2-18) are obtained from the solution of microscopic pore level governing Eqs. (2-1) through (2-4). For the determination of the Forchheimer tensor, a similar method is applied; however, for this case, the first term known as a Darcy term in the right side of Eqn. (2-16) is neglected in view of the domination of the second term, in the limiting case of high Reynolds number. It should thus be emphasized that the Nakayama's determination of hydrodynamic tensors were strictly based on the limiting cases of very low and very high flow rates. Furthermore, all these studies have addressed steady-state and incompressible flow.

The situation is much more complicated for oscillating and/or periodic flow and compressible flow in porous media. The available experimental data are very limited [18, 23-27]. Direct simulations are also difficult due to the ambiguity and even irrelevance of the definitions of various closure parameters which tie pore-scale phenomena to volume-averaged parameters. Experimental measurement is thus needed.

2.2.2 Review of System Level Pulse Tube Cryocooler and Regenerator Models

For the last 10 to 15 years, the regenerator has been the main subject of research in the cryocooler community due to their complicated flow phenomena of fluid-solid interactions and requirement of closure relations, and many well respected cryogenic scientists around the world devoted their time and effort to develop their computational regenerator models. A few regenerator models are briefly discussed here.

The most famous and well recognized regenerator model is Regen 3.2 [28]. This code is a one dimensional computational model and uses finite difference numerical

method and real helium gas properties to solve the momentum and energy transport equations in time. This code was developed by Radebaugh and O'Gallagher from NIST. One-dimensional computational models have also been developed at the Los Alamos National Laboratory (LANL) (DeltaE [29]). These and all other similar models ignored the possible effect of turbulence [30]. A few years later, Kashani and Roach, from NASA Ames Research Center, developed a computer program known as ARCOPTR [30, 31]. This program utilizes the 1-D fluid mass, momentum, and energy conservation equations to simulate the thermo-fluidic processes in the regenerator and the entire cooler. However, this program was only limited to small mass flows and small pressure and temperature oscillations. In a recent 1-D numerical simulation, Ju et al. [32] modeled the entire orifice and double-inlet PTCs, by using a common set of fluid conservation equations everywhere. The friction factor and heat transfer coefficients were chosen to be the larger among relevant laminar and turbulent correlations everywhere, however. A common feature of the regenerator models is that they assume that the working fluid and the solid porous matrix in the regenerator are everywhere at thermal equilibrium.

Harvey has recently developed a 1-D regenerator model based on the volume averaged method. He solved the model differential equations using the method of lines [1]. The one-dimensional volume-averaged mass, momentum, fluid-energy, and solid energy equations solved by Harvey [1] are, respectively:

$$\frac{\partial \rho}{\partial t} + \frac{\partial [\rho u]}{\partial x} = 0 \tag{2-19}$$

$$\frac{\partial [\rho u]}{\partial t} + \frac{\partial}{\partial x}\left[\rho u^2\right] + \frac{\partial P}{\partial x} + \left[\frac{\alpha \mu}{K} u + \frac{c_f \alpha^2 \rho}{\sqrt{K}} u^2\right] = 0 \tag{2-20}$$

$$\frac{\partial e}{\partial t} + \frac{\partial}{\partial x}\left[\rho_f u h_f - N_k k_f \frac{\partial T_f}{\partial x} \right] - a_\lambda H \left(T_s - T_f \right) = 0 \qquad (2\text{-}21)$$

$$(\rho c)_s \frac{\partial T_s}{\partial t} = \frac{\partial}{\partial x}\left[k_s \eta_s \frac{\partial T_s}{\partial x} \right] - \frac{\alpha}{1-\alpha} a_\lambda H \left(T_s - T_f \right) \qquad (2\text{-}22)$$

The model by Harvey uses the best available closure relations as of 2002 for the 1-D conservation equations. A major distinction between the model by Harvey and other models published in the open literature is that Harvey's model is capable of accounting for thermal non-equilibrium between the working fluid and the solid structure in the regenerator. The selected hydrodynamic correlations, however, are primarily based on steady state literature dealing with purely axial flow in the porous media of interest.

Gedeon has also developed a 1-D model that simulates not only the regenerator but the entire pulse tube cryocooler system [33]. Gedeon's work was implemented into a widely-used commercial software known as SAGE. An important attribute of Sage that distinguishes it from other published models is its embedded optimization routine, whereby the code can actually optimize any user-selected geometrical parameter to achieve the system's optimum performance [33]. However, Harvey et al have shown that Sage predictions can be relatively inaccurate when the code is used with its default parameters, and requires adjusting the coefficient values of the losses in the pulse tube in order to match the experimental results [34]. The results of Harvey et al. show that Sage may generally over predict the coefficient of performance of pulse tube coolers.

2.2.3 Experimental Measurements of Regenerator Parameters under Oscillatory Flows

The experimental measurements of regenerator flow impedance and heat transfer coefficient have been conducted by many and they are well documented in the open literature. However, their experimental measurements were primarily for steady flow experiments and not for oscillatory flow. Only a few oscillating flow experiment studies are cited in the open literature.

Hsu et al. [35] recently [2004] measured the velocity and the pressure drop for both steady and oscillating flows (limited to low frequency) across porous columns packed from wire screens. Their experimental measurement results showed that oscillating flow friction factors identically replicated the steady flow measurement [35, 36]. This implies that for low frequency oscillating flow the friction factor in porous media were indeed quasi-steady [35, 36].

Nam and Jeong [24, 25] conducted experimental measurements on the regenerator flow impedance and ineffectiveness under cooler operating conditions. Their instruments included fast response Hot Wire Anemometers (HWA) and high frequency pressure sensors, and these were used to measure the local instantaneous time dependent velocities, pressures, and temperatures at the inlet and exit of their experimental regenerator. As a result, they were able to completely characterize the thermodynamic properties of the fluid at both ends of the regenerator. Using the maximum pressure amplitude in their data oscillatory friction factor was correlated based on Zhao and Cheng's [37, 38] proposed friction factor relations. Zhao and Cheng's friction factor relations are

$$f = \frac{0.5\Delta P_{\max} d_h}{\rho u_{\max}^2 L} \tag{2-23}$$

where L is the length of the regenerator, d_h is the hydraulic diameter, $\Delta P_{\max}$ is the maximum pressure drop and $u_{\max}$ is the maximum velocity inside the regenerator. Further, enthalpy measurements were used to quantify the ineffectiveness of the regenerator. Nam and Jeong had used 200 mesh stainless steel screens in their regenerator.

Roberts and Desai [26] [1999] conducted an experimental study similar to the work of Nam and Jeong. However their regenerator was composed of weave 400 mesh stainless steel screens.

Ju et al [1998] measured the velocities and pressures of the compressor in a compressor-regenerator-pulse tube system operating at 50 Hz [32]. In their investigation various Reynolds number regimes were achieved by varying compressor swept volume. Based on their experimental data, they proposed the following correlation for the friction factor:

$$f = \max\left[f_1, f_2 \right] : \left\{ \begin{array}{l} f_1 = 1.6 + 180/\mathrm{Re} \\ f_2 = 0.257\,\mathrm{Re}^{-0.157} \end{array} \right\} \tag{2-24}$$

And for their analysis they used the larger friction factor value among the two listed in Eqn. (2-24).

Some earlier work has been reported along this line of research. Rawlin [39] and Radebaugh et al [40], performed similar experimental measurements and reported regenerator effectiveness and friction factors. Gedeon, in 1984, has also reported various

regenerator friction factors under oscillating flow conditions [23]. The latter work was later incorporated into his Sage Software [33].

2.3 Miniaturization of Pulse Tube Cryocooler

The miniaturization of PTCs can provide many benefits, most obviously the possibility of their application in systems where low weight and volume are essential. Miniaturization of PTCs is not straightforward, however, and a number of basic phenomena tend to deteriorate the performance of a PTC as its size is reduced. These phenomena are only quantitatively understood at this time, however. The general performance-degrading issues related to PTC miniaturization still need to be better identified and the exact physical nature and scope of these phenomena need to be adequately understood. It is fairly obvious, however, that the design and analysis methods and tools for large PTCs are unlikely to be directly applicable to miniature PTCs in which the diameter of the regenerator is smaller than about 0.6 cm. The regenerator diameter is used here as a useful reference size scale because it approximately represents the lateral dimension of linearly configured PTCs. These issues include increased surface friction and heat gain/loss, adverse thermal effects due to large thermal gradients over small distances, increased thermal boundary effects, dead volume increases (relative to the total system volume), and thermal instability in the regenerator matrix. These attributes of miniature PTCs require careful consideration and analysis, though the analysis is not simple due to the strong coupling among the multitude of miniaturization-induced phenomena.

As a preliminary investigation on the effect of system miniaturization an entire Inertance Tube Pulse Tube Cryocooler (ITPTC) were modeled and simulated. Three miniature scale ITPTC systems with total fluid volume of ~40 cc, ~10 cc, and ~0.7 cc, were modeled and simulated. The modeling, analysis, and results are described and presented in Appendix C.

CHAPTER 3

EXPERIMENT TEST APPARATUS DESIGN, SETUP, AND TEST PROCEDURES

The detail experiment test apparatus that was used to measure the directional hydrodynamic flow resistance parameters under steady and oscillatory flows are presented in this chapter. Solid models with theoretical blueprints of various components of the experimental test apparatus are presented. Test procedures for all the performed measurements are also briefly discussed. Furthermore, the pore characteristics of tested regenerator samples are also described.

3.1 Radial Pressure Drop Test Apparatus for Steady Flow

The test apparatus utilized for the measurement of radial hydrodynamic characteristics of regenerator matrices (referred to hereafter as the radial test apparatus) is schematically displayed in Figure 6, and includes a helium tank, a mass flow meter, two pressure transducers, and a specially designed annular test section that is filled with the regenerator fillers. The Helium tank contains research grade *He* with a nominal purity of 99.9999%. By manually adjusting the valves V1 and V2, the flow rate and the pressure at

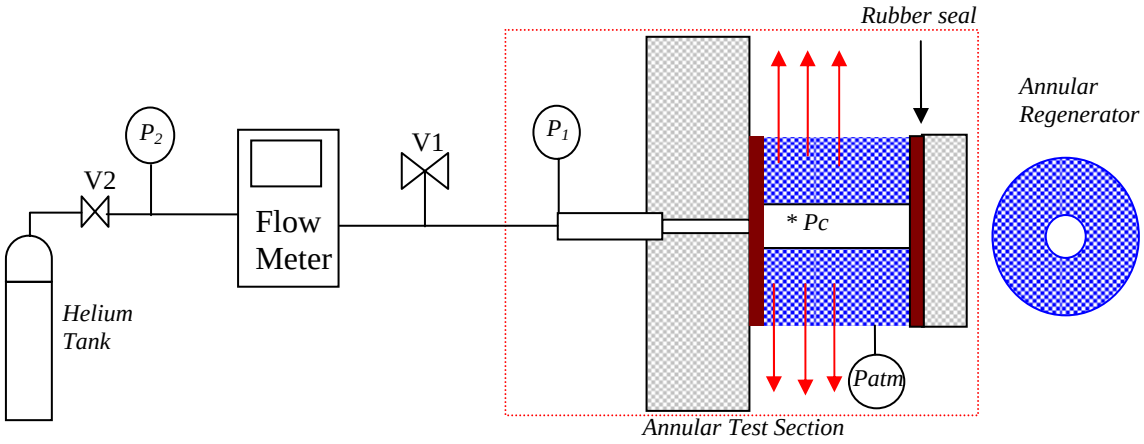

Figure 6. Schematic of radial pressure drop test apparatus for steady flow.

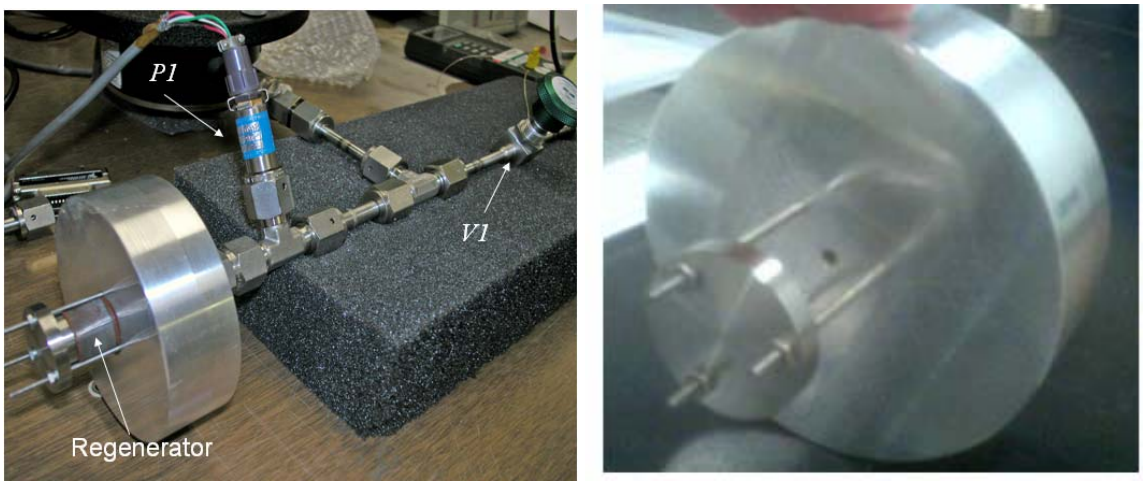

Figure 7: Radial pressure drop test apparatus for steady flow

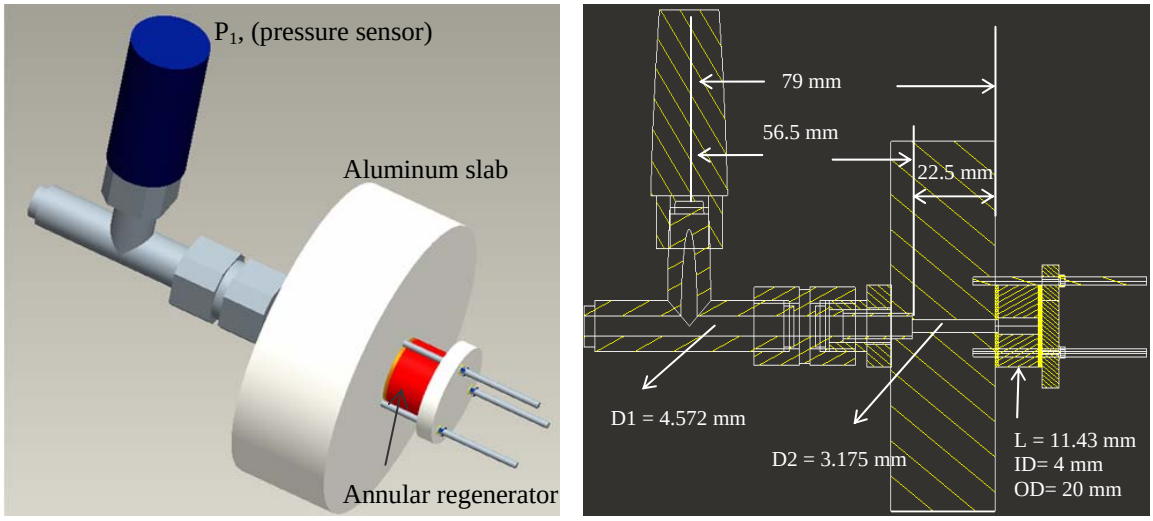

Figure 8. Exploded view of radial pressure drop test apparatus.

inlet to the test section, P_1, are both adjusted to their desired values. The exit from the annular test section was open to the atmosphere.

Details of the test section are depicted in Figures 7 and 8. It consists of a straight 3.175 mm inner diameter circular tube that leads to the annular test section. When 325 stainless steel mesh screens are of interest, for example, a stack of these screens is used, which form an 11.43 mm long porous structure with inner and outer diameters of 4 mm and 20 mm, respectively. The annular structure was constructed in the following manner. Three stainless steel rods were first threaded perpendicularly onto an aluminum slab 30 mm long and 90 mm in diameter. A 3.175 mm-diameter hole was drilled through the aluminum slab, which served as the inlet channel to the annular porous structure. The three rods were equally spaced such that a 20-mm diameter cylinder could be tightly housed between them. The rods formed three rigid supports for stacking 20 mm – diameter circular screens between them. Annular-shaped screen plates with inner and outer diameters of 4 mm and 20 mm, respectively, prepared by laser-cut procedure, were provided by Cleveland Wire, Inc. The screen plates were stacked, pressed, and fitted

between the depicted rubber seals. The free ends of the stack (the right side, in Figure 8) was sealed off by pressing a circular, 5 mm-thick aluminum plate against the assembly of screens via tightening the three hexagonal nuts on to the threaded rods. The constructed test section thus formed a leak free system, where gas could only leave through the outer surface of the annular porous structure. The porosity of the packed screens could be adjusted by tightening the end cover plates using the threaded rods.

The mass flow meter (model 826 Toptrak, from Sierra Instruments) had a response time of 800 ms, a range of 0 ~1.5 g/s, and an accuracy of +/- 1.5 % of full range. A repeatability of +/- 0.5% of full range was obtained in the tests. The two pressure transducers (Series 210-10, Paine Electronics) had an adjusted range of 0~ 27.57 bar, an accuracy of +/-0.25% of full range, and a maximum repeatability error of +/- 0.05 % of full range.

A series of pressure drop tests were conducted with stainless steel 325 mesh screens, using two porosities: 0.696 and 0.632. Each series was conducted by varying the steady state mass flow rate with valve V1, starting from a very low value and increasing the flow rate by increments, and measuring the pressure at P_1.

3.2 Radial Pressure Drop Test Apparatus for Oscillatory Flow

The test apparatus for oscillatory flow is more complicated than the test apparatus for steady flow. In oscillatory flow experiments, the entire working fluid is contained in a leak free, hermetically-closed chamber and the working fluid, typically gas, undergoes a periodic series of compressions and expansions through oscillating pressure waves. The

entire test apparatus is schematically shown in Figure 9, and included a function generator, a data acquisition system, an amplifier, a compressor, two PCB piezo pressure transducers, and an annular test section with a chamber enclosure that contains the regenerator. The entire test loop contains research grade Helium with a nominal purity of 99.9999%. A 4.29 cubic centimeter (cc) swept volume Hughes Tactical Condor compressor is used to impose the oscillatory flow in the entire test section.

Details of the test section are depicted in Figure 10. The annular test section shown in Figure 10 is the same annular test section that is used in radial pressure drop experiment for steady flow.

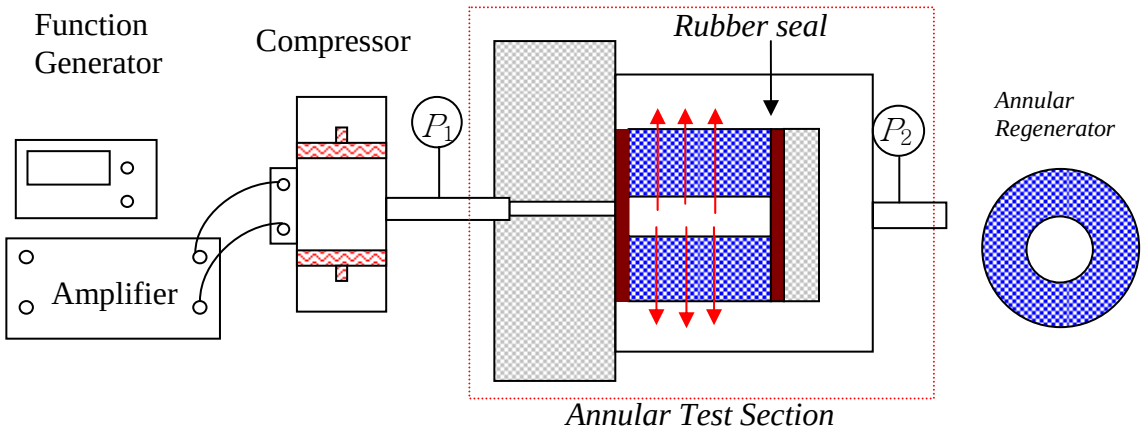

Figure 9. Schematic of radial pressure drop test apparatus for oscillatory flow

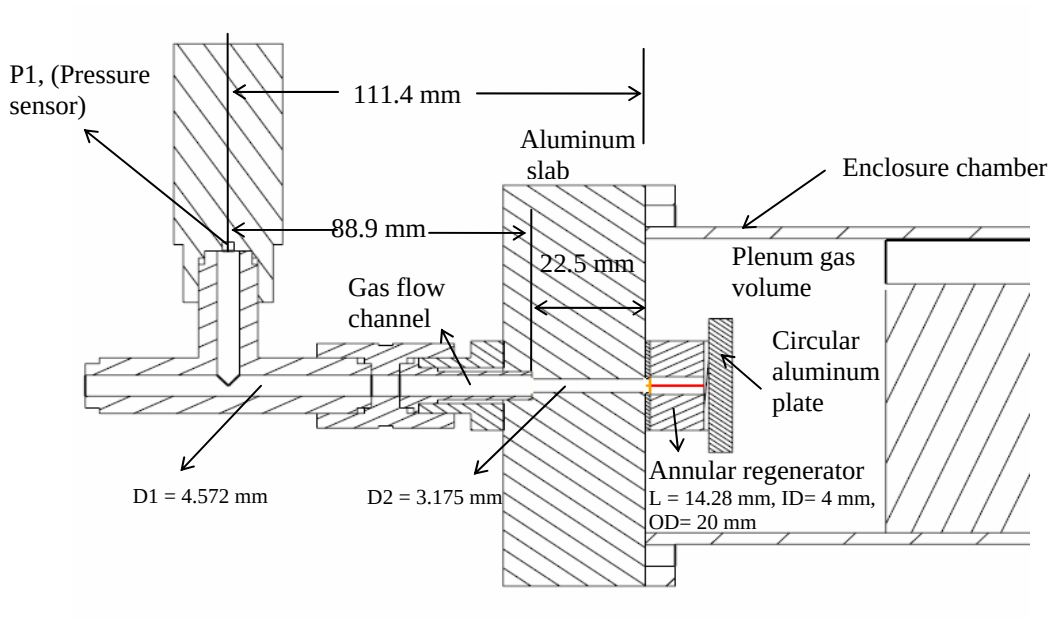

Figure 10. Detail description of radial test section and its vicinity.

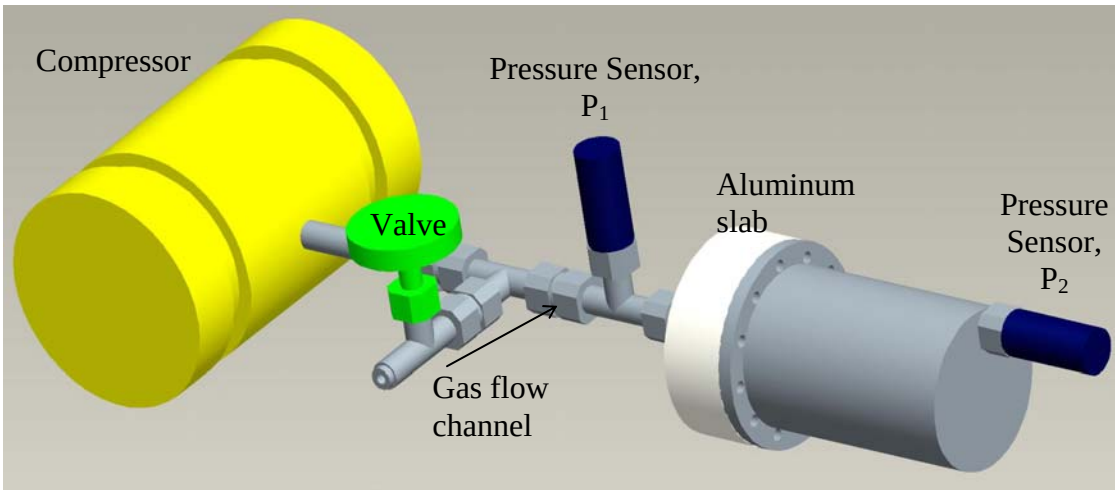

Figure 11. Radial pressure drop experimental test apparatus for oscillatory flow.

The annular test section was made of stainless steel sintered 400 mesh screens for this investigation. Annular-shaped sintered regenerator with inner and outer diameters of 4 mm and 20 mm, respectively, prepared by diffusion-bonding and Electron Discharge Machining procedure, were used (provided by Raytheon SAS Company). The sintered

400 mesh annular regenerator was fitted between the depicted rubber seals. The right-end of the regenerator (the right side, in Figure 9) was sealed off by pressing a circular, 5 mm-thick aluminum plate against the regenerator via tightening the three hexagonal nuts on to the threaded rods. The constructed test section thus formed a leak free system, where gas could only leave through the outer surface of the annular porous structure. Furthermore, a constant volume of 174 cc stainless steel chamber is used to fully enclose the entire porous medium. At the interface of stainless chamber and base aluminum, a Viton O-ring seal was used to prevent any leakage in the system.

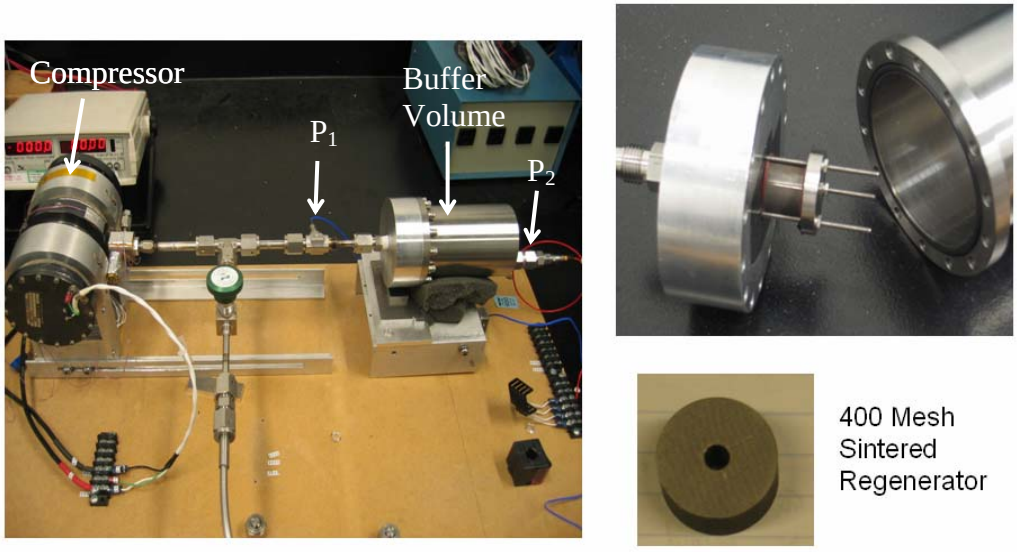

Figure 12. Experimental apparatus for radial pressure drop measurement.

The two PCB piezo transducers (model A101A05, from PCB electronics) were used to measured the local instantaneous pressures and have a response time of less than 2 μsec, a range of 0 ~689 kPa (100 psi), a resolution of 0.014 kPa (2mpsi), and a sensitivity of 7.3 mV/kPa (50mv/psi).

A total of seven oscillatory radial pressure drop tests was conducted for the sintered 400 mesh regenerator sample. Each test represented a fixed compressor frequency, and the seven tests covered the frequency range 5 to 60 Hz. In six of the tests (excluding a test at 5 Hz) the peak to peak sinusoidal voltage amplitude was first increased via the function generator, starting from a near-zero value, until either the maximum compressor piston displacement or the maximum current limit were reached. The voltage amplitude was then maintained constant and the pressures at P_1 and P_2 were recorded after steady periodic conditions were established. For the 5 Hz frequency, however, low flow conditions were sought so that the permeability in Darcy flow conditions could be tested, thereby the peak to peak sinusoidal voltage amplitude was increased only sufficiently to ensure that pressure sensor signals were viable.

3.3 Axial Pressure Drop Test Apparatus for Oscillating Flow

For oscillatory flow axial pressure drop measurement a new test apparatus was designed and built. All the designed parts were fabricated utilizing the Georgia Tech Machining Laboratory. The schematic of the entire test apparatus is shown in Figure 13. The test apparatus included a function generator, a data acquisition system, an amplifier, a compressor, three PCB piezo pressure transducers, a constant temperature hot wire anemometer, a buffer volume, and a specially designed regenerator module that houses the regenerator sample. The entire test section contains research grade Helium with a nominal purity of 99.9999%. A 4.29 cubic centimeter (cc) swept volume Hughes Tactical Condor compressor is again used to impose oscillatory flow in the entire test

section. Time histories of local instantaneous pressures at the inlet and exit of the regenerator and the buffer volume are measured. Furthermore, the regenerator inlet velocity was also measured using Hot Wire Anemometry.

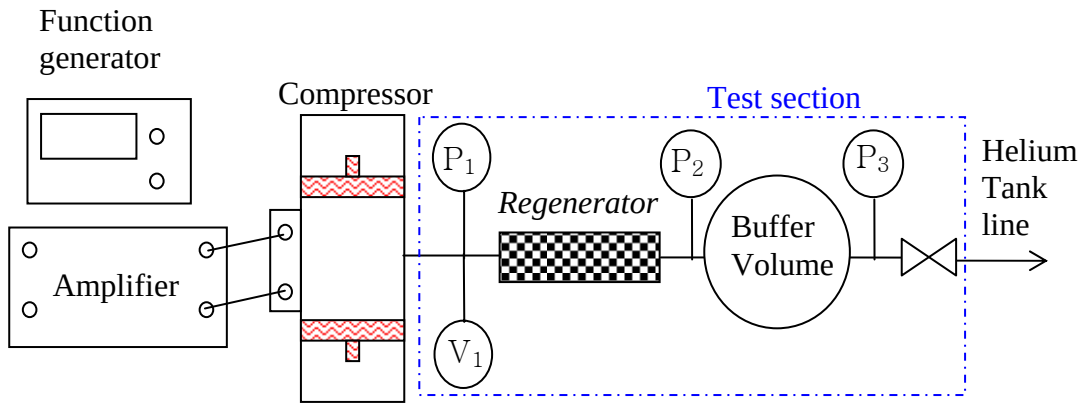

(A) Schematic of axial pressure drop test apparatus for oscillatory flow.

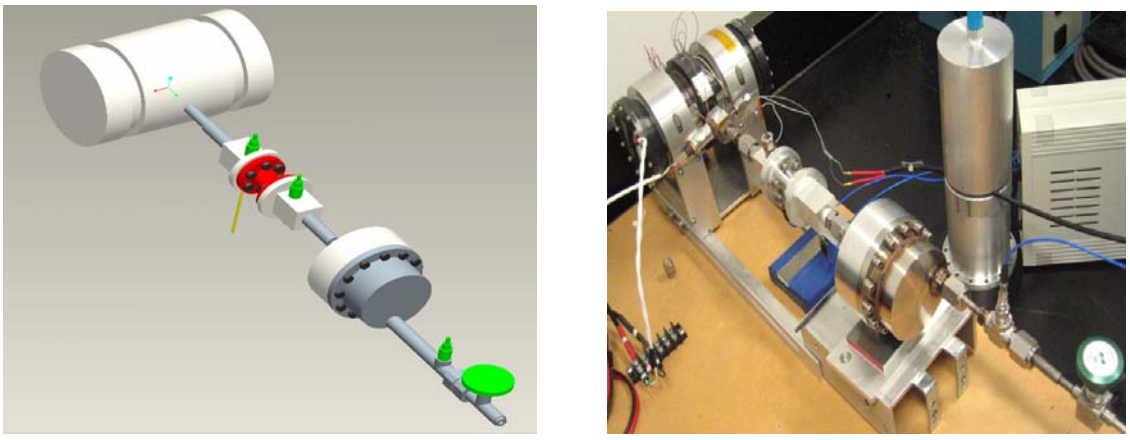

(B) Solid model and photograph of axial pressure drop test apparatus

Figure 13. A schematic (A) and photograph and solid model (B) of axial pressure drop test apparatus for oscillatory flow

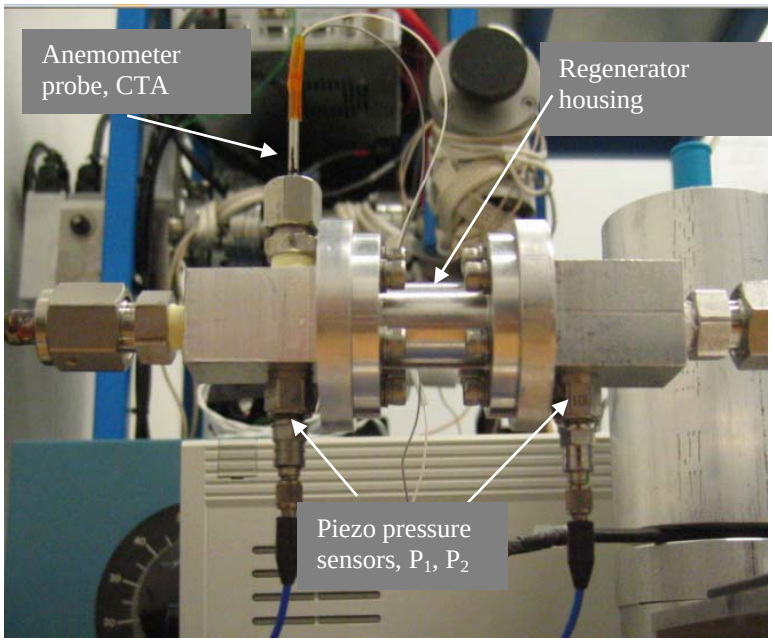

Figure 14. Detail view of instrument locations for RTS1.

Two regenerator test sections, RTS1 and RST2, were specially designed and fabricated for these tests. The details of the RTS1 test section are depicted in Figure 15. It consists of a specially designed regenerator housing module that has flange type end-connections, Viton O-ring seals, and two flange type connecting components. The RTS1 regenerator test section is design with inner diameter and length of 7.94 mm and 38.1 mm, respectively. The connecting end-components had an inner diameter and length of 7.62 mm and 40.6 mm, respectively. The RTS2 test section was designed with larger diameter and shorter length than the RTS1 test section, and its inner diameter and length were 15 mm and 31.4 mm, respectively. The end connecting components were also designed and

fabricated and had an inner diameter and length of 12.7 mm and 19.05 mm, respectively. The schematic of RTS2 is depicted in Figure 17.

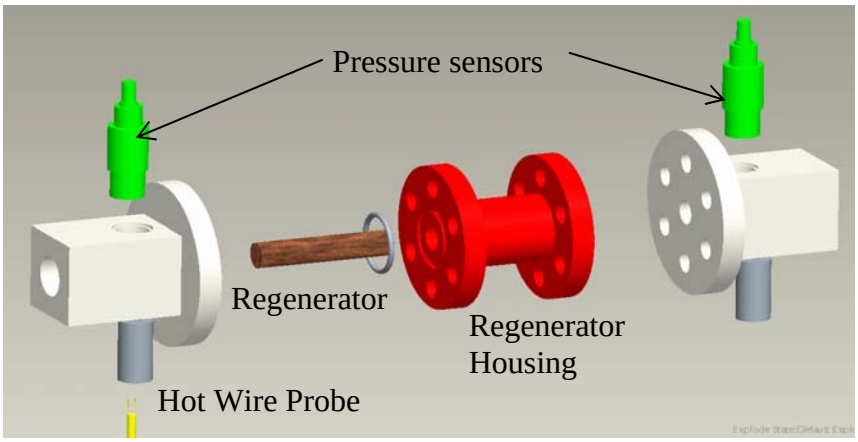

Figure 15. Exploded view of RTS1 test section.

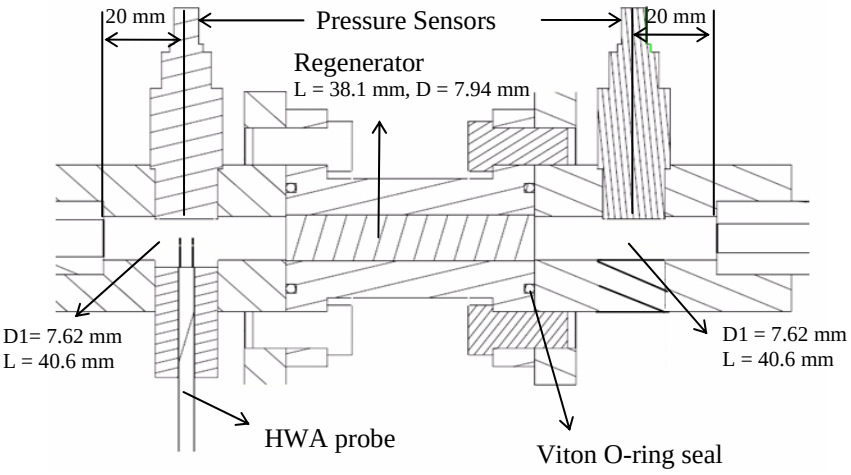

Figure 16. Detail description of RTS1 test section.

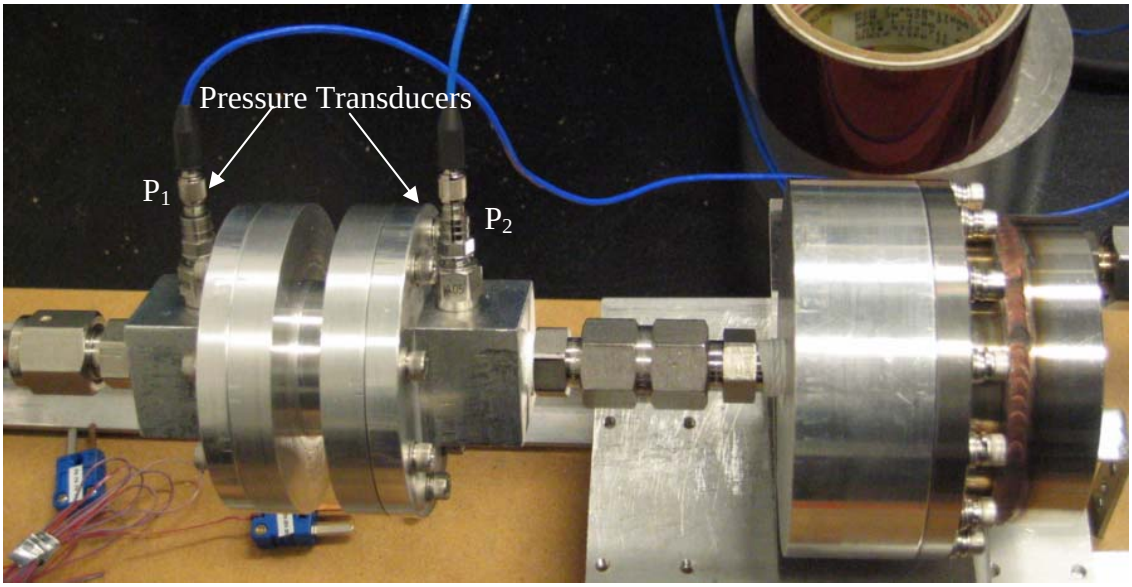

Figure 17. Schematic of RTS2 test section.

Five regenerator samples were tested. The first four regenerator fillers were fine wire mesh screens (325 and 400 mesh), sinter 400 mesh, and metallic foam metal, respectively, and they were tested using the RTS1 test section. However for the last regenerator filler, which consisted of stacked nickel micro-machined disks, the RTS2 test section was used.

Each tested regenerator was prepared using the following procedure. For the wire meshed screens (325 mesh and 400 mesh screens), the fine wire meshed screens were individually packed in the regenerator housing unit to form the regenerator. For the sintered 400 mesh regenerator, three segmented solid pieces, which were prepared by an Electron Discharge Machining (EDM) procedure, were packed into the regenerator housing module to form a 38.1 mm in length regenerator (see Figure 18). For the foam metal regenerator a single solid sintered piece was simply inserted into the module.

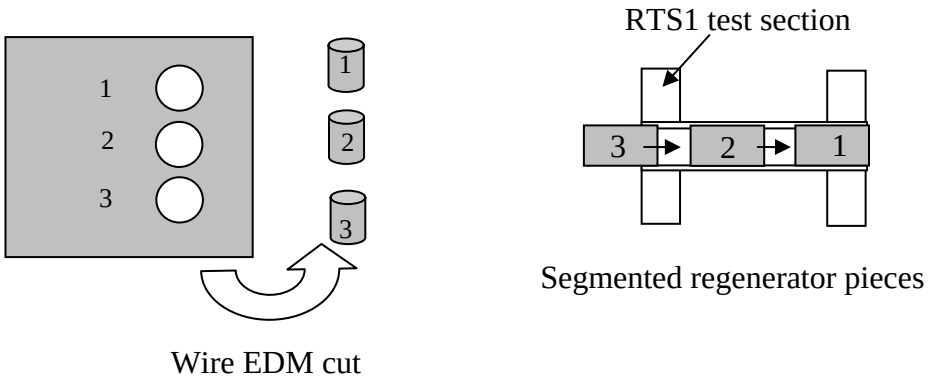

Figure 18: Sintered 400 mesh screen regenerator preparation procedure.

For the last regenerator, the nickel micro machined disks were provided by Mezzo Technologies Inc. The detail and pore characteristics of each regenerator samples are discussed later in the chapter.

A total of seven oscillatory axial pressure drop tests was conducted for each of the aforementioned regenerator samples.

3.4 Axial Pressure Drop Test Apparatus for Steady Flow

The schematic of steady axial pressure drop test is very similar to the schematic of steady radial pressure drop test apparatus described earlier in section 3.1. The apparatus included a helium tank, a mass flow meter, two high frequency pressure transducers, and a specially designed regenerator test section that contains the regenerator fillers.

A schematic of the regenerator test apparatus is shown in Figure 19. Figure 20 displays a photograph of the test apparatus. The RTS2 regenerator test section described earlier in section 3.3 is also used in the experimental setup to conduct steady flow

pressure drop measurements for micro machined disks regenerator. The dimensions of the test section and its vicinity are thus similar to Fig. 8, with the following exception.

1. A pressure transducer, P_1, is installed at a distance of 19 mm from the right-side end of the regenerator, and a pressure transducer, P_2, is installed at a distance of 140 mm from the left-side end of the regenerator (see Fig. 19).

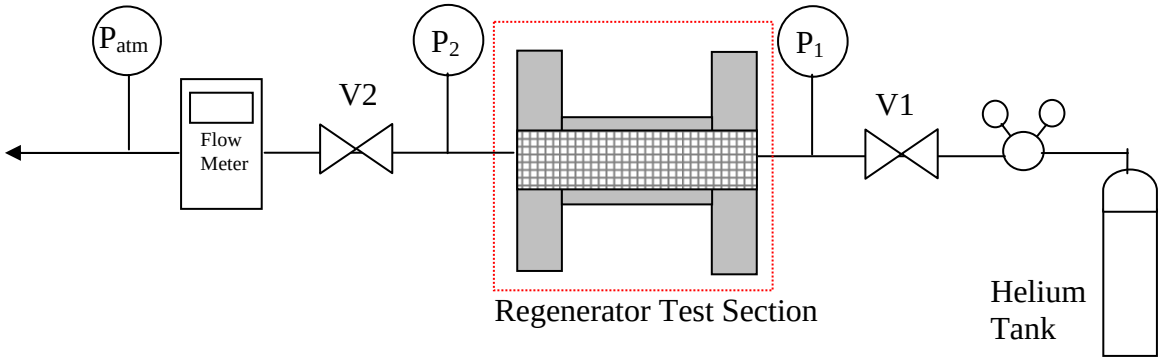

Figure 19. Schematic of axial pressure drop experimental test apparatus for steady flow.

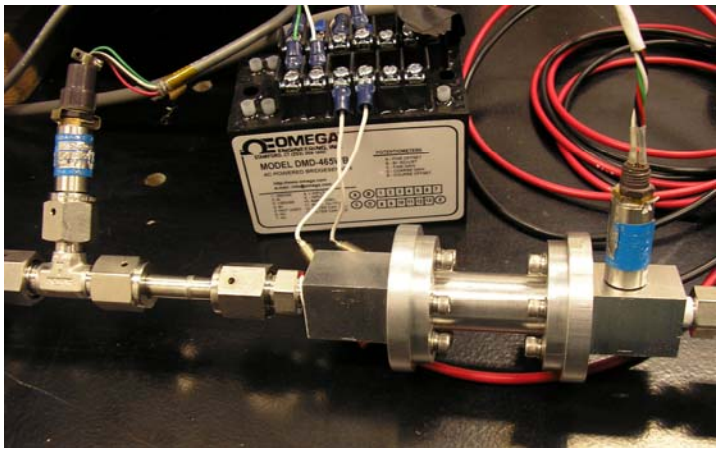

Figure 20. Axial pressure drop test section for steady flow [41].

It should be mentioned that Clearman [41] designed and built this new regenerator test section based on the original regenerator test section design for oscillatory axial

pressure drop tests, as described in section 3.3. Clearman [41] conducted a series of steady axial pressure drop measurements for same regenerator samples that were used in oscillatory tests.

3.5 Regenerator Characteristics

In this section physical pore characteristics of the tested regenerator filler samples are briefly described. Two of the five tested regenerator samples were made of fine wire mesh screens (325 mesh and 400 mesh), one sample was made of sintered 400 mesh screens, one from foam metal, and the fifth was made of micro-machined disks. The first four are among the most widely used and studied regenerator fillers in cryocooler systems, and they are all made from stainless steel. The last regenerator is a novel one and is made of nickel micro machined disks, and had the potential for extensive use in the next generation cryocoolers. The important characteristics of the tested regenerators are summarized in Tables 1 and 2.

Table 1. Summary of tested regenerators for radial flow tests.

Regenerator type	Description	Measured porosity
325 mesh screen	Stainless Steel, wire diameter: 35.6 um ID: 4 mm, OD: 20 mm, length:11.43 mm	0.696
325 mesh screen	Stainless Steel, wire diameter: 35.6 um ID: 4 mm, OD: 20 mm, length: 9.53 mm	0.632
Sintered 400 mesh	Stainless Steel, 400 mesh screens sintered/ annular Geometry ID: 4 mm, OD: 20 mm, length:14.28 mm	0.62

Table 2. Summary of tested regenerators for axial flow tests.

Regenerator type	Description	Measured porosity
325 mesh screen	Stainless Steel, Wire diameter: 35.6 um Packed to length: 38.1 mm (1.5”) Diameter: 7.94 mm (0.3125”)	0.692
400 mesh screen	Stainless Steel, Wire diameter: 25.4 um Packed to length: 38.1 mm (1.5”) Diameter: 7.94 mm (0.3125”)	0.692
Sintered 400 mesh	Stainless Steel, 400 mesh screens sintered/ segmented into 3 pieces Length: 38.1 mm (1.5”), Diameter: 7.94 mm (0.3125”)	0.62
Metallic foam metal	Stainless Steel, Sintered foam metal plug Length: 38.1 mm (1.5”), Diameter: 7.94 mm (0.3125”)	0.5547
Micro-machined disks *	Nickel, Pore size: 36um - 40 um Length: 31.4 mm (1.236”) Diameter:14.99 mm (0.59”)	0.268

*Provided by Mezzo Technologies Inc.

The porosity of each test section was measured by measuring the weight and volume of the test section, and using the following expression:

$$\alpha_{annular} = 1 - \frac{V_s}{V_{total}} = 1 - \frac{4\,m_s/\rho_s}{\pi\, l\left(d_o^2 - d_i^2\right)} \tag{3-1}$$

$$\alpha_{solid\ cylinder} = 1 - \frac{V_s}{V_{total}} = 1 - \frac{4\,m_s/\rho_s}{\pi\, l d^2} \tag{3-2}$$

The physical pore characteristics of the regenerator fillers can be better understood in Figures 21-23.

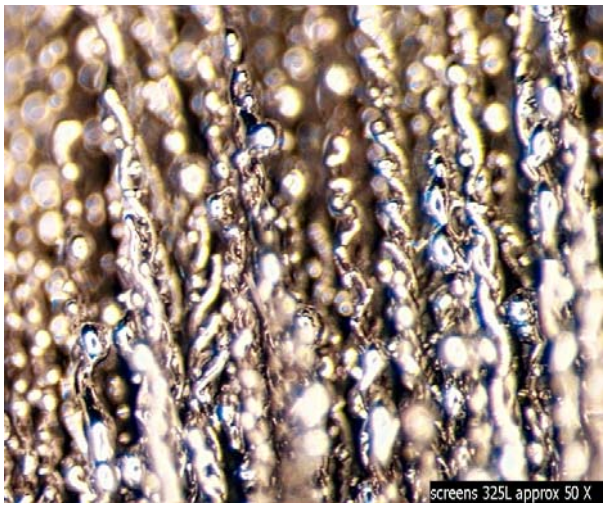

Figure 21. Radial flow path of stacked stainless steel 325 mesh screens.

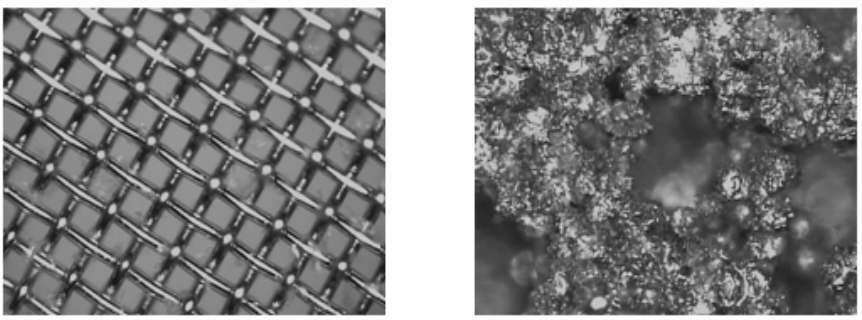

(A) (B)

Figure 22. Fine wire mesh screens (A) and metallic foam (B) for axial flow path [1].

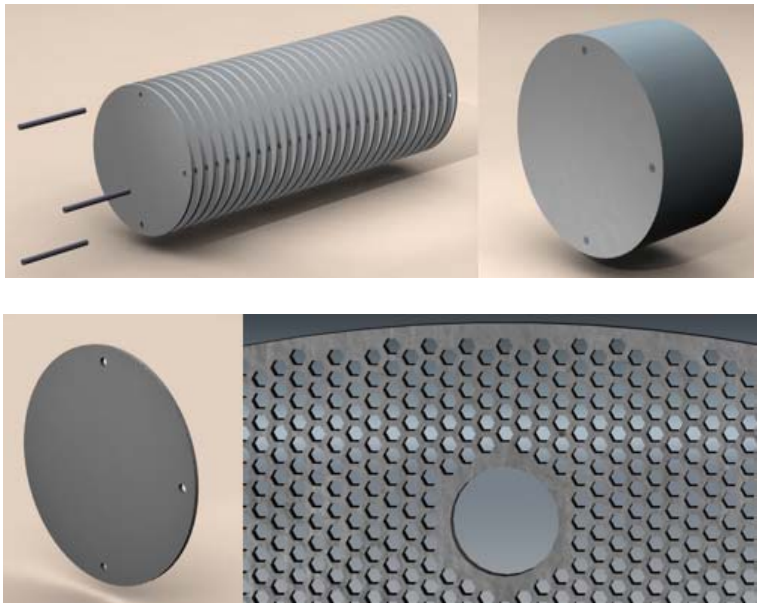

Figure 23. Building blocks of micro machined disks regenerator [Mezzo Technologies Inc].

The nickel micro machined disks were provided by International Mezzo Technologies Inc (Baton Rouge, Louisiana). The disks are manufactured such that they each have three holes drilled in them (see figure 23). When the plates are stacked so that these three holes are aligned, all the perforations in all the stacked plates also end up perfectly aligned. The alignment of the aforementioned three holes is achieved by using three rods, as depicted in Figure 23. Once properly stacked and aligned, the micro machined nickel plates actually produce a network of parallel micro-channels with circular cross-sections.

CHAPTER 4

MODELING AND SOLUTION METHODS

This chapter describes the basic modeling and solution methods that were used for simulating the experiments. The continuum-based conservation equations for basic single-phase fluid flow and heat transfer in open and porous media, which were used for modeling the entire test apparatus, are first presented. Two exact solutions for one dimensional flow pressure drop across a regenerator are then derived and presented. Finally, the method applied for CFD modeling of entire conventional-size are presented and discussed.

4.1 CFD-Based Modeling and Governing Conservation Equations

CFD simulations in this study were performed using the Fluent [42] code package. Fluent is a well-known and widely-used computer program for modeling fluid flow and heat transfer processes in complex engineering problems. Fluent offers the flexibility of meshing any complex geometry and solving complicated 2-dimensional and 3-dimensional problems. Transient flow and transport phenomena in porous media, two-phase flow, and volumetrically-generating sources can all be modeled by Fluent. Fluent numerically solves the entire continuum fluid and energy equations with no arbitrary assumptions. Although Fluent's basic conservation equations and numerical solution

methods are not accessible to users, the code allows the users to develop their own subroutines (referred to as User Defined Functions, or UDFs) and couple them with the main code in order to add or modify closure relations and impose arbitrary transient boundary conditions.

For this investigation, two types of continuum-based conservation equations were utilized for modeling the fluid flow and heat transfer processes. One set of continuum-based conservation equations are the well known Navier-Stokes (NS) equations with energy transport equation. For components and parts in the test apparatus that satisfy the continuum assumption where mean free path of gas molecules is much smaller than the characteristic dimension of the components the NS and energy equations will be used to solve the flow and energy transport phenomena. The other set represents the volume-averaged conservation equations, based on porous media theory. For the component parts that are better represented as a porous medium, these volume-averaged continuum conservation equation will be used to solve the fluid flow and heat transfer processes. All porous media/regenerator part will be modeled using the latter set of conservation equations.

The general continuum-based governing equations (NS and Energy) used by the Fluent code [42] are as follows

$$\frac{\partial \rho}{\partial t} + \nabla \cdot \left(\rho \vec{u} \right) = 0 \tag{4-1}$$

$$\frac{\partial \left(\rho \vec{u} \right)}{\partial t} + \nabla \cdot \left(\rho \vec{u} \vec{u} \right) + \nabla P - \nabla \cdot \bar{\bar{\tau}} - \rho \vec{g} = 0 \tag{4-2}$$

$$\nabla \cdot \left(k \nabla T + \overline{\overline{\tau}} \cdot \vec{u} \right) - \frac{\partial \left(\rho E \right)}{\partial t} - \nabla \cdot \left(\vec{u} \left(\rho E + P \right) \right) = 0 \qquad (4\text{-}3)$$

where

$$E = h - \frac{P}{\rho} + \frac{u^2}{2} \qquad (4\text{-}4)$$

$$\overline{\overline{\tau}} = \mu \left\{ \left\langle \nabla \vec{u} + \nabla \vec{u}^T \right\rangle - \frac{2}{3} \nabla \cdot \vec{u} \overline{\overline{I}} \right\} \qquad (4\text{-}5)$$

where μ is molecular viscosity, and $\overline{\overline{I}}$ is the second-order unit tensor. The second term on the right hand side of Eqn. (4-5) represents the effect of volume dilation. The factor of $2/3\,\mu$ is in fact the second coefficient of viscosity. All properties in these equations represent the properties of the working fluid (usually helium for cryocoolers and their experimental representations).

The above equations apply to all components of an entire ITPTC system, except for the regenerator and heat exchangers. The regenerator needs to be modeled as a porous medium for obvious reasons. The warm and cold-end heat exchangers are also modeled as a porous media in this study because porous media representation is flexible and general, and is not restricted to any particular geometric configuration. When it is assumed that there is local thermodynamic equilibrium between the fluid and the solid structure, the mass, momentum, and energy equations in the porous media components are:

$$\frac{\partial(\alpha\rho)}{\partial t} + \nabla\cdot(\alpha\rho\vec{u}) = 0 \tag{4-6}$$

$$\frac{\partial(\alpha\rho\vec{u})}{\partial t} + \nabla\cdot(\alpha\rho\vec{u}\vec{u}) + \alpha\nabla P + \nabla\cdot\left(\alpha\overline{\overline{\tau}}\cdot\vec{u}\right) - \alpha\vec{F}_{bf} + \mu\overline{\overline{\beta}}^{-1}\cdot\vec{u} + \frac{\overline{\overline{C}}\rho}{2}\cdot|\vec{u}|\vec{u} = 0 \tag{4-7}$$

$$\nabla\cdot\left(\left(\alpha k_f + (1-\alpha)k_s\right)\nabla T + \overline{\overline{\tau}}\cdot\alpha\vec{u}\right) = \frac{\partial}{\partial t}\left(\alpha\rho_f E_f + (1-\alpha)\rho_s E_s\right) + \nabla\cdot\left(\alpha\vec{u}\left(\rho_f E_f + P\right)\right) \tag{4-8}$$

where α is the porosity and $\overline{\overline{\beta}}$ *[m²]* and $\overline{\overline{C}}$ *[m⁻¹]* appearing in Eqn. (4-7) are viscous and inertial resistance coefficient tensors according to Fluent's notations. The velocity $\vec{u}$ in fact represents the volume-averaged intrinsic (physical) fluid velocity, namely $\langle\vec{u}\rangle^f$.

When flow along a principal direction x (axial) and r (radial) is considered the last two terms appearing in Eqn. (2-20) which represents Darcy permeability, K_j and Forchheimer's inertial coefficient, $C_{f,j}$, can be compared directly to the last two terms in Eqn. (4-7) and obtain the following relationship:

$$\frac{\alpha\mu}{K_j}u_j + \frac{C_{f,j}\alpha^2\rho}{\sqrt{K_j}}\cdot|\vec{u}|u_j = \frac{\mu}{\alpha\beta_j}u_j + \frac{C_j\rho}{\alpha 2}\cdot|\vec{u}|u_j \tag{4-9}$$

where $j = x \text{ and } r$. By comparing the coefficients of each terms, the Darcy permeability, K_j and the Forchheimer's inertial coefficient, $C_{f,j}$, can be represented as:

$$K_j = \alpha^2\beta_j \tag{4-10}$$

$$c_{f,j} = \frac{C_j \sqrt{K_j}}{2\alpha^3} \tag{4-11}$$

In the forthcoming sections, several computational models will be developed using the above sets of equations to characterize the fluid flow and heat transfer transport in the experiments.

4.2 Exact Solutions for Steady flow Pressure Drop in an Anisotropic Porous Medium

There are only a limited numbers of exact solutions that describe the pressure drop across a porous media. In this section, two exact solutions are derived and presented. First, the axial pressure drop across a cylindrical porous media bounded by an impermeable wall on the outer boundary of the porous media is presented for 1D compressible, isothermal, and steady flow. Second, an analytic solution for the radial pressure drop across an annular porous medium is presented for one-dimensional compressible, isothermal, steady flow case.

Assuming that the axial direction is a principal direction of the porous structure, steady-state conditions flow with negligible convective acceleration, viscous diffusion, and external body forces, Eqn. (4-7) reduces to:

$$\frac{dP}{dx} = -\frac{\mu}{\alpha\beta_x} u_x - \frac{C_x \rho}{\alpha 2} u_x^{\,2} \tag{4-12}$$

where x represents the axial coordinate. Upon substituting ideal gas equation of state under the assumption of isothermal condition the density gradient is expressed as:

$$\frac{d\rho}{dx} = -\frac{\mu}{\alpha RT\beta_x}u_x - \frac{C_x\rho}{2\alpha RT}u_x^{\,2} \tag{4-13}$$

By substituting mass conservation in Eqn. (4-13) the integral form of axial velocity becomes:

$$d\left(\frac{\dot{m}}{A_f u_x}\right) = \left[-\frac{\mu}{RT\alpha\beta_x}u_x - \frac{C_x\dot{m}}{2RT\alpha A_f}u_x\right]dx \tag{4-14}$$

$$\int \frac{1}{u_x}\, d\left(1/u_x\right) = \int\left(-\frac{\mu A_f}{\dot{m}RT\alpha\beta_x} - \frac{C_x}{2RT\alpha}\right)dx \tag{4-15}$$

By direct integration the explicit form of local axial velocity is found to be:

$$\frac{1}{2u_x^2} = G_1 - \frac{\mu A_f}{\dot{m}RT\alpha\beta_x}x - \frac{C_x\dot{m}}{2\dot{m}RT\alpha}x \tag{4-16}$$

where G_1 is an integration constant that is determined from the local fluid properties at inlet. Using the inlet fluid properties, G_1 is defined as:

$$G_1 = \frac{1}{2}\left(\frac{P_i A_f}{\dot{m} RT}\right)^2 \tag{4-17}$$

Finally, the explicit form of intrinsic axial velocity is derived as:

$$\frac{1}{2u_x^2} = \frac{1}{2}\left(\frac{P_i A_f}{\dot{m} RT}\right)^2 - \left[\frac{\mu A_f}{\dot{m} RT \alpha \beta_x} + \frac{C_x}{2RT\alpha}\right] x \tag{4-18}$$

where $\dot{m}$ is mass flow rate, A_f is flow cross sectional area (which, on the average, is $A\alpha$), R are T are universal gas constant and local static fluid temperature, respectively, and x is the axial coordinate which is oriented along the length of the porous media. If local axial friction factor and axial pressure drop are defined, respectively, by:

$$f_{axial} = \frac{\mu}{\rho u_x \sqrt{\beta_x}} + \frac{C_x \sqrt{\beta_x}}{2} \tag{4-19}$$

$$\Delta P_{axial} = P_i\left(x = 0\right) - P_e\left(x = l\right) = \left(P_i - P_e\right)_{axial} \tag{4-20}$$

Equation (4-18) can be recasts to:

$$\frac{-f_{axial}}{\sqrt{\beta_x}\alpha RT} = \frac{1}{2l}\left[\frac{1}{u_{x,e}^2} - \frac{\left(\Delta P_{axial} + P_e\right)^2}{\left(\rho_e u_e RT\right)^2}\right] \tag{4-21}$$

After some manipulations, the steady-state axial pressure drop associated with the flow of an isothermal ideal gas across any porous media is found to have the following form:

$$\left[\Delta P_{axial} + \frac{\Delta P_{axial}^2}{2p_e}\right] = \frac{RTl}{P_e {A_f}^2}\left\langle \frac{\mu A_f}{\alpha\beta_x}\dot{m} + \frac{C_x}{2\alpha}\dot{m}^2 \right\rangle \tag{4-22}$$

where l is length of the porous media and subscript e represents local fluid properties at the exit ($x = l$) of the porous media. If mass flow rate and pressure drop are known through experiments then local hydrodynamic parameters, namely the viscous resistance coefficient β_x and inertial resistance coefficient C_x can be found through Eqn. (4-22).

Equation (4-22) is thus an analytical form of pressure drop across any porous media for 1D, compressible, isothermal, steady flow with no spatial acceleration, no viscous dissipation, and no external body force.

The analytic form of radial pressure drop across an annular porous media is now derived. We assume that the porous medium is symmetric with respect to the axial direction. In that case, any radial direction will be a principal direction. Using the cylindrical coordinate system and assuming 1-D radial steady flow with negligible convective acceleration, viscous dissipation, and external body forces, Eqn. (4-7) is reduced to:

$$\frac{dp}{dr} = -\frac{\mu}{\alpha\beta_r}u_r - \frac{C_r\rho}{\alpha 2}u_r^2 \tag{4-23}$$

where u_r is volume-averaged intrinsic radial velocity and α is porosity. By using mass conservation and ideal gas equation of state under isothermal assumption Eqn. (4-23) can be recasts to:

$$\rho \frac{d\rho}{dr} = -\frac{\mu G_2}{\alpha^2 r RT \beta_r} - \frac{C_r G_2^2}{2\alpha^3 r^2 RT} \tag{4-24}$$

with G_2 being an integration constant to be specified from mass conservation. Integration is applied to both sides of Eqn. (4-24) with the condition at the inner radius, r_i, and an arbitrary r as the limits of integration, to get:

$$\int_{\rho_{inlet}}^{\rho} \rho d\rho = -\int_{r_i}^{r} \left\langle \frac{\mu G_2}{\alpha^2 RT \beta_r} \frac{1}{r} + \frac{C_r G_2^2}{2\alpha^3 RT} \frac{1}{r^2} \right\rangle dr \tag{4-25}$$

Using mass conservation, we can write:

$$G_2 = \frac{\dot{m}}{2\pi l} \tag{4-26}$$

Substituting Eqn. (4-26) into Eqn. (4-25) and performing the integrations, the density variation with respect to r is found to be:

$$\frac{\rho^2}{2} = \frac{\rho_i^2}{2} + \left\langle \frac{\mu \dot{m}}{2\pi l \alpha^2 RT \beta_r} \ln\left(\frac{r_i}{r}\right) + \frac{C_r \dot{m}^2}{8\pi^2 l^2 \alpha^3 RT} \left(\frac{1}{r} - \frac{1}{r_i}\right) \right\rangle \tag{4-27}$$

By defining the radial pressure drop as:

$$\Delta P_{radial} = P\left(r = r_i\right) - P\left(r = r_o\right) = \left(P_i - P_e\right)_{radial} \tag{4-28}$$

and using ideal gas equation of state, the radial pressure drop across annular porous media is found to be:

$$\Delta P_{radial} = P_i - \left[\left(\frac{P_i}{RT}\right)^2 + \left\langle \frac{\mu \dot{m}}{\pi l \alpha^2 RT \beta_r} \ln\left(\frac{r_i}{r_o}\right) + \frac{C_r \dot{m}^2}{4\pi^2 l^2 \alpha^3 RT}\left(\frac{1}{r_o} - \frac{1}{r_i}\right)\right\rangle\right]^{0.5} RT \tag{4-29}$$

where r_i and l are inner radius and length of the annular porous media. The subscript i represents local fluid properties at the inlet ($r = r_i$) of the annular porous media. If the mass flow rate and pressure drop are known from experimental data, local radial hydrodynamic parameters β_r and C_r can be empirically determined.

Equation (4-29) is thus an analytic solution to a radial pressure drop across an annular porous media for a 1-D radial, isothermal, compressible, steady flow with no spatial acceleration, viscous dissipation, or external body forces.

Equations (4-22) and (4-29) can also be represented using Darcy permeability, K_j and Forchheimer's inertial coefficient, $C_{f,j}$ by substituting Eqs. (4-10) and (4-11). Their pressure drop relations are:

$$\left[\Delta P_{axial} + \frac{\Delta P_{axial}^2}{2 p_e}\right] = \frac{RTl}{P_e A_f{}^2}\left\langle \frac{\alpha \mu A_f}{K_x}\dot{m} + \frac{c_{f,x}\alpha^2}{\sqrt{K_x}}\dot{m}^2 \right\rangle \quad (4\text{-}30)$$

$$\Delta P_{radial} = P_i - \left[\left(\frac{P_i}{RT}\right)^2 + \left\langle \frac{\mu \dot{m}}{\pi l RTK_r}\ln\left(\frac{r_i}{r_o}\right) + \frac{c_{f,r}\dot{m}^2}{\sqrt{K_r}\,2\pi^2 l^2 RT}\left(\frac{1}{r_o} - \frac{1}{r_i}\right)\right\rangle\right]^{0.5} RT \quad (4\text{-}31)$$

4.3 Computational Fluid Dynamics (CFD) Models

4.3.1 CFD Model for Steady Radial flow

The commercial CFD code Fluent ® [42] was used to model the entire annular test section, shown in Figure 6, in order to facilitate the interpretation of the experimental data. Given the configuration of the test section, axi-symmetric, two-dimensional flow was assumed. The simulated system evidently has two completely different parts (a pure single phase fluid and a porous media). For the open (purely fluid) parts, the steady state mass, momentum and energy equations solved by Fluent are, respectively:

$$\nabla \cdot \left(\rho \vec{u}\right) = 0 \quad (4\text{-}32)$$

$$\nabla \cdot \left(\rho \vec{u}\vec{u}\right) + \nabla P - \nabla \cdot \overline{\overline{\tau}} = 0 \quad (4\text{-}33)$$

$$\nabla \cdot \left(k \nabla T + \overline{\overline{\tau}} \cdot \vec{u} \right) - \nabla \cdot \left(\vec{u} \left(\rho E + P \right) \right) = 0 \tag{4-34}$$

where E and $\overline{\overline{\tau}}$ are defined according to Eqs. (4-4) and (4-5), respectively. All properties represent the Newtonian working fluid, helium. The above equations apply to all sections in the entire test section shown in Figure 6, except for the annular porous structure (i.e., the stacked of screens). The latter region is modeled as an anisotropic porous medium with local thermal equilibrium assumption. The steady-state mass, momentum, and energy equations for this region can then be represented as

$$\nabla \cdot \left(\alpha \rho \vec{u} \right) = 0 \tag{4-35}$$

$$\nabla \cdot \left(\alpha \rho \vec{u} \vec{u} \right) + \alpha \nabla P + \nabla \cdot \left(\alpha \overline{\overline{\tau}} \right) - \alpha \vec{F}_{bf} + \mu \overline{\overline{\beta}}^{-1} \cdot \vec{u} + \frac{\overline{\overline{C}} \rho}{2} \cdot \left| \vec{u} \right| \vec{u} = 0 \tag{4-36}$$

$$\nabla \cdot \left(\left[\alpha k_f + (1-\alpha) k_s \right] \nabla T + \overline{\overline{\tau}} \cdot \alpha \vec{u} \right) - \nabla \cdot \left(\alpha \vec{u} \left(\rho_f E_f + P \right) \right) = 0 \tag{4-37}$$

where $\overline{\overline{\beta}}$ and $\overline{\overline{C}}$ represent the viscous resistance coefficient and the inertial resistance coefficient tensors. All velocities are volume-averaged physical (intrinsic) velocities.

Steady flow CFD simulations for the entire test section depicted in Figure 6 were performed using approximately 5500 mesh nodes. The nodalization of the test section was done by the Gambit software [43]. Once the physical 2-D drawings were generated, meshing was applied to the drawing as shown in Figure 24. Upon successful meshing process, the meshed case is then imported into Fluent. At this stage, the material

properties and the boundary conditions are assigned to the system based on the actual problem definitions. For this model, the boundary conditions included known pressure P_1 or mass flow rate at inlet, and atmospheric exit pressure.

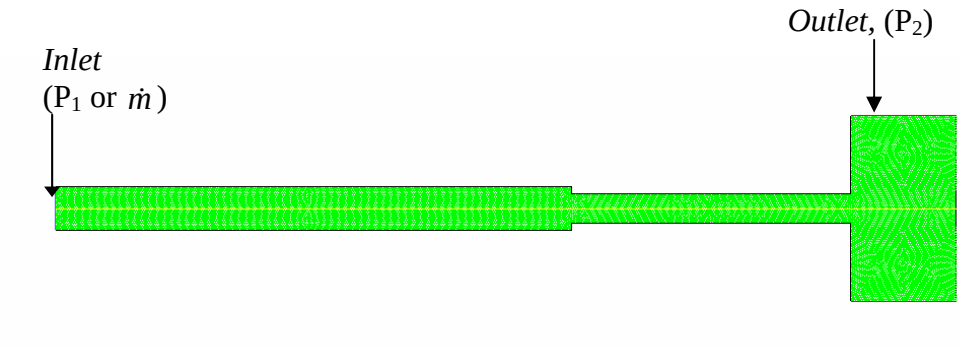

Figure 24. Radial pressure drop model for steady flow with meshing.

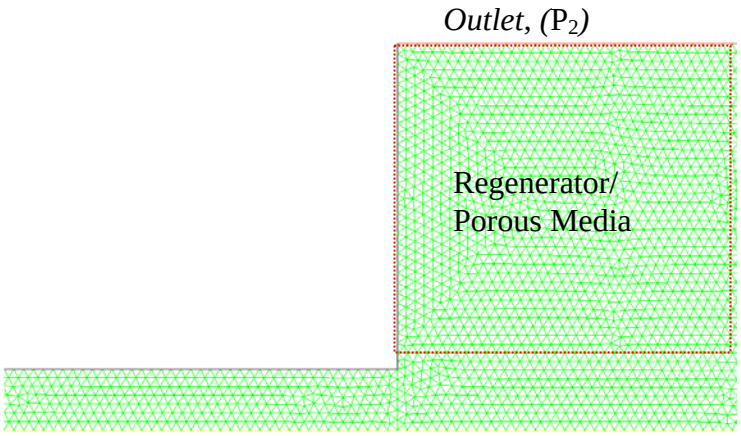

Figure 25. Detail mesh view of radial test section with annular regenerator.

All the simulations were performed using a residual convergence criterion of 1.0e-8 for the mass, *x*-velocity, *r*-velocity, and energy. Second Order Upwind Discretization

Scheme (SOUDS) was initially applied to the above mentioned continuum based conservation equations (4-32) ~ (4-37). However, much better residual convergences were noticed using the First Order Upwind Discretization Scheme (FOUDS). Thus, all CFD models were re-simulated using the FOUDS.

The physical dimensions of the radial test section for steady flow tests are summarized in Table 3 and in Figure 26 according to their component index notations.

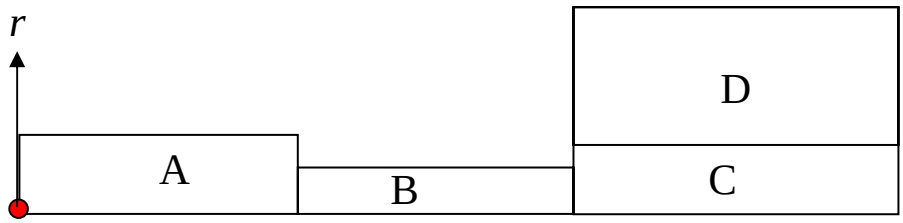

Figure 26. Component index notation of radial test section for steady flow.

Table 3.Component radiuses and lengths of steady flow radial test section.

Component index	Radius, *r*, (m)	Length (m)
A (Transfer line)	0.002286	0.05588
B (Transfer line)	0.0015875	0.022543
C (Inner section of annular regenerator)	0.002	0.01143
D (Annular regenerator)	0.01	0.01143

4.3.2 CFD Model for Oscillatory Radial Flow

The models for oscillatory radial flow are now discussed. The test apparatus shown in Figure 9 is modeled to simulate a radial pressure drop experiment in oscillatory flow. All the components appearing in Figure 9 were not modeled for this simulation, however, and instead only the components that appeared after pressure measurement

location, P_1, were modeled and simulated. Experimentally measured pressure values at location P_1 are imposed in the model as the boundary condition to simulate oscillatory flow conditions. Due to the transient nature of oscillatory flow, time dependent continuum based conservation equations were used to model the test apparatus.

Similar to what was described in the previous section the simulated system had two different parts (purely fluid part and porous media part). For the open (purely fluid) parts Eqs. (4-1), (4-2), and (4-3), which represents the mass, momentum, and energy conservation equations, respectively, were used. For the porous region, Eqs., (4-6), (4-7), and (4-8), which represent the single phase volume-averaged mass, momentum, and energy conservation equations, were used. When applicable, the k-epsilon turbulence model was also applied.

As mentioned earlier, the UDF feature in Fluent provides capability of imposing time dependent flow and heat transport properties such as pressure, temperature, density, velocity, mass flow rate, etc, at any desired boundary of the model. In this investigation a transient pressure UDF was developed, and was coupled with the main CFD code in order to impose time dependent pressure inlet boundary conditions. Before aforementioned UDF was hooked and compiled to the code, experimentally measured pressure data were first transformed to the frequency domain form by Fast Fourier Transformation (FFT) and were represented as Fourier Cosine Series. Using the first three harmonics of magnitudes and phases, actual measured pressure waveforms were replicated. The transformed pressures were then represented using the following expressions:

$$P_1(t) = \Gamma_1 \cos(\Omega_1 t + \Delta_1) + \Gamma_2 \cos(\Omega_2 t + \Delta_2) + \Gamma_3 \cos(\Omega_3 t + \Delta_3)$$

$$\Omega_n = n\omega, \quad \omega = 2\pi f, \quad n = 1, 2, 3 \tag{4-38}$$

Using a UDF, the exact mathematical function represented by Eqn. (4-38) could be imposed at the inlet of the regenerator to simulate the pressure oscillations. Detailed description of this UDF code is shown in Appendix A.

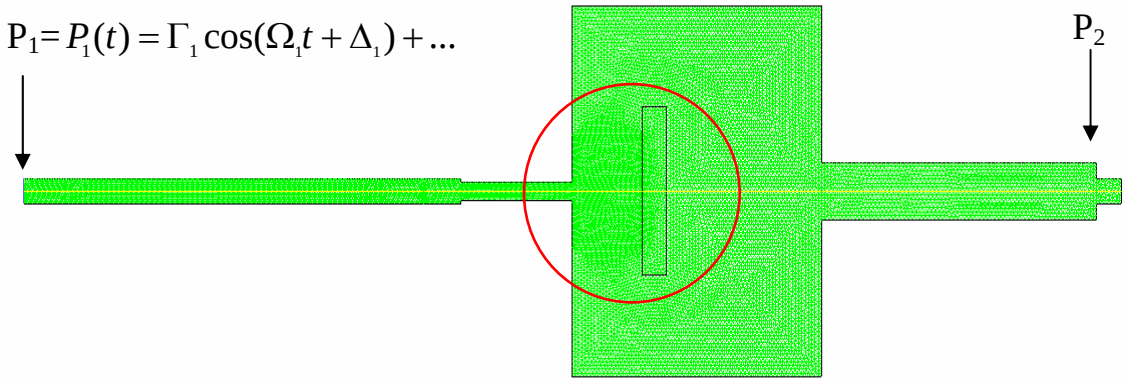

Figure 27. Radial pressure drop model for oscillatory flow with meshing

CFD simulations for the annular test section depicted in Figure 9 were performed using approximately 7000 mesh nodes. The grid and meshing representation of the model is shown in Figures 27 and 28.

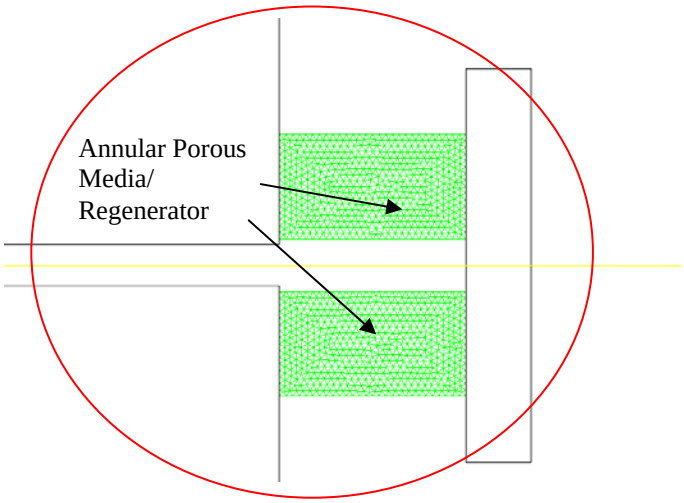

Figure 28. Detail view of annular porous region

SOUDS (Second Order Upwind Discretization Scheme) and PISO (Pressure-Implicit with Splitting of Operators) pressure-velocity coupling scheme is used to perform the model simulations. The residual convergence criterion of 1.0e-4 for the mass, *x*-velocity, and *r*-velocity, and the criterion of 1.0e-6 for the energy were used. For the turbulence model, for both *k* and epsilon the criterion of 1.0e-3 were used.

Seven CFD simulations were performed using this model. Each simulation represented a specific oscillation frequency. The simulated frequencies were 5 Hz, 10 Hz, 20 Hz, 30 Hz, 40 Hz, 50 Hz, and 60 Hz, these frequencies of course represented the experiments.

The solution time increment plays a crucial role in obtaining fully converged solutions in any numerical analysis. Larger time steps are always desired for the purpose of minimizing the computation time. However, large time steps can lead to code divergence. Thus optimum time step must be found for each simulation. Near-optimal time steps were found by trial and error and are summarized in Table 4, and these values were used for the simulations.

Table 4. Summary of solution time steps.

Frequency (Hz)	Time steps (sec)
60	0.00016667
50	0.0002
40	0.00025
30	0.00033333
20	0.0005
10	0.0005
5	0.001

The physical dimensions of the model and component notations are shown in Table 5 and in Figure 29. Figure 29 is shown in the cylindrical coordinate system,

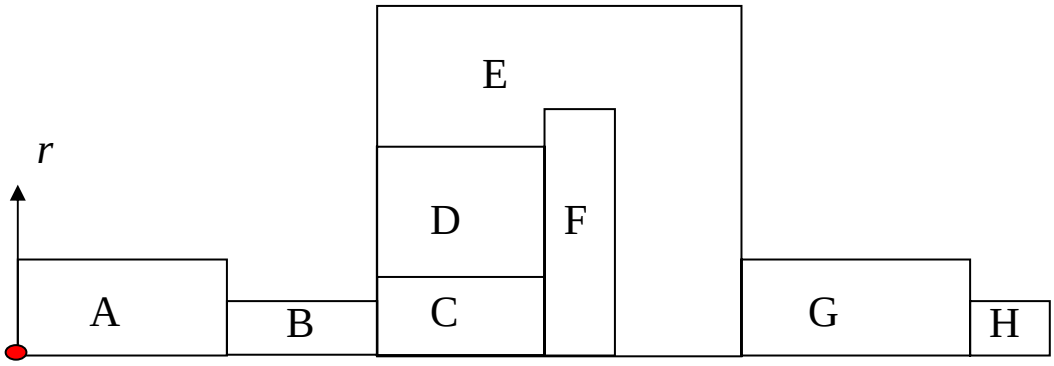

Figure 29. Component index notation of radial test section for oscillatory flow.

Table 5. Component radii and lengths of radial test section for oscillatory flow.

Component index	Radius, *r*, (m)	Length (m)
A (Transfer line)	0.002286	0.0889
B (Transfer line)	0.0015875	0.022543
C (Inner section of annular regenerator)	0.002	0.014275
D (Annular porous media)	0.01	0.014275
E (Buffer volume)	0.0330581	0.0508
F (Solid aluminum plate)	0.015	0.005
G (Transfer line)	0.00508	0.05588
H (Transfer line)	0.002286	0.00508

4.3.3 CFD Model for Axial Oscillatory Flow

For the CFD-based modeling of oscillatory axial flow, the RTS1 and RTS2 test sections depicted in Figures 14 and 17, respectively, are modeled using the fluid and energy transport conservation equations represented by Eqs. (4-1) ~ (4-8).

Given that the test apparatus is cylindrical and all the components are linearly aligned in series and form an axi-symmetric system, the entire test section is modeled in a 2-dimensional axi-symmetric coordinate system. Model nodalization and meshing is performed using Gambit software. The generated meshes are shown in Figures 30, 31, and 32 for RTS1 and Figures 33 and 34, for RTS2 system.

The boundary conditions for the tests, as well as the simulations included a known inlet time-dependent pressure, and isothermal and impermeable walls (at room temperature). A UDF function was again developed and implemented according to Eqn. (4-38) based on the measured pressure data. The developed UDF was thus coupled to the main CFD code in order to impose transient pressure boundary conditions at the inlet of RTS1 and RTS2 test sections. RTS1 and RTS2 were simulated using approximately 8300 and 9500 nodes, respectively.

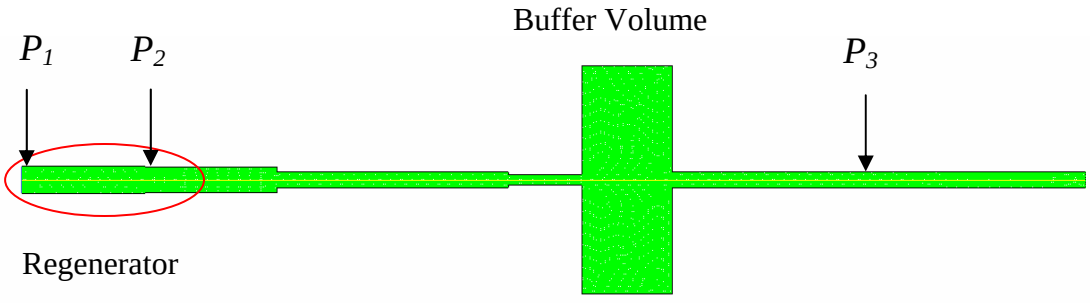

Figure 30. Oscillatory flow axial pressure drop model (RTS1) with meshing

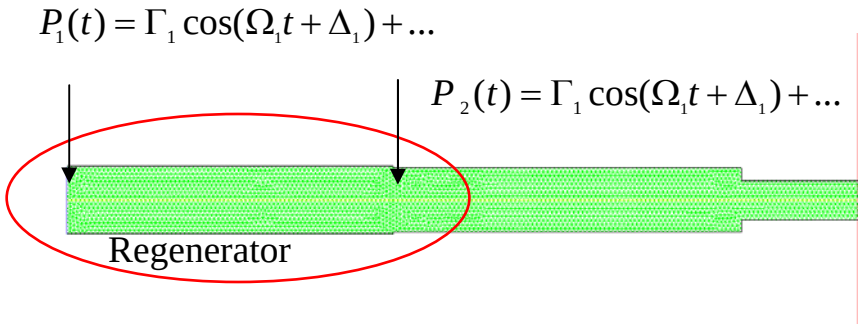

Figure 31. Detail view of the RTS1 regenerator section and imposed (P_1) and predicted (P_2) pressure locations.

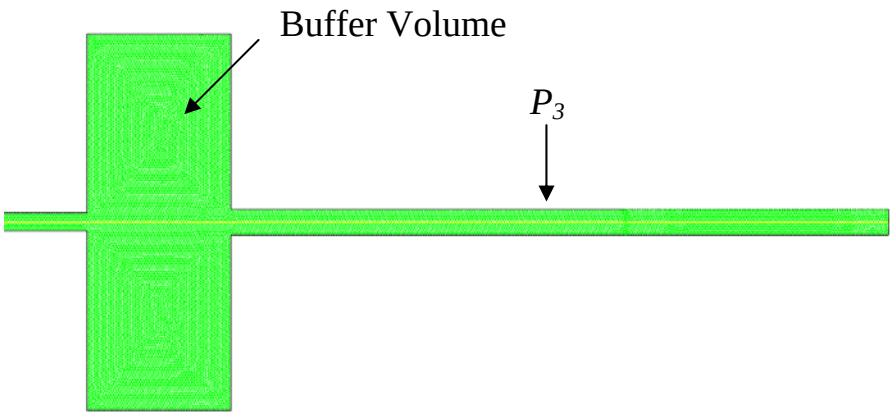

Figure 32. Detail view of the buffer volume and P_3 measurement location.

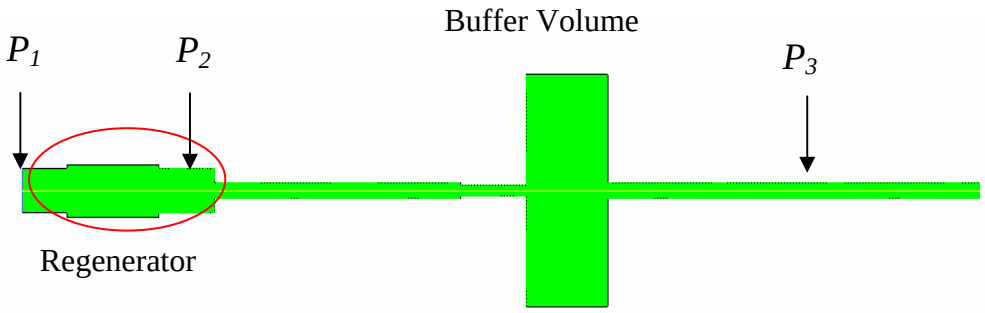

Figure 33. Oscillatory flow axial pressure drop model (RTS2) with meshing

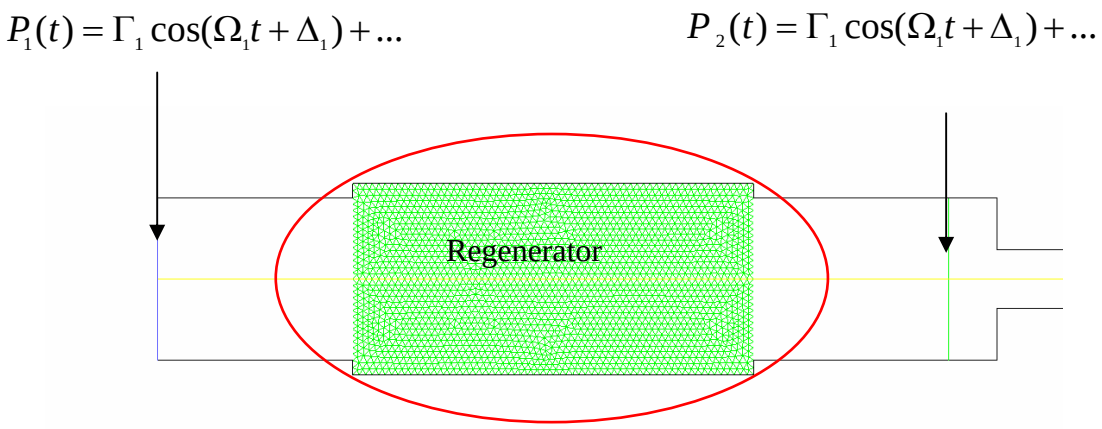

Figure 34. Detail view of the RTS2 regenerator section and imposed (P_1) and measured (P_2) pressure locations.

The discretization scheme of SOUDS and pressure-velocity coupling scheme of PISO are used for all the simulations. The scaled residual convergence criterion of 1.0e-6 for the mass, *x*-velocity, and *r*-velocity; and the convergence criterion of 1.0e-7 for the energy, were used for all the simulations. The isothermal condition of 300 K was applied to the walls of the simulated models.

Similar to the cases described in the previous section a total of seven CFD simulations were performed using this model. Simulated frequencies were 5 Hz, 10 Hz, 20 Hz, 30 Hz, 40 Hz, 50 Hz, and 60 Hz. Table 6 displays the time steps used in these simulations.

Table 6. Summary of solution time steps for both RTS1 and RTS2.

Frequency (Hz)	Time steps (sec)
60	5.005e-5
50	6.006e-5
40	7.5075e-5
30	1.001e-4
20	7.5075e-5
10	8.3333e-5
5	9.0909e-5

The physical dimensions of the model and component index for RTS1 and RTS2 test section are shown in Table 7 and Figure 35, respectively. Note that Figure 35 is shown in the cylindrical coordinate system.

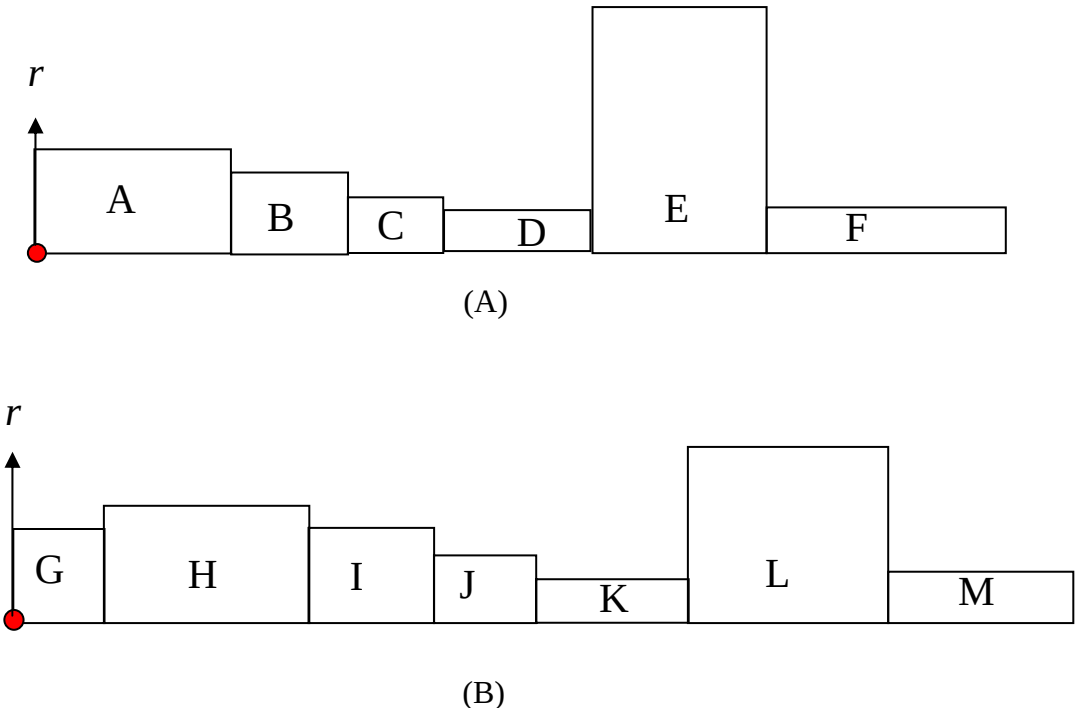

Figure 35. Component index notation of RTS1 (A) and RTS2 (B) test section.

Table 7. Component radiuses and lengths of RTS1 and RTS2 test section.

Component index	Radius, *r*, (m)	Length (m)
A (Regenerator)	0.0039688	0.0381
B (Transfer line)	0.00381	0.04064
C (Transfer line)	0.002286	0.07112
D (Transfer line)	0.0015875	0.022543
E (Buffer volume)	0.0330581	0.02794
F (Transfer line)	0.002286	0.127
G (Transfer line)	0.00635	0.01524
H (Regenerator)	0.007493	0.031394
I (Transfer line)	0.00635	0.01905
J (Transfer line)	0.002286	0.08382
K (Transfer line)	0.0015875	0.022543
L (Buffer volume)	0.0330581	0.02794
M (Transfer line)	0.002286	0.127

4.4 CFD Model for System-Level Parametric Study

The objective of this parametric study was to assess the impact of uncertainties associated with regenerator closure parameters on the system level performance of a typical ITPTC. This assessment was done by modeling and simulating the entire ITPTC system depicted in Figure 36 using different regenerator closure relations. The simulated model included a compressor, heat exchanger HX1 and HX2, a cold heat exchanger CHX, a pulse tube, inertance tube, and a buffer volume.

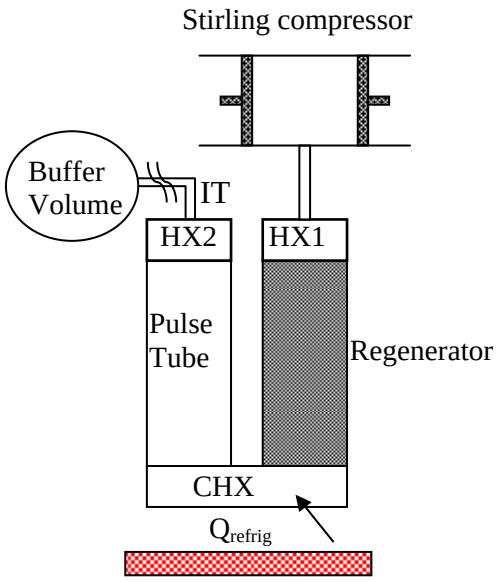

Figure 36. Schematic of Inertance Tube Pulse Tube Cryocooler (ITPTC).

The cold-head configuration depicted in Figure 36 is a U-shaped. However, to simplify the computational analysis, the U-shaped cold-head was modeled as a linear configuration, so that 2-D axi-symmetric flow could be assumed. The potential asymmetry caused by gravity and the change in flow direction by the bend are thus neglected. The gravity term however will be important if the order of magnitude of the acceleration becomes comparable with other terms (such as temporal acceleration, convective acceleration, viscous diffusion, etc.) in the momentum equation.

Once again, the general continuum-based conservation equations Eqs. (4-1) ~ (4-3), can be applied everywhere in the ITPTC system, except for the regenerator, CHX, HX1, and HX2, for the latter four components we apply Eqs. (4-6) ~ (4-8) which represent single phase volume-averaged mass, momentum, and energy equations for flow in porous media.

Eqs. (4-1) ~ (4-3) can be simplified given the axi-symmetric configuration of the modeled system. Assuming a negligible asymmetry caused by gravity and external body forces, the aforementioned equations can be cast in 2-dimensional cylindrical polar coordinate systems by the following:

The continuity is given by

$$\frac{\partial \rho}{\partial t} + \nabla \cdot \left(\rho \vec{u} \right) = \frac{\partial \rho}{\partial t} + \frac{\partial \rho}{\partial x}\left(\rho u_x \right) + \frac{\partial \rho}{\partial r}\left(\rho u_r \right) + \frac{\rho u_r}{r} = 0 \tag{4-39}$$

The axial and radial momentum conservation are given by, respectively,

$$\begin{aligned} \frac{\partial P}{\partial x} = & -\frac{\partial \left(\alpha \rho u_x \right)}{\partial t} - \frac{1}{r}\frac{\partial}{\partial x}\left(r \rho u_x u_x \right) - \frac{1}{r}\frac{\partial}{\partial r}\left(r \rho u_r u_x \right) + \\ & \frac{1}{r}\frac{\partial}{\partial x}\left\langle r\mu\left(2\frac{\partial u_x}{\partial x} - \frac{2}{3}\left[\frac{\partial u_x}{\partial x} + \frac{\partial u_r}{\partial r} + \frac{u_r}{r} \right] \right) \right\rangle + \frac{1}{r}\frac{\partial}{\partial r}\left\langle r\mu\left(\frac{\partial u_x}{\partial r} - \frac{\partial u_r}{\partial x} \right) \right\rangle \end{aligned} \tag{4-40}$$

$$\begin{aligned} \frac{\partial P}{\partial r} = & -\frac{\partial \left(\rho u_r \right)}{\partial t} - \frac{1}{r}\frac{\partial}{\partial x}\left(r \rho u_x u_r \right) - \frac{1}{r}\frac{\partial}{\partial r}\left(r \rho u_r u_r \right) + \frac{1}{r}\frac{\partial}{\partial x}\left\langle r\mu\left(\frac{\partial u_r}{\partial x} + \frac{\partial u_x}{\partial r} \right) \right\rangle + \\ & \frac{1}{r}\frac{\partial}{\partial r}\left\langle r\mu\left(2\frac{\partial u_r}{\partial r} - \frac{2}{3}\left(\frac{\partial u_x}{\partial x} + \frac{\partial u_r}{\partial r} + \frac{u_r}{r} \right) \right) \right\rangle - 2\mu\frac{u_r}{r^2} + \frac{2}{3}\frac{\mu}{r}\left\langle \frac{\partial u_x}{\partial x} + \frac{\partial u_r}{\partial r} + \frac{u_r}{r} \right\rangle + \rho\frac{u_\theta^2}{r} \end{aligned} \tag{4-41}$$

where u_θ is the swirl velocity. For all the forthcoming simulations swirl velocities will be set equal to zero for simplicity.

The fluid energy conservation is given by

$$\nabla \cdot \left(k \nabla T + \overline{\overline{\tau}} \cdot \vec{u} \right) - \frac{\partial (\rho E)}{\partial t} - \nabla \cdot \left(\vec{u} \left(\rho E + P \right) \right) = 0 \tag{4-42}$$

Porous media equations shown in Eqs. (4-6) ~ (4-8), can further be simplified given the axi-symmetric configuration of the modeled system. Again assuming a negligible asymmetry caused by gravity and external body forces, the aforementioned equations can be cast in 2-dimensional cylindrical polar coordinate systems by the following:

The single phase volume-averaged continuity, axial and radial momentum equations are respectively given by:

$$\frac{\partial (\alpha \rho)}{\partial t} + \nabla \cdot (\alpha \rho \vec{u}) = \frac{\partial (\alpha \rho)}{\partial t} + \frac{\partial \rho}{\partial x}(\alpha \rho u_x) + \frac{\partial \rho}{\partial r}(\alpha \rho u_r) + \frac{\alpha \rho u_r}{r} = 0 \tag{4-43}$$

$$\begin{aligned} \alpha \frac{\partial P}{\partial x} = & -\frac{\partial (\alpha \rho u_x)}{\partial t} - \frac{1}{r}\frac{\partial}{\partial x}(\alpha r \rho u_x u_x) - \frac{1}{r}\frac{\partial}{\partial r}(\alpha r \rho u_r u_x) + \\ & \frac{1}{r}\frac{\partial}{\partial x}\left\langle \alpha r \mu \left(2\frac{\partial u_x}{\partial x} - \frac{2}{3}\left[\frac{\partial u_x}{\partial x} + \frac{\partial u_r}{\partial r} + \frac{u_r}{r} \right] \right) \right\rangle + \frac{1}{r}\frac{\partial}{\partial r}\left\langle \alpha r \mu \left(\frac{\partial u_x}{\partial r} - \frac{\partial u_r}{\partial x} \right) \right\rangle + \\ & \frac{\mu}{\beta_x} u_x + \frac{C_x \rho}{2} |\vec{u}| u_x \end{aligned} \tag{4-44}$$

$$\alpha\frac{\partial P}{\partial r}=-\frac{\partial(\alpha\rho u_r)}{\partial t}-\frac{1}{r}\frac{\partial}{\partial x}(\alpha r\rho u_x u_r)-\frac{1}{r}\frac{\partial}{\partial r}(\alpha r\rho u_r u_r)+\frac{1}{r}\frac{\partial}{\partial x}\left\langle\alpha r\mu\left(\frac{\partial u_r}{\partial x}+\frac{\partial u_x}{\partial r}\right)\right\rangle+$$
$$\frac{1}{r}\frac{\partial}{\partial r}\left\langle\alpha r\mu\left(2\frac{\partial u_r}{\partial r}-\frac{2}{3}\left(\frac{\partial u_x}{\partial x}+\frac{\partial u_r}{\partial r}+\frac{u_r}{r}\right)\right)\right\rangle-2\alpha\mu\frac{u_r}{r^2}+$$
$$\frac{2}{3}\frac{\alpha\mu}{r}\left\langle\frac{\partial u_x}{\partial x}+\frac{\partial u_r}{\partial r}+\frac{u_r}{r}\right\rangle+\rho\frac{\alpha u_\theta^2}{r}+\frac{\mu}{\beta_r}u_r+\frac{C_r\rho}{2}|\vec{u}|u_r \tag{4-45}$$

where u_θ is the swirl velocity, α is the porosity, and all velocities are volume-averaged intrinsic velocities. The single phase volume-averaged energy equation is given by:

$$\nabla\cdot\left(\left(\alpha k_f+\lambda k_s\right)\nabla T+\left(\overline{\overline{\tau}}\cdot\alpha\vec{u}\right)\right)-\frac{\partial}{\partial t}\left(\alpha\rho_f E_f+\lambda\rho_s E_s\right)-\nabla\cdot\left(\alpha\vec{u}\left(\rho_f E_f+P\right)\right)=0 \tag{4-46}$$

where $\lambda=(1-\alpha)$.

Nodalization and grid representation of the simulated ITPTC model is depicted in Figure 37. Simulations were performed using approximately 8300 mesh nodes.

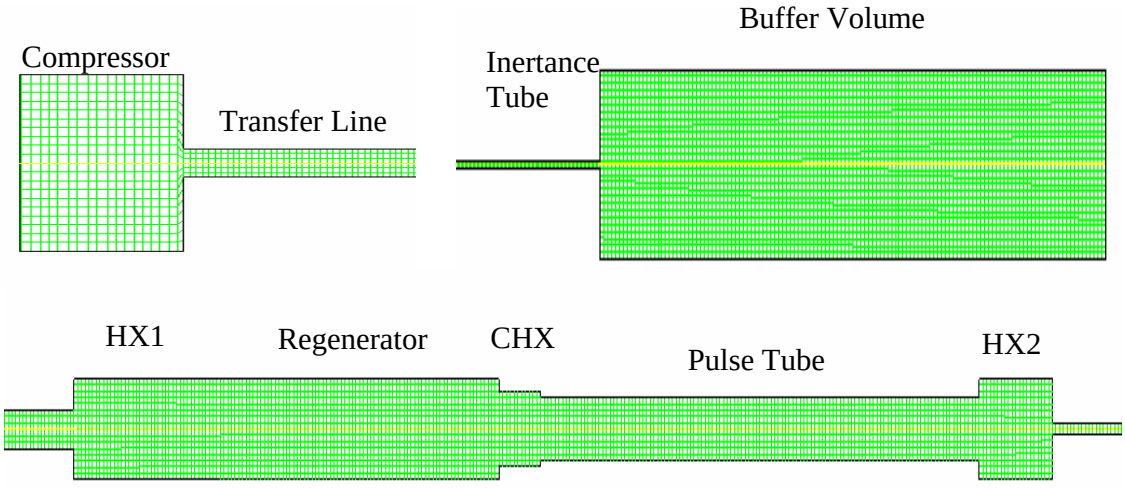

Figure 37. Node representation of simulated ITPTC system.

The physical dimensions of the entire ITPTC system are summarized in Table 8 and Figure 38.

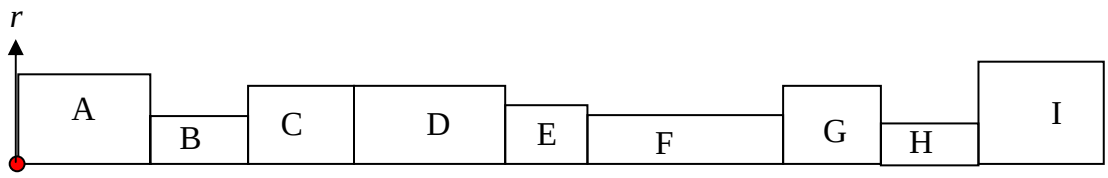

Figure 38. Component index of ITPTC system.

Table 8. Component radiuses and lengths of ITPTC.

Component index	Radius, *r*, (m)	Length, (m)
A (Compressor)	0.00954	0.0075
B (Transfer line)	0.00155	0.101
C (HX1)	0.004	0.02
D (Regenerator)	0.004	0.0381
E (CHX)	0.003	0.0057
F (Pulse tube)	0.0025	0.06
G (HX2)	0.004	0.01
H (Inertance tube)	0.000425	0.6841
I (Buffer volume)	0.013	0.13

Once again, SOUDS and PISO pressure-velocity coupling scheme are used to perform the model simulations. A residual convergence criterion of 1.0e-5 for the mass, *x*-velocity, and *r*-velocity, and a residual convergence criterion of 1.0e-7 for the energy, were used. A time step of 0.0005 seconds was used to march the solution in time.

A Fluent user-defined functions (UDF) is available that provides for dynamic meshing feature in Fluent. This UDF was utilized to model the compressor. This dynamic feature in Fluent is fairly new and it allows the user to simulate volume compression and expansion in the fluid volume using deformable meshing method. For this investigation, one of the compressor walls was modeled as a moving piston wall using the aforementioned dynamic meshing feature to compress and expand the fluid volume in the compressor. A detailed description of the UDF code that is used for imposing moving piston head motion can be found in Appendix A. A sinusoidal piston stroke of 6.5 mm (zero to peak) was imposed in the compressor for all the simulations.

The most common method for CFD simulation of a steady-state process is to perform a transient analysis using appropriate boundary conditions, and continue with the transient simulation until a steady-state numerical solution is obtained. Accordingly, although only the system's steady periodic operational results are of interest, the ITPTC model was simulated using a transient analysis. One of the advantages of transient analysis is the capability of predicting the actual cooling time. Periodic-steady conditions are assumed when all system parameters are repeated from one cycle to the next within acceptable margins. Adiabatic wall boundary condition is assumed for all the walls in the system except for the ones that are listed in Table 9. The boundary conditions and initial temperatures of the aforementioned system are summarized in Table 9.

Table 9. Boundary and initial conditions and regenerator closure relations for the modeled ITPTCs.

IPTPC Model	Oscillatory Friction Factor					Steady Friction Factor				
HX1 Wall [^{o}K]	293	293	293	293	293	293	293	293	293	293
HX2 Wall [^{o}K]	293	293	293	293	293	293	293	293	293	293
Regenerator Type	325 Mesh	400 Mesh	400 Mesh Sintered	Foam Metal	Micro-machined Disks	325 Mesh	400 Mesh	400 Mesh Sintered	Foam Metal	Micro-machined Disks
Regenerator Material	Stainless Steel	Stainless Steel	Stainless Steel	Stainless Steel	Nickel	Stainless Steel	Stainless Steel	Stainless Steel	Stainless Steel	Nickel
β [m^2]*	6.4247 E-11	2.5295 E-11	1.9828 E-11	3.7689 E-11	4.0000 E-11	4.2553 E-11	3.6101 E-11	1.8018 E-11	3.7736 E-11	4.3478 E-11
C [1/m]*	67000	120000	110000	66000	192000	47000	73000	260000	99000	115000
Regenerator Porosity	0.692	0.692	0.6147	0.5547	0.268	0.696	0.696	0.6147	0.5547	0.268
CHX, HX1, and HX2 material	Copper	Copper	Copper	Copper	Copper	Copper	Copper	Copper	Copper	Copper
β_c [m^2]	1.345 E-9	1.345 E-9	1.345 E-9	1.345 E-9	1.345 E-9	1.345 E-9	1.345 E-9	1.345 E-9	1.345 E-9	1.345 E-9
C_c [1/m]	8147	8147	8147	8147	8147	8147	8147	8147	8147	8147
CHX, HX1 and HX2 Porosity	0.68	0.68	0.68	0.68	0.68	0.68	0.68	0.68	0.68	0.68
Initial CHX Temperature [^{o}K]	300	300	300	300	300	300	300	300	300	300
CHX LOAD (W)	0	0	0	0	0	0	0	0	0	0

*These values were obtained from the forthcoming correlations.

CHAPTER 5

RESULTS AND DISCUSSION

In this chapter the experimental measurement results obtained with the test apparatus described in Chapter 3 are presented and discussed. Using the experimental measurements, furthermore, the steady and oscillatory anisotropic hydrodynamic parameters, namely, the Darcy permeability and Forchheimer's inertial coefficients of widely used PTC regenerator fillers are calculated and presented. These hydrodynamic parameters are calculated using the CFD analysis methods described in Chapter 4. The local directional (axial and radial/lateral) hydrodynamic parameters are also empirically correlated in the form of directional dimensionless friction factors as a function of appropriately defined Reynolds numbers. An assessment of the impact of the uncertainties associated with regenerator closure relations on the system level performance of a typical ITPTC system is also performed and reported.

5.1 Radial Pressure Drop Test Results for Steady Flow

Using helium as the working fluid, steady-state pressure drops were measured over a wide range of flow rates in annular test sections that contained regenerator fillers. The tests were performed in the apparatus described in Section 3.1, and the experimental data were analyzed using CFD simulations according to Section 4.3.1. The aforementioned hydrodynamic parameters were then obtained by comparing the data with

the results of CFD calculations that simulated the test sections and their vicinity. CFD simulations of the experiments were performed iteratively, whereby permeability and Forchheimer coefficient that brought about agreement between data and simulation results were calculated.

Five radial pressure drop test series were conducted with stainless steel 325 mesh screens, using two porosities: 0.696 and 0.632. The sintered 400 mesh sample was also tested and the corresponding pressure drops were measured. The measured data are shown in Figure 39. Each series was conducted by varying the steady state mass flow rate

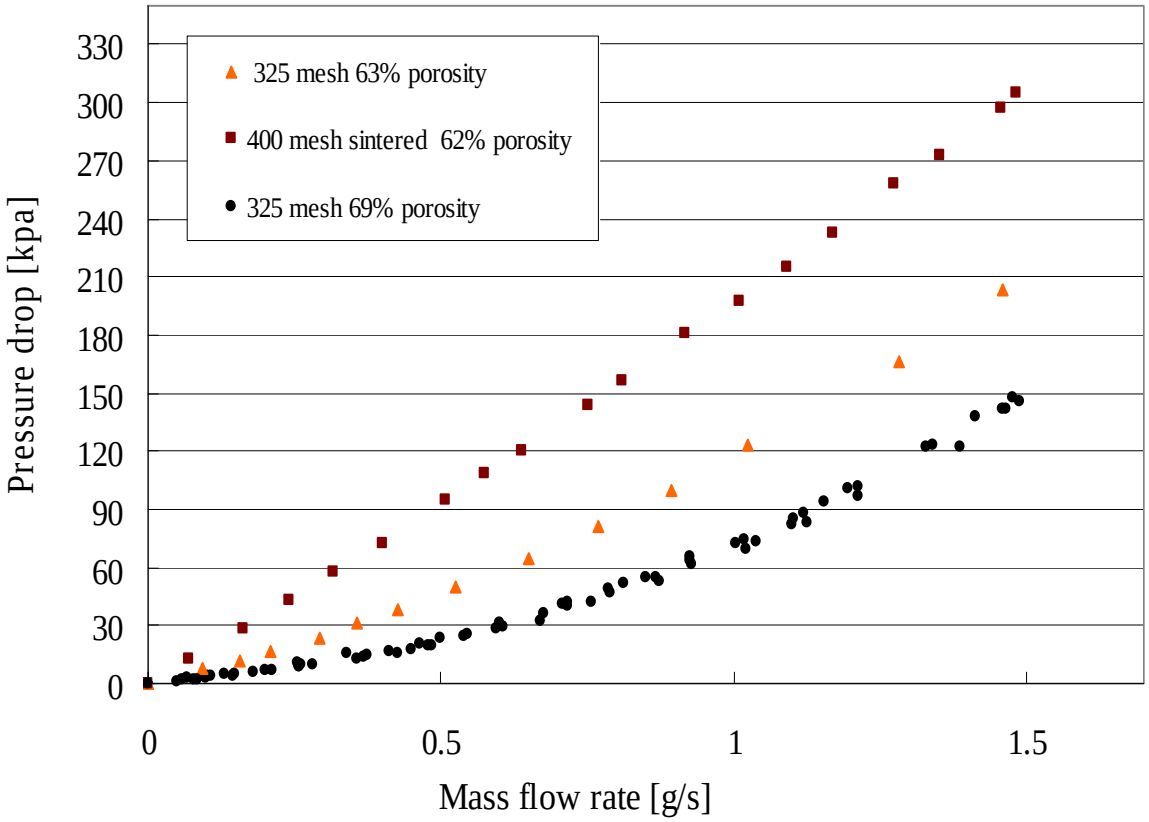

Figure 39. Experimental radial pressure drops for 325 mesh stacked screens and 400 mesh sintered regenerator filler.

with valve V1 (as shown in Figure 7), starting from a very low value and increasing the flow rate by increments, and measuring the pressure at P_1 (shown in Figure 7). Three of

test series were repetitive, and were performed with the test section with porosity 0.696, to examine data reproducibility. As noted in Figure 39, excellent reproducibility was achieved. The fourth test series was carried out with a regenerator with a porosity of 0.632. In Figure 40, for α = 0.69, the total measured pressure drop ($P_1 - P_{atm}$), as well as the pressure drop across the porous annular structure (defined as $P_C - P_{atm}$, with P_C representing the pressure of point *C* in Figure 6), are shown. The latter pressure drop is the results of the forthcoming CFD simulations.

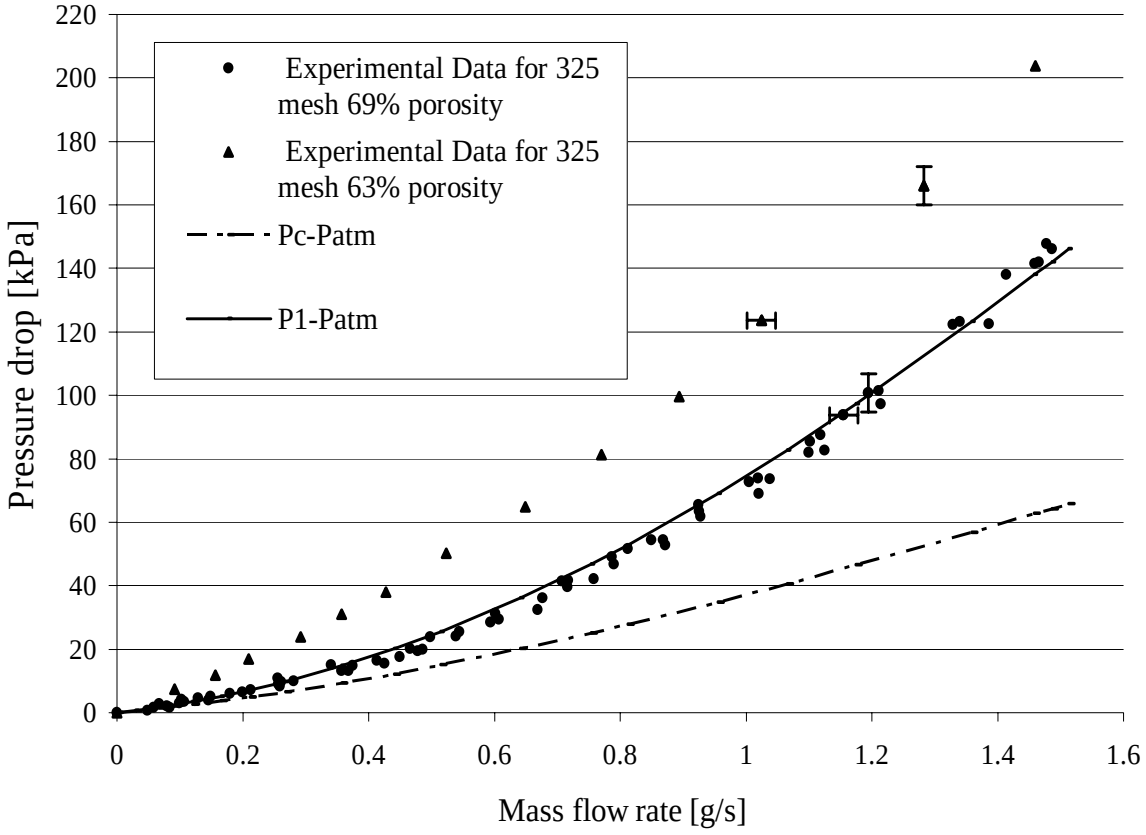

Figure 40. Experimental radial/lateral pressure drops and simulated results.

CFD Simulations were performed for the tests with α = 0.69. Harvey [1] previously measured the axial flow parameters for an identical porous matrix with α = 0.69, and obtained β_x =*5.0711e-11* m^2 and C_x =*61330* m^{-1}. These values were used here

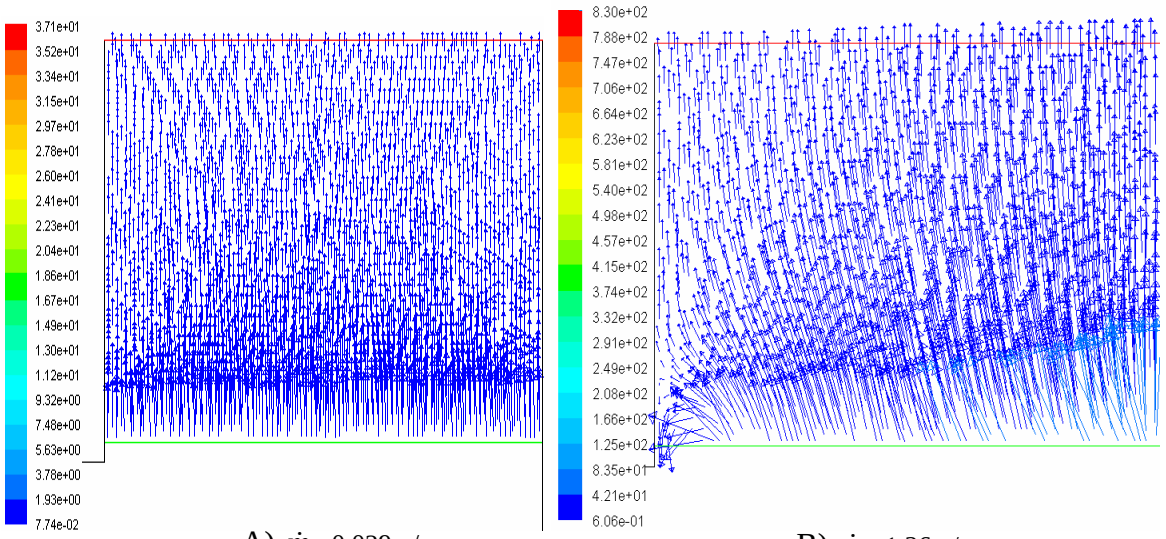

A) $\dot{m}$ =0.029 g/s B) $\dot{m}$ =1.36 g/s

Figure 41. Steady velocity vectors [in m/s] in the regenerator with α = 0.696.

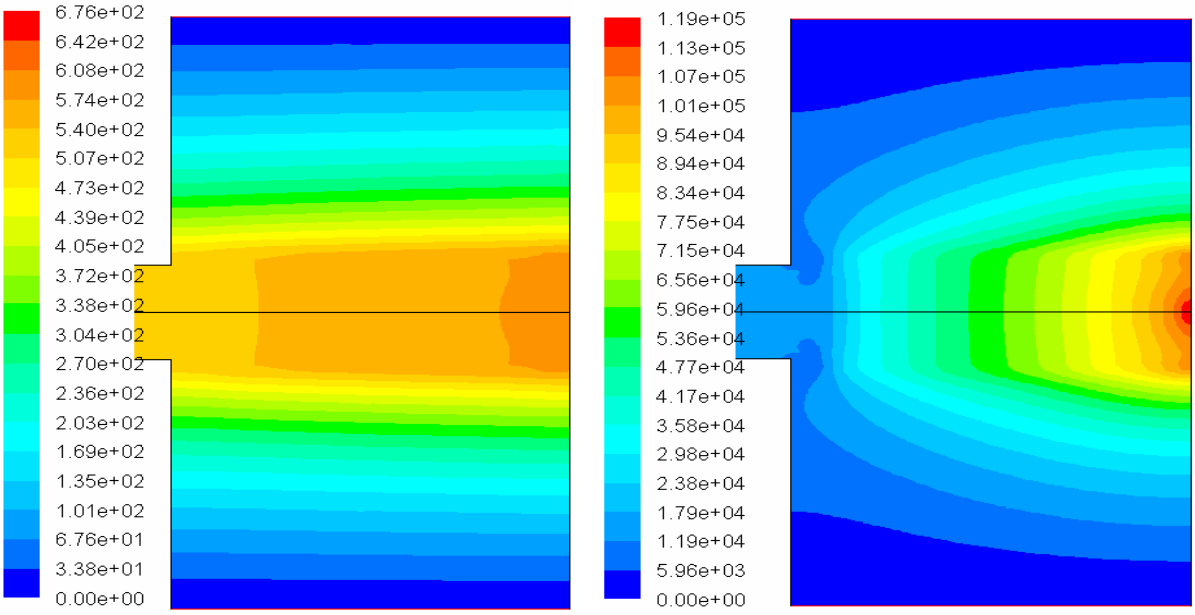

A) $\dot{m}$ =0.029 g/s B) $\dot{m}$ =1.36 g/s.

Figure 42. Simulated pressure contours [in Pa] for α = 0.696.

in the simulation of the tests with α = 0.696. Simulations were iteratively repeated by adjusting β_r and C_r. Very good agreement between data and simulation results was

obtained with β_r = *1.4705e-10* [m^2] and C_r = *98600* [m^{-1}]. Figure 40 compares the measured total pressure drops with results of the simulations with the latter parameter values. As noted, β_r is approximately 3 times larger than β_x, confirming the importance of anisotropy in the tested filler. The steady radial hydrodynamic parameters correlation results are summarized in Table 10.

Table 10. Results of steady radial hydrodynamic parameters for SS 325 mesh.

Annular regenerator	β_r [m^2]	C_r [1/m]	K_r [m^2]	$c_{f,r}$ [-]
325 mesh screens	1.4705e-10	98600	7.0011e-11	1.256

Figures 41 and 42 depict the velocity vectors and pressure contours in the test section, respectively, for two typical simulations. As noted in Figure 41 (A), at very low mass flow rates the velocity vectors in the annular porous medium were approximately purely radial. At higher mass flow rates, represented by Figure 41 (B), however, significant two dimensional effects occurred near the blocked end of the test section. The stagnation process near the blocked end also produced a high-pressure region which can be easily recognized in Figure 42 (B). The occurrence of these complex, multi-dimensional flow effects only confirmed that correct extraction of the hydrodynamic parameters requires a detailed CFD-based analysis.

5.2 Radial Pressure Drop Test Results for Oscillatory Flow

A total of seven radial pressure drop tests were conducted using the 400 mesh sintered stainless steel regenerator with porosity of 62% and charge pressure of 3.2 MPa. Each test represented a fixed compressor frequency, and the seven tests covered the frequency range 5 to 60 Hz. In six of the tests (excluding a test at 5 Hz) the peak to peak sinusoidal voltage amplitude was first increased via the function generator, starting from a near-zero value, until either the maximum compressor piston displacement or the maximum current limit were reached. The voltage amplitude was then maintained constant and the pressures at P_1 and P_2 were recorded after steady periodic conditions were established (see Figures 10, 11, 12 for exact location of P_1 and P_2). For the 5 Hz frequency, however, low flow conditions were sought so that the permeability in Darcy flow conditions could be tested, therefore the peak to peak sinusoidal voltage amplitude was increased only sufficiently to ensure that pressure sensor signals were viable.

The recorded pressure data were steady periodic. In order to simplify the analysis, they were first transformed to the frequency domain by Fast Fourier Transforms (FFT), and were thereby represented as Fourier Cosine series. It was noticed that the first three harmonics were sufficient for the accurate replication of the actual measured waveforms. The measured steady periodic pressures could thus be represented as:

$$P_i(t) = \Gamma_1 \cos(\Omega_1 t + \Delta_1) + \Gamma_2 \cos(\Omega_2 t + \Delta_2) + \Gamma_3 \cos(\Omega_3 t + \Delta_3)$$
$$\Omega_n = n\omega, \quad \omega = 2\pi f, \quad n = 1, 2, 3 \tag{5-1}$$

where $i = 1$ and 2. Table 11 is a summary of all the parameters in the above equation.

CFD simulations were performed for all the measured data. The objective, as mentioned before, was to obtain the radial permeabilities and coefficients of inertia of the 400 mesh sintered regenerator by an iterative procedure. To do this, the axial permeability and coefficient of inertia were needed since the simulations were axi-symmetric two dimensional. The porous structure was assumed to be isotropic, due to the unavailability of axial flow parameters for the tested 400 mesh sintered regenerator at the time. The error caused by this assumption is likely to be small, however, because the simulation results indicate that axial flows were everywhere negligibly small in comparison with radial flows. A UDF for Fluent was developed, whereby, for each

Table 11. Experimentally measured radial pressure drop for 400 mesh sintered regenerator under oscillating flow using charged pressure of 3.2 MPa.

Freq (Hz)	5	10	20	30	40	50	60
P_1							
Γ_1, [Pa]	2456.1	40052.8	45161.1	50419.8	26913.3	17133.6	11912.1
Γ_2, [Pa]	6.3	196.4	119.0	467.2	274.5	153.5	105.7
Γ_3, [Pa]	158.3	1007.9	1385.3	3243.1	1364.5	850.0	604.3
Δ_1, [Deg]	-110.3	-115.8	-143.3	-158.5	-168.9	-176.7	176.6
Δ_2, [Deg]	-58.3	68.1	5.0	-78.8	-92.9	-121.4	-131.3
Δ_3, [Deg]	-153.7	53.4	-169.7	73.5	13.7	-33.4	-74.5
P_2							
Γ_1, [Pa]	2063.8	33762.8	37150.1	38584.1	20410.0	12834.2	8806.7
Γ_2, [Pa]	4.1	149.0	42.0	121.4	108.1	68.7	47.3
Γ_3, [Pa]	133.7	1014.0	620.2	414.5	56.4	74.8	64.2
Δ_1, [Deg]	-113.3	-122.8	-160.5	171.4	156.9	144.2	132.5
Δ_2, [Deg]	5.5	87.3	25.3	-154.4	-141.4	173.5	137.4
Δ_3, [Deg]	-161.5	36.1	-139.5	32.0	-111.0	161.4	116.6

frequency Eqn. (5-1) with parameters representing P_1 was applied as the inlet boundary condition of the corresponding CFD simulations with Fluent. The predicted CFD results for pressure amplitude and phase angle at P_2 could then be directly compared with the experimental data or Eqn. (5-1) with parameters representing P_2, for verification. Simulations were iteratively repeated by adjusting the radial hydrodynamic parameters β_r and C_r. Very good agreement between data and simulations results were obtained with β_r = 5.348e-12 m^2 and C_r = 240000 m^{-1}. The latter values were obtained based on the charge pressure of 3.2 MPa.

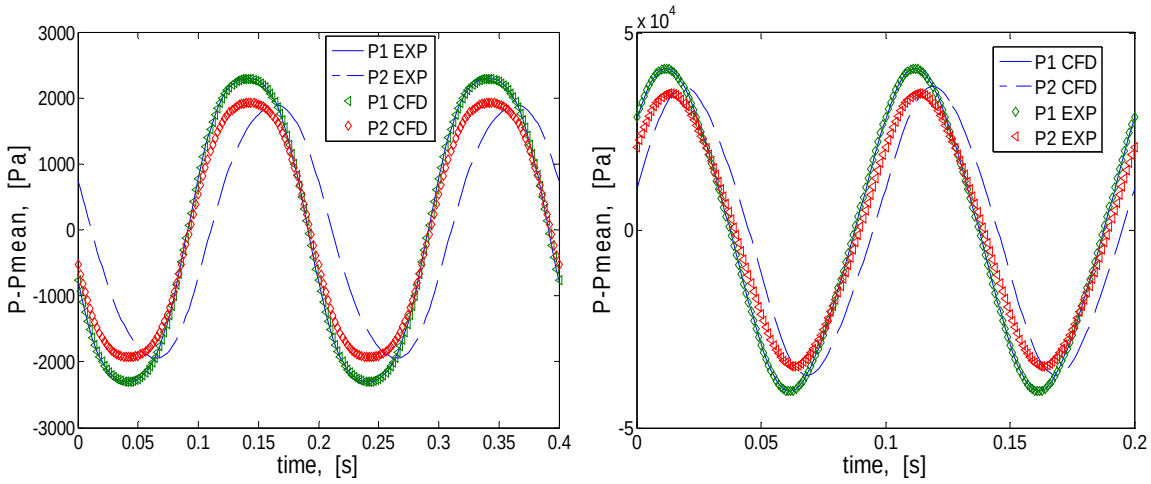

(A) (B)

Figure 43. Experimental oscillatory pressure drops and simulation results for 5 Hz (A) and 10 Hz (B).

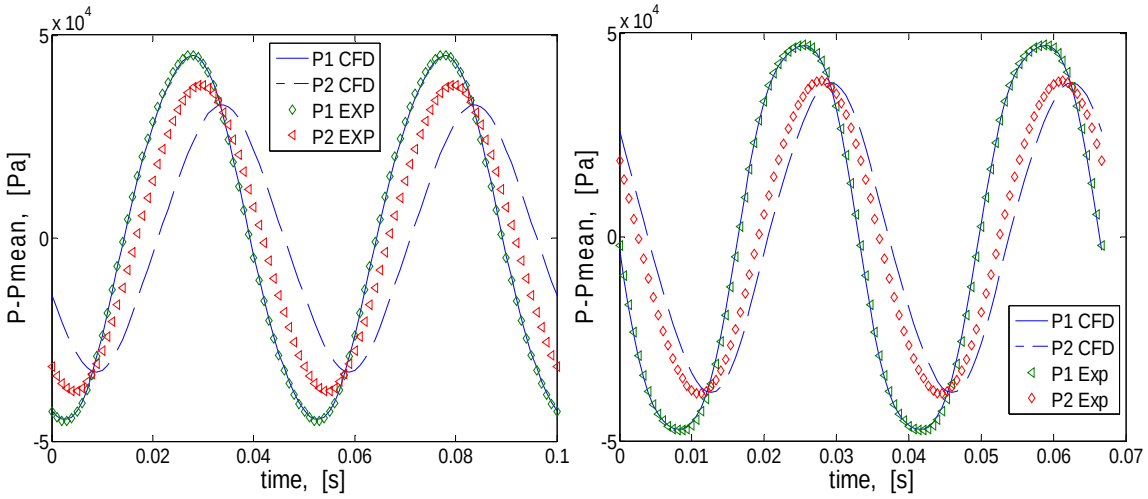

(A) (B)

Figure 44. Experimental oscillatory pressure drops and simulation results for 20 Hz (A) and 30 Hz (B).

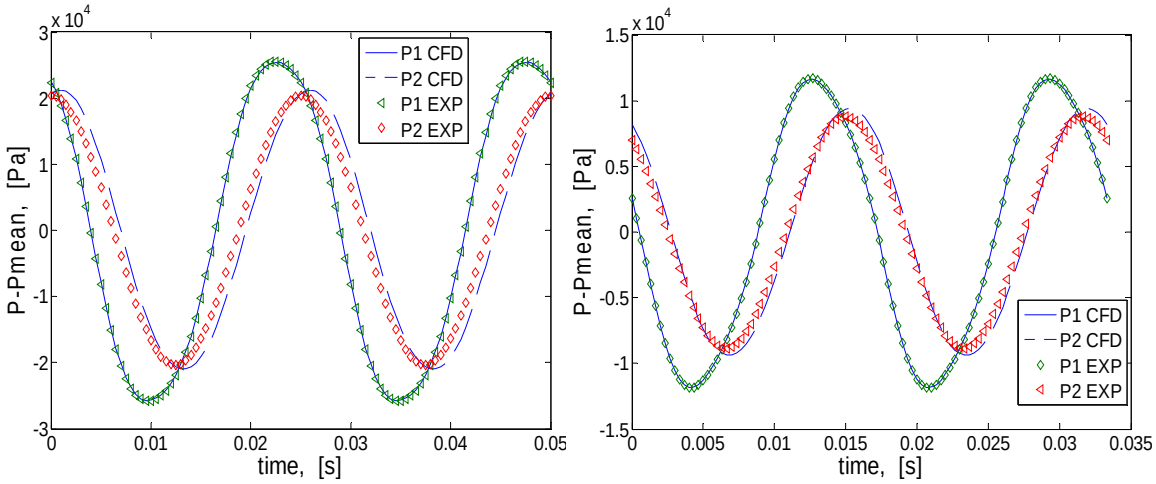

(A) (B)

Figure 45. Experimental oscillatory pressure drops and simulation results for 40 Hz (A) and 60 Hz (B).

Figures 43, 44, and 45, display comparisons between the experimental pressures at location P_2 with the pressures predicted by the simulations. These figures show that for frequencies of 30 Hz and higher the experimental data and simulation results are in

excellent agreement with respect to the pressure oscillation magnitude and phase. At the lower frequencies, 5 Hz, 10 Hz, and 20 Hz, however, the simulations over predict the phase difference between the pressure waves at the two locations. Thermo acoustic resonance in the test apparatus may be the possible explanation for this phase difference.

The pressure contours and velocity vectors of the sintered 400 mesh regenerator simulation for 40 Hz are depicted in Figures 46 and 47, respectively. As expected, most pressure drops occurred in the annular regenerator. The volume average fluid velocity vectors in the regenerator were purely one-dimensional in radial direction, and the effect of the fluid compressibility is illustrated through density contour plot in Figure 48. Very small density variations were observed for the 40 Hz simulation.

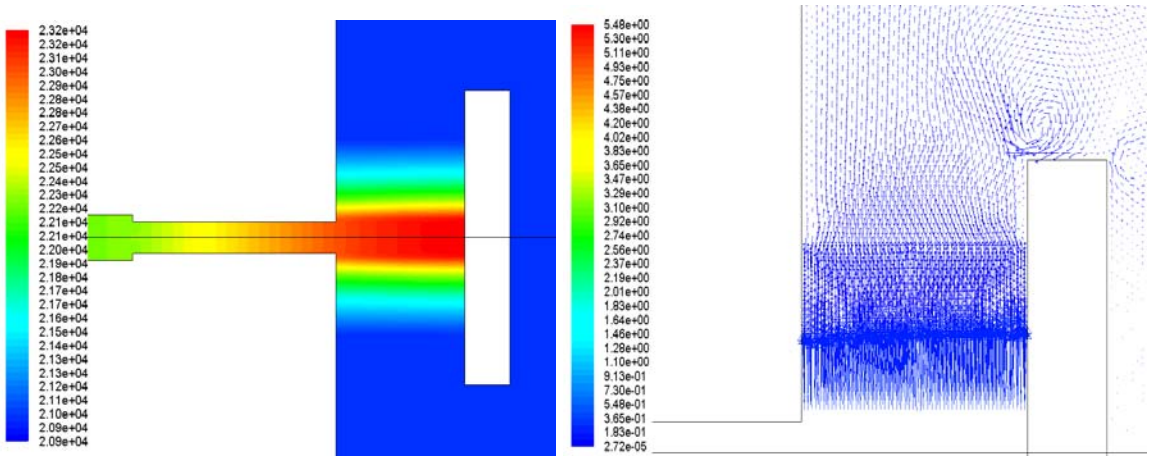

(A) (B)

Figure 46. Simulated regenerator pressure (A), in [Pa] and velocity vectors (B), in [m/s], in a snapshot for 40 Hz.

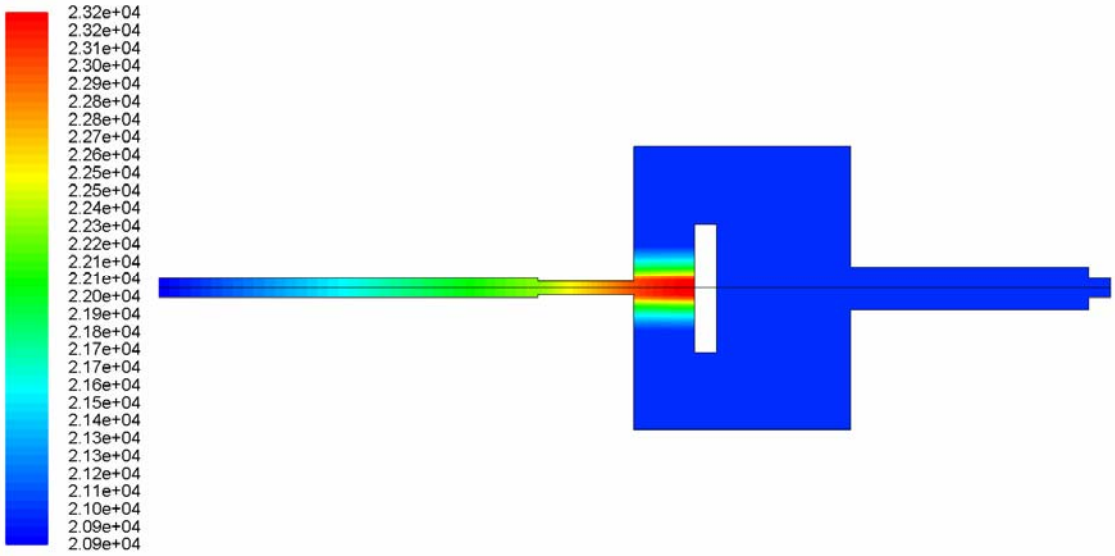

Figure 47. Contours of simulated pressure, in [Pa], in a snapshot for 40 Hz.

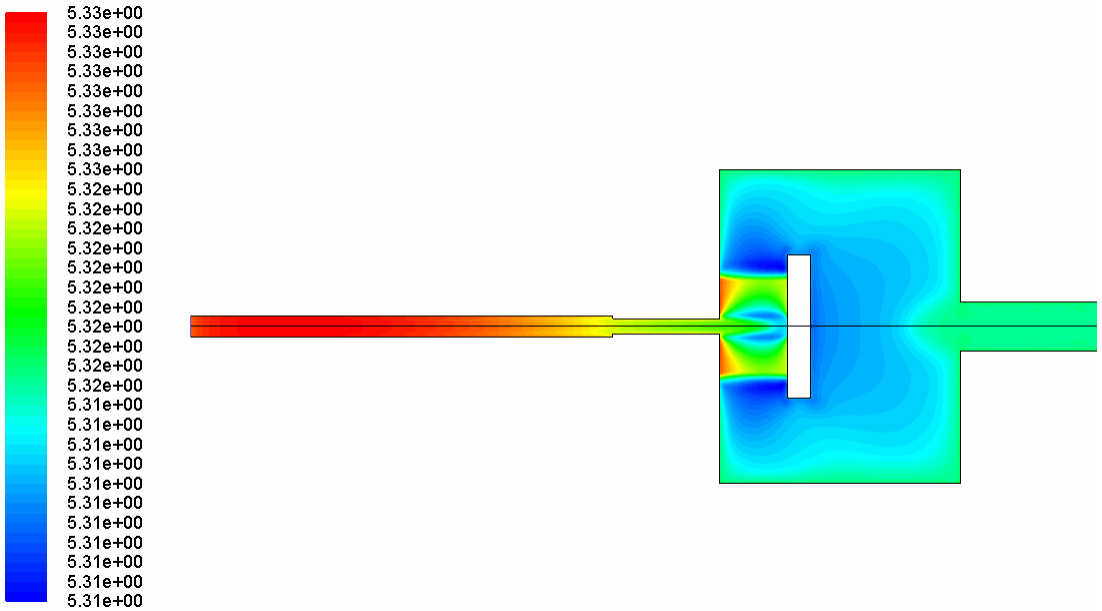

Figure 48. Contour of density, in [kg/m^3], in a snapshot for 40 Hz.

Recently, similar oscillatory radial pressure drop experiments were conducted using the same regenerator. For these experiments, the charge pressure of 2.78 MPa was used instead of 3.2 MPa. These experiments were performed in order to directly compare the radial and the axial hydrodynamic parameters, using identical charge pressures. The latter comparison will be presented in Section 5.5. The obtained data were analyzed following the steps just described. The experimental and simulation results are compared in Figures 49-52.

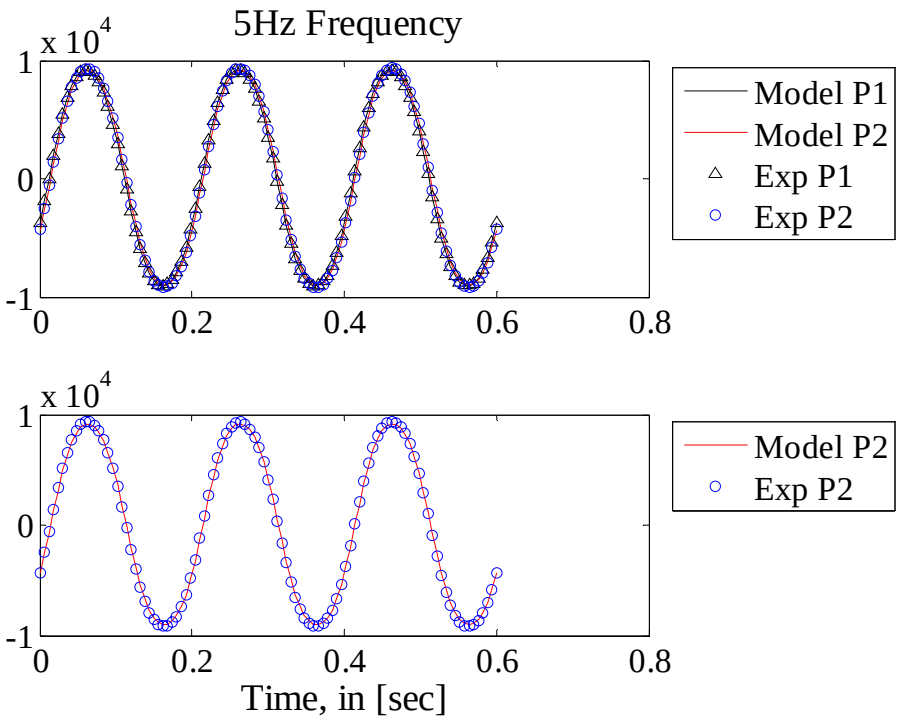

Figure 49. Prediction of pressure amplitude (P- P_{mean}), in [Pa] and phase at P_2, and their comparison to experimental data for sintered 400 mesh.

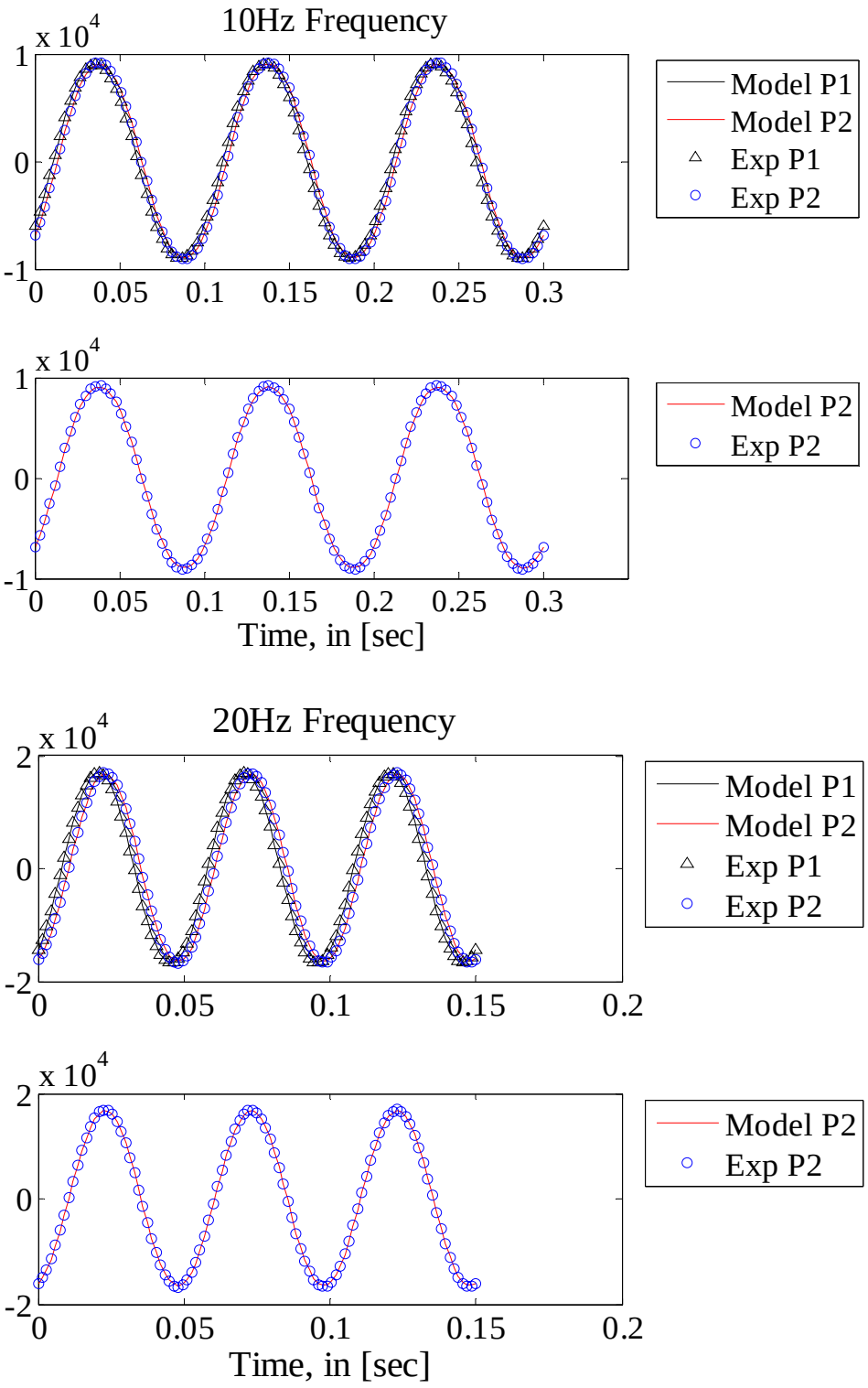

Figure 50. Prediction of pressure amplitude (P- P_{mean}), in [Pa] and phase at P_2, and their comparison to experimental data for sintered 400 mesh.

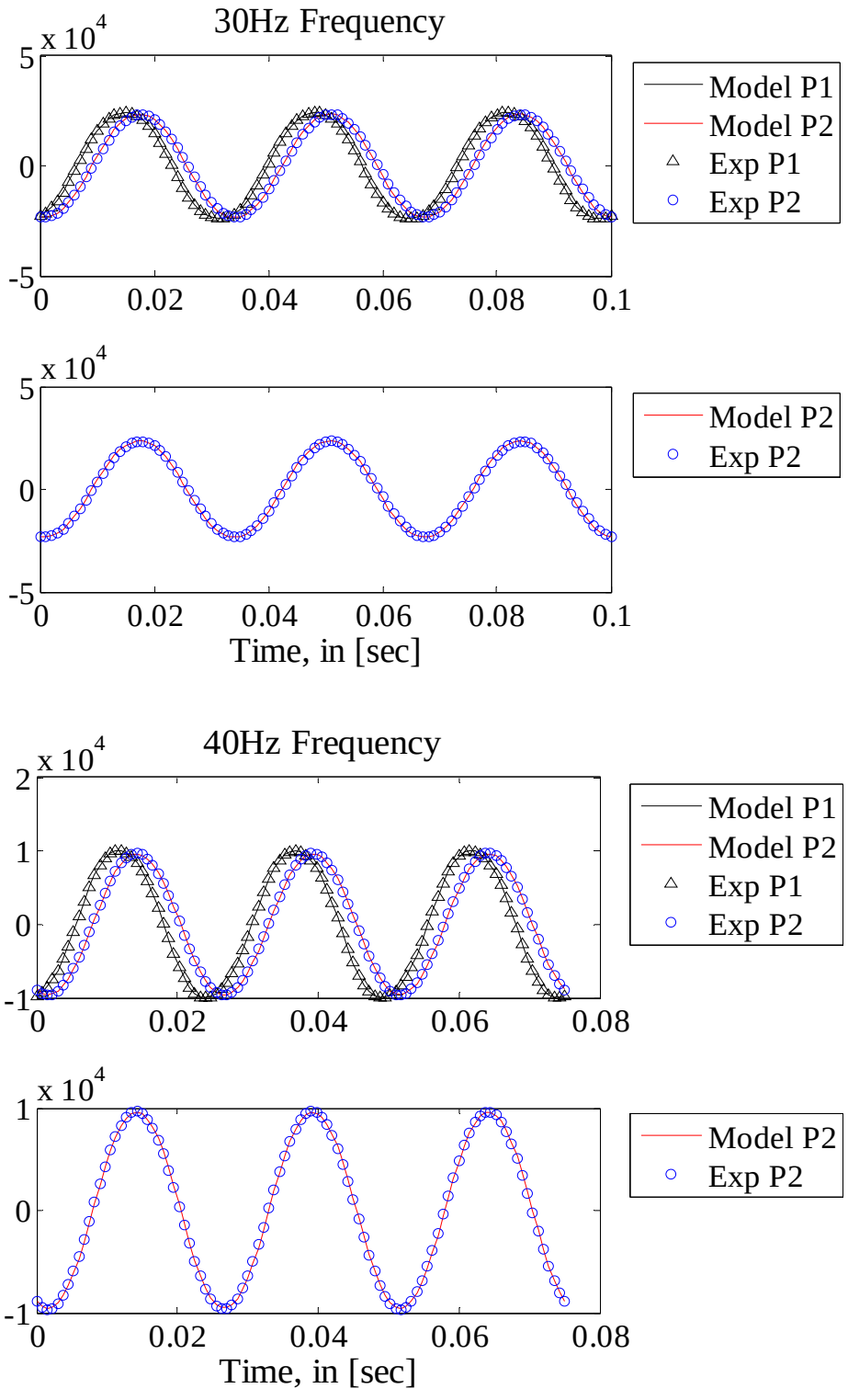

Figure 51. Prediction of pressure amplitude (P- P_{mean}), in [Pa] and phase at P_2, and their comparison to experimental data for sintered 400 mesh.

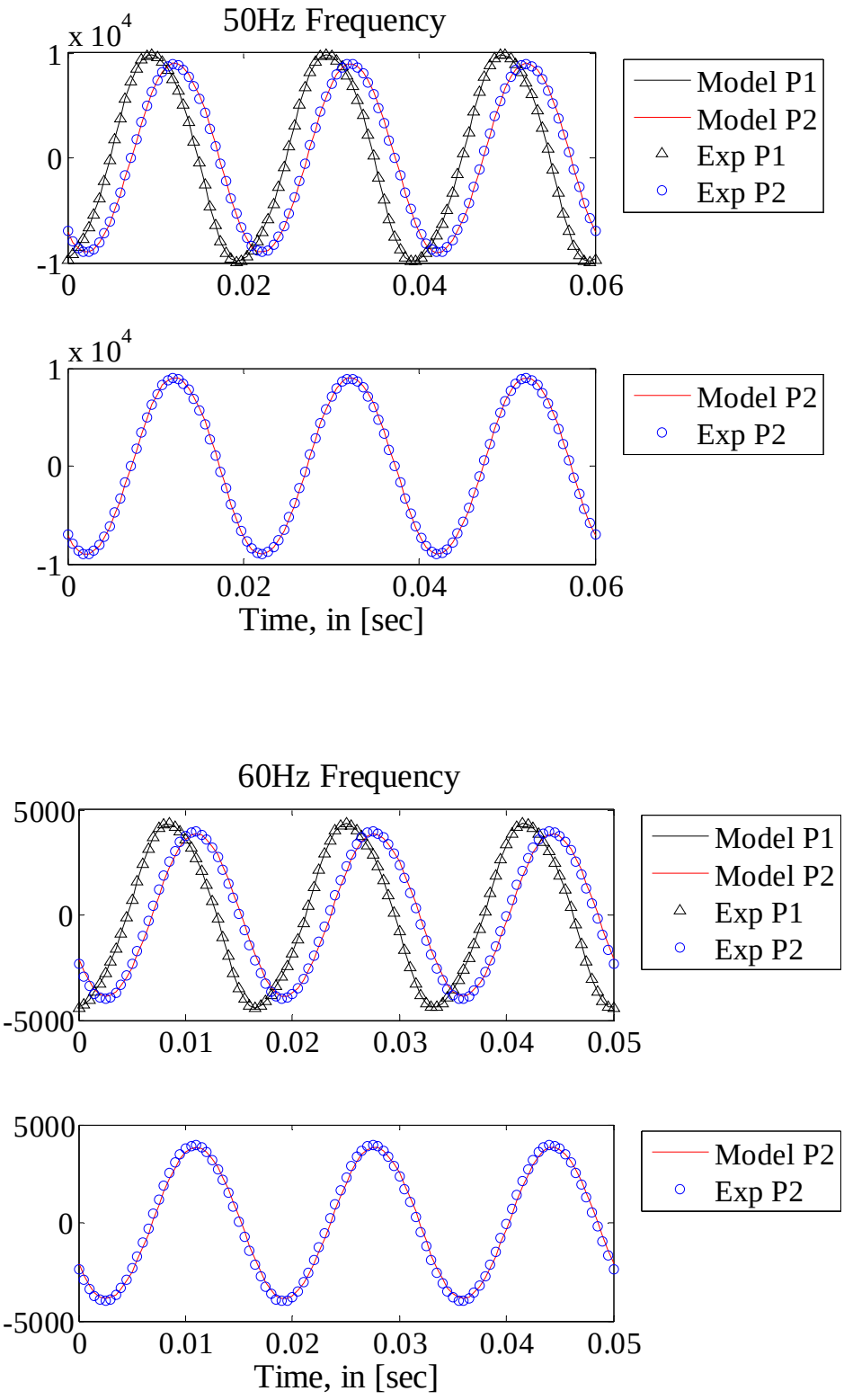

Figure 52. Prediction of pressure amplitude (P- P_{mean}), in [Pa] and phase at P_2, and their comparison to experimental data for sintered 400 mesh.

The simulation results shown in figures 49 through 52 were obtained using the 2.78 MPa charge pressure and β_r and C_r values listed in Table 13. Very good agreement between experimental data and simulated predictions were observed. The oscillatory radial hydrodynamic parameters correlation results for both 3.2 and 2.78 MPa are summarized in Table 12.

Table 12. Results of oscillatory radial hydrodynamic parameters using different charge pressure.

Annular regenerator	β_r [m^2]	C_r [1/m]	K_r [m^2]	$c_{f,r}$ [-]	Charge pressure, [MPa]
400 mesh sintered	5.34759e-12	240000	2.056e-12	0.7219	3.2
400 mesh sintered	6.66667e-12	200000	2.5627e-12	0.672	2.78

The results showed that a higher charge pressure produced a larger value of inertial coefficient $c_{f,r}$ and a smaller value of Darcy permeability K_r.

5.3 Axial Pressure Drop Test Results for Oscillatory Flow

Longitudinal hydrodynamic parameters that influence the pressure drop in a regenerator were empirically obtained using experimental data. Five regenerator fillers were tested using the apparatus shown in Figures 14 and 17. The pore characteristics and their physical dimensions of the tested regenerators are shown in Table 1.

The experimental conditions were similar to those described in the previous section. For each regenerator a total of seven oscillatory axial pressure drop tests were

conducted. Each test represented a fixed compressor frequency, and the seven tests covered the frequency range 5 to 60 Hz. In six of the tests (excluding a test at 5 Hz) the peak to peak sinusoidal voltage amplitude was first increased via the function generator, starting from a near-zero (50 milli-volts) value, until either the maximum compressor piston displacement or the maximum current limit were reached. The voltage amplitude was then maintained constant and the pressures at P_1, P_2, and P_3 were recorded after steady periodic conditions were established (see Figures 13 and 14 for the exact locations of P_1, P_2, and P_3). For the 5 Hz frequency, however, low flow conditions were sought so that the permeability in Darcy flow conditions could be tested, therefore the peak to peak sinusoidal voltage amplitude was increased only sufficiently to ensure that pressure sensor signals were viable.

The recorded pressure data were steady periodic. In order to simplify the analysis, they were transformed to the frequency domain by Fast Fourier Transforms (FFT), and were thereby represented as Fourier Cosine series. The first three harmonics were found to be sufficient for the accurate replication of the actual measured waveforms. The measured steady periodic pressures could thus be represented by Eqn. (5-1). Tables 13-18 summarize the coefficients in Eqn. (5-1). As expected, the magnitudes of the coefficients varied from filler to filler, and for each filler they depended on the frequency.

Table 13. Experimentally measured axial pressure drop for SS 400 mesh screens regenerator under oscillating flow.

Freq (Hz)	5	10	20	30	40	50	60
P_1							
Γ_1, [Pa]	5952.93	9578.44	8366.59	18306.82	12020.11	9124.57	8392.59
Γ_2, [Pa]	24.38	57.10	69.45	223.33	36.24	8.78	26.47
Γ_3, [Pa]	162.25	301.79	292.09	1047.76	662.06	447.30	375.98
Δ_1, [Deg]	-77.13	-87.06	-106.15	-119.06	-132.00	-144.87	-156.96
Δ_2, [Deg]	152.42	142.49	113.30	109.54	64.15	-100.47	-36.77
Δ_3, [Deg]	-119.47	138.96	123.12	43.78	-23.19	-80.52	-130.89
P_2							
Γ_1, [Pa]	5315.32	7068.02	4139.45	5332.75	2928.88	1877.28	1434.87
Γ_2, [Pa]	32.00	46.83	24.96	37.80	15.68	9.24	6.46
Γ_3, [Pa]	102.95	148.75	14.53	25.42	12.30	4.89	3.33
Δ_1, [Deg]	-96.56	-124.61	-164.29	169.90	154.09	138.91	124.72
Δ_2, [Deg]	153.51	114.58	61.37	54.38	41.00	9.44	-24.16
Δ_3, [Deg]	-174.07	36.10	-127.10	145.88	130.00	60.33	-68.54

Table 14. Experimentally measured axial pressure drop for SS 325 mesh screens regenerator under oscillating flow.

Freq (Hz)	5	10	20	30	40	50	60
P_1							
Γ_1, [Pa]	37016.06	56721.21	50152.29	103109.17	61626.50	45391.86	41798.90
Γ_2, [Pa]	170.29	329.88	421.38	1039.76	136.60	207.54	231.33
Γ_3, [Pa]	1004.77	1862.13	1984.14	6963.88	3985.42	2676.04	2403.10
Δ_1, [Deg]	-80.40	-92.57	-112.23	-122.33	-136.30	-147.89	-159.20
Δ_2, [Deg]	0.02	139.96	100.47	94.91	-28.34	-104.74	-153.49
Δ_3, [Deg]	-111.80	141.94	132.18	51.22	-18.11	-70.85	-121.73
P_2							
Γ_1, [Pa]	36699.41	48972.65	31634.80	39695.24	20689.59	13077.13	10067.37
Γ_2, [Pa]	229.67	265.53	181.36	269.40	75.64	39.52	37.74
Γ_3, [Pa]	799.48	1258.91	116.03	134.47	83.83	19.06	24.87
Δ_1, [Deg]	-94.19	-122.29	-162.76	171.68	154.54	140.09	126.18
Δ_2, [Deg]	155.06	110.80	56.11	67.19	42.45	18.25	-19.39
Δ_3, [Deg]	-158.31	47.98	-130.83	131.66	140.59	88.72	-89.36

Table 15. Experimentally measured axial pressure drop for SS 400 mesh sintered regenerator under oscillating flow.

Freq (Hz)	5	10	20	30	40	50	60
P_1							
Γ_1, [Pa]	37044.47	52871.78	78580.23	165070.90	117846.24	83308.07	69634.68
Γ_2, [Pa]	242.52	389.82	1112.46	3680.49	1625.48	606.74	342.11
Γ_3, [Pa]	1545.52	1546.68	2938.00	7337.10	4847.40	2910.38	2138.61
Δ_1, [Deg]	-81.78	-87.38	-103.46	-118.11	-133.94	-147.73	-160.06
Δ_2, [Deg]	-157.01	-71.01	124.11	119.15	86.11	59.71	38.10
Δ_3, [Deg]	-131.34	155.54	87.02	9.98	-61.23	-116.85	-164.03
P_2							
Γ_1, [Pa]	31467.92	31981.74	26187.83	31598.76	18059.39	10797.11	7581.53
Γ_2, [Pa]	267.38	223.82	206.23	432.30	176.13	84.25	44.49
Γ_3, [Pa]	657.42	256.54	101.16	241.43	111.20	38.83	17.16
Δ_1, [Deg]	-112.71	-138.43	-173.20	163.81	145.43	130.03	116.31
Δ_2, [Deg]	116.84	110.05	54.82	46.35	15.33	-28.98	-62.92
Δ_3, [Deg]	163.64	25.69	-113.91	152.39	101.67	28.08	-84.09

Table 16. Experimentally measured axial pressure drop for SS metallic foam regenerator under oscillating flow.

Freq (Hz)	5	10	20	30	40	50	60
P_1							
Γ_1, [Pa]	35974.72	32697.21	39487.63	117866.12	70639.06	48387.14	47183.37
Γ_2, [Pa]	216.49	312.11	458.12	1176.50	180.94	199.07	248.96
Γ_3, [Pa]	1162.28	970.78	2232.79	8121.91	4854.68	3191.80	2974.19
Δ_1, [Deg]	-94.15	-104.21	-113.84	-123.02	-136.06	-148.47	-159.06
Δ_2, [Deg]	-167.52	154.87	86.50	86.17	-14.40	-111.64	-174.55
Δ_3, [Deg]	-136.41	-170.11	105.19	31.39	-32.37	-85.70	-132.92
P_2							
Γ_1, [Pa]	34557.92	27614.24	22675.08	36920.53	19120.44	11451.10	9163.25
Γ_2, [Pa]	281.54	191.77	141.32	261.78	76.28	38.30	35.23
Γ_3, [Pa]	787.05	196.17	82.93	245.44	90.19	27.91	20.29
Δ_1, [Deg]	-109.76	-135.44	-167.94	166.66	150.90	136.30	123.32
Δ_2, [Deg]	153.97	104.65	38.72	52.61	36.83	-4.71	-27.46
Δ_3, [Deg]	161.02	54.33	-55.01	150.94	137.23	98.83	-102.11

Table 17. Experimentally measured axial pressure drop for Nickel micro-machined disks regenerator under oscillating flow.

Freq (Hz)	5	10	20	30	40	50	60
P_1							
Γ_1, [Pa]	41032.00	34392.00	49594.00	42863.00	32982.00	20542.00	15959.00
Γ_2, [Pa]	244.95	187.20	260.76	213.51	354.51	247.88	156.18
Γ_3, [Pa]	1413.40	222.06	1037.50	1718.10	1518.80	859.22	755.85
Δ_1, [Deg]	-90.76	-115.03	-139.79	-157.38	-165.79	-177.92	176.47
Δ_2, [Deg]	150.79	121.93	128.32	22.91	-30.36	-84.65	-141.29
Δ_3, [Deg]	-158.35	92.63	164.55	42.12	-28.13	-95.36	-116.74
P_2							
Γ_1, [Pa]	42067.00	34549.00	46236.00	36059.00	25214.00	14776.00	10348.00
Γ_2, [Pa]	274.39	130.89	120.75	88.77	49.95	28.66	34.77
Γ_3, [Pa]	1426.10	288.56	524.40	189.73	94.89	44.30	33.22
Δ_1, [Deg]	-95.55	-125.26	-161.93	170.87	155.68	138.80	126.78
Δ_2, [Deg]	148.31	110.92	47.21	-46.85	-155.69	117.23	102.39
Δ_3, [Deg]	-175.89	59.50	-169.63	64.50	12.72	-38.92	-101.19

Table 18. Experimentally measured axial pressure drop for SS 400 mesh screens regenerator under oscillating flow using 2.07 MPa charged pressure.

Freq (Hz)	5	10	20	30	40	50	60
P_1							
Γ_1, [Pa]	32716.42	56548.19	52022.04	111148.52	71047.03	54768.62	50459.80
Γ_2, [Pa]	192.27	379.59	519.60	1655.68	334.73	33.36	116.02
Γ_3, [Pa]	1041.76	2315.54	1450.56	5052.40	3076.12	2044.20	1668.80
Δ_1, [Deg]	-73.64	-82.96	-104.35	-119.86	-132.88	-146.19	-158.57
Δ_2, [Deg]	-164.39	168.78	114.99	106.58	62.71	31.69	156.97
Δ_3, [Deg]	-122.65	124.39	110.79	30.94	-38.63	-97.00	-147.00
P_2							
Γ_1, [Pa]	28201.56	37601.84	21670.39	27328.83	14477.63	9294.34	7079.37
Γ_2, [Pa]	200.09	338.63	159.39	246.86	95.70	53.63	37.50
Γ_3, [Pa]	553.81	841.08	74.16	150.70	62.13	19.85	19.83
Δ_1, [Deg]	-98.07	-126.88	-167.70	166.28	150.62	135.24	121.04
Δ_2, [Deg]	173.80	123.60	58.27	40.69	27.36	-4.99	-36.00
Δ_3, [Deg]	105.08	27.62	-140.36	132.88	110.99	44.46	-79.90

CFD simulations were performed for all the measured data using the models in Figures 30 and 33. The objective was to obtain the longitudinal permeability and coefficient of inertia under oscillatory flow conditions through a series of logical iterations process. In the iterative simulations the porous structure was assumed to be isotropic, due to the unavailability of radial parameters. The error caused by this assumption is likely to be small, however, because the simulation results indicate that radial flows were everywhere negligibly small in comparison with axial flows. The result of course is not surprising, given that the test section was specifically designed to ensure a predominantly axial flow. The approach for analyzing the experimental data was similar to what has already been described. A UDF was developed and used, and for each frequency Eqn. (5-1) with parameters representing P_1 was applied as the pressure inlet boundary condition of the corresponding CFD simulations. The predicted CFD results for pressure amplitude and phase at P_2 could then be directly compared with the experimental data or more conveniently with the predictions of Eqn. (5-1) with parameters representing P_2 for verification. Simulations were iteratively repeated by adjusting the axial hydrodynamic parameters β_x and C_x.

The following procedures were used to obtain the aforementioned hydrodynamic parameters. First, the case of 5 Hz which had the lowest experimental pressure drop across the regenerator was simulated by iteratively adjusting the viscous resistance coefficient β_x without including the inertial effect ($C_x = 0$) until P_2 simulation predictions matched the experimental data. Once the 5 Hz simulated results showed a good agreement between the experimental data and model predictions, the 30 Hz case

which had the largest experimental pressure drop was simulated. This time however, only the inertial coefficient C_x was iteratively adjusted while β_x was kept constant until good agreement was obtained between the P_2 predictions and experimental data. Then, using the determined values of β_x and C_x simulations were performed for all the measured frequencies. If good agreement was obtained for all frequencies then iterative simulations would end, otherwise β_x and C_x would be iteratively adjusted to match the experiment data. It should be mentioned, however, that at this point only minor adjustments were needed to match all the experiment data and simulation results to reasonable accuracy. It should however be emphasized unlike the approach followed by Nakayama [21], the methodology proposed here for determining β_x and C_x was not solely based on the limiting cases of very low flow rates (purely Darcy flow regime) and very high flow rates (inertial dominant flow regime). Rather, our investigation went beyond the work of Nakayama by validating the intermediate flow rate data points where both Darcy and Forchheimer inertial effects were comparable. These intermediate points were all accounted for in our empirical correlation results by operating the system in periodic mode and at various frequencies.

Figures 53 and 54 compare the experimental data with the simulation results representing the pressure at P_2 when inertial coefficient C_x, was set equal to zero. These results show that for 5 Hz a good agreement was obtained between the experiment data and model predictions; however for 30 Hz significant disagreement is observed. The latter disagreement is mainly due to neglecting Forchheimer inertial term in highly inertial dominant flow regime.

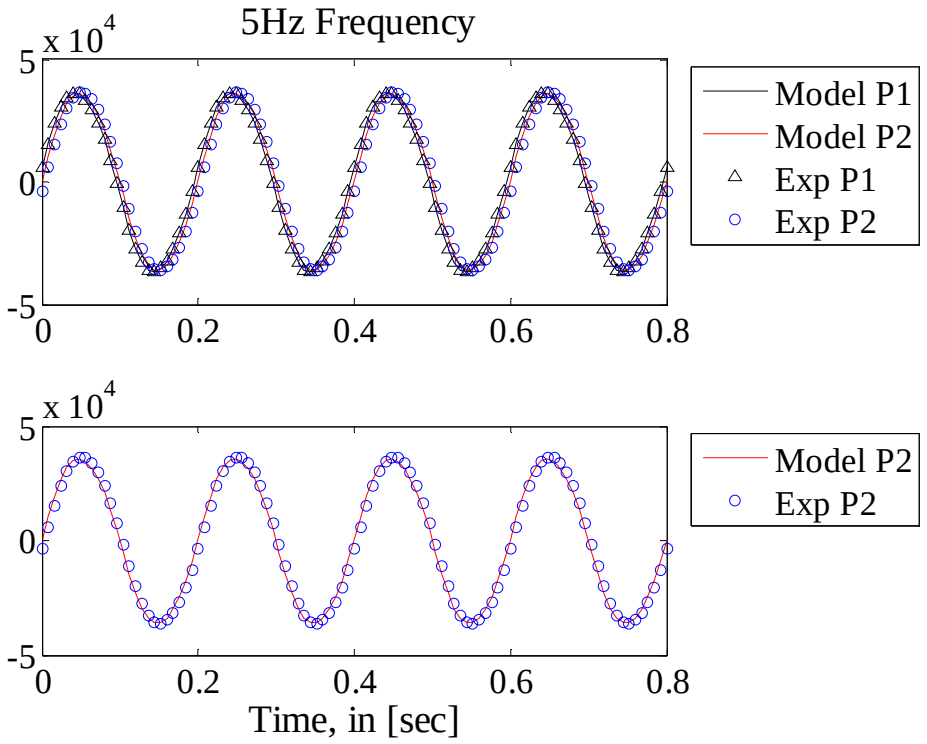

Figure 53. P_2 pressure simulation results for 325 mesh with $C_x = 0$.

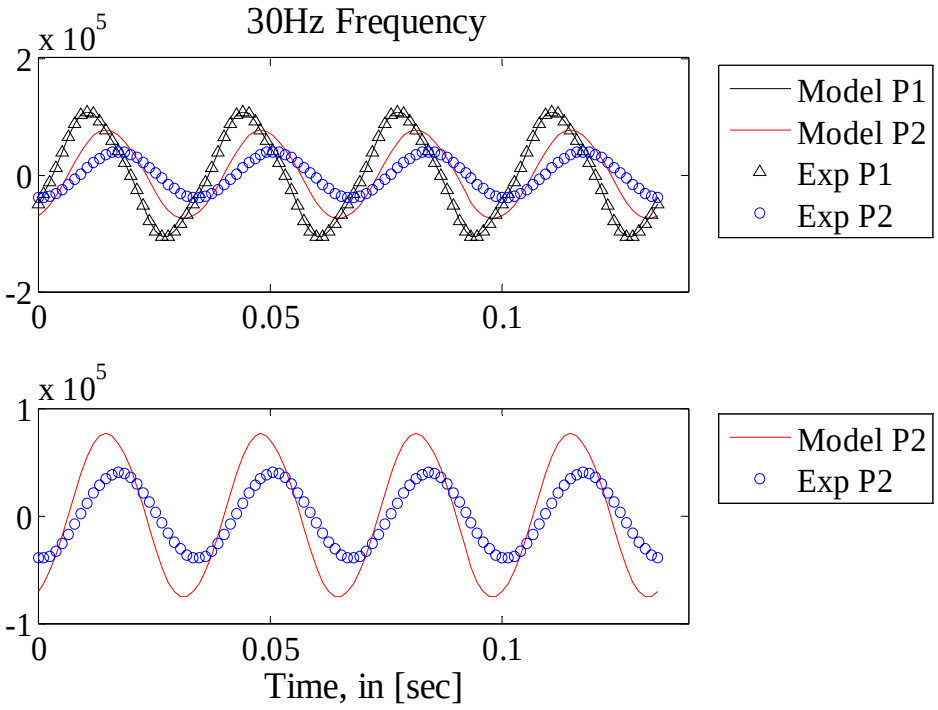

Figure 54. P_2 pressure simulation results for 325 mesh with $C_x = 0$.

This result agrees very well with our proposed methodology that at 5 Hz the flow regime is, to a good approximation, purely Darcy flow, and at 30 Hz the flow regime is almost purely inertial flow, and is dominated by inertial Forchheimer effect. Using the proposed methodology, simulations were performed for all the tested regenerators. Excellent agreement between data and simulation results were obtained using the β_x and C_x values summarized in Table 19.

Table 19. Results of oscillatory axial hydrodynamic parameters.

Regenerator Type	β_x [m^2]	C_x [m^{-1}]	K_x [m^2]	$c_{f,x}$ [-]	Porosity α , [%]	Charge pressure ,[MPa]
325 mesh screens	6.4247e-11	67000	3.077e-11	0.561	69.2	2.78
400 mesh screens	2.5295e-11	120000	1.211e-11	0.630	69.2	2.78
400 mesh sintered	1.9828e-11	110000	7.622e-12	0.637	62	2.78
Metallic foam	3.7689e-11	66000	1.160e-11	0.658	55.47	2.78
Micro-machined disks	4.0000e-11	192000	2.873e-12	8.453	26.8	2.78
400 mesh screens	3.3297e-11	70000	1.5853e-11	0.424	69.2	2.07

From Table 19, it can be seen that the permeability and inertial coefficient of the 400 mesh screens regenerator were different for different charge pressures. The correlation obtained using 2.78 MPa charge pressure data over predicted the friction factor values corresponding to the 2.07 MPa charge pressure. These two friction factors will be compared and discussed later in this chapter.

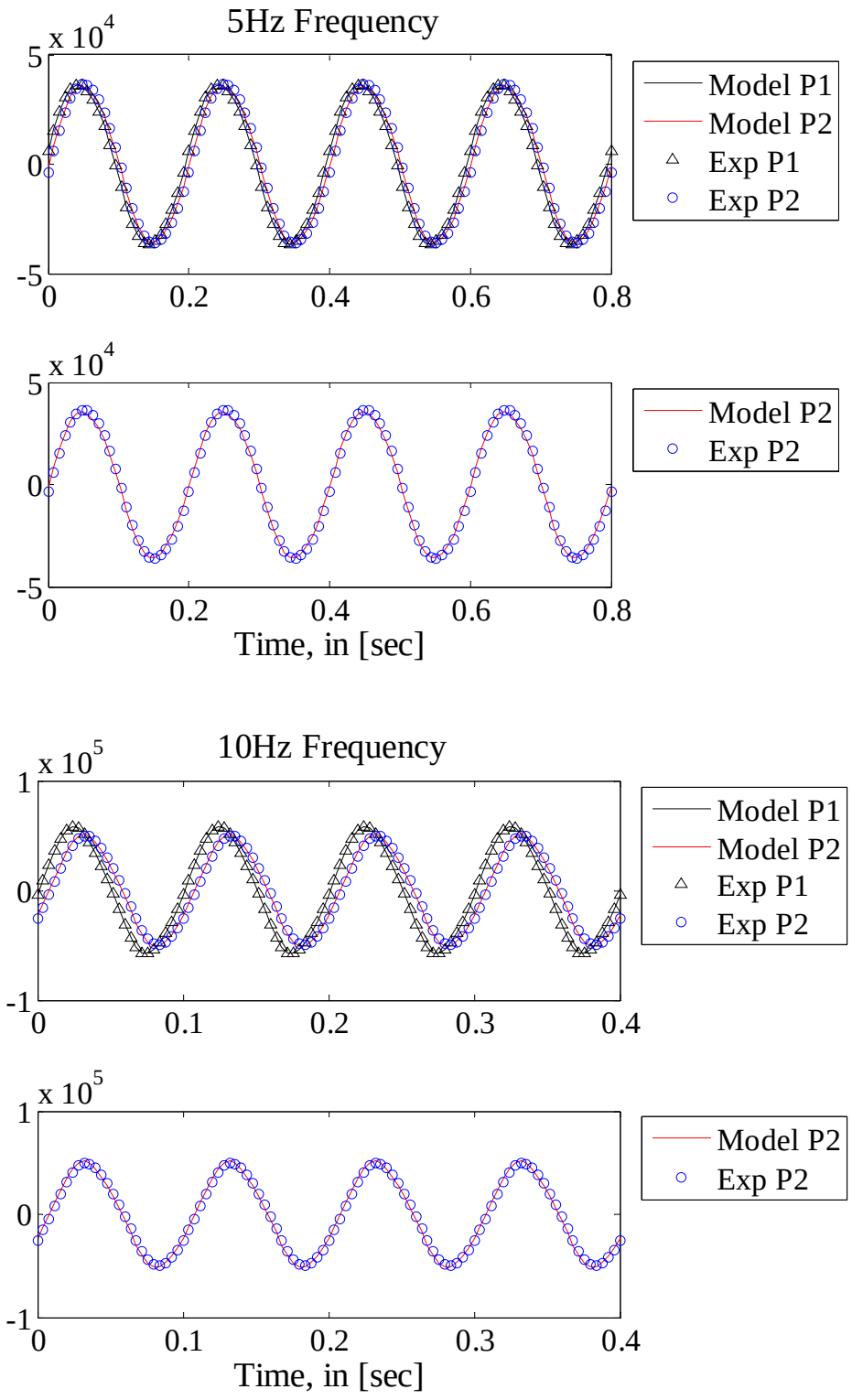

Figure 55. Prediction of pressure amplitude (P- P_{mean}), in [Pa] and phase at P_2, and their comparison to experimental data for SS 325 mesh.

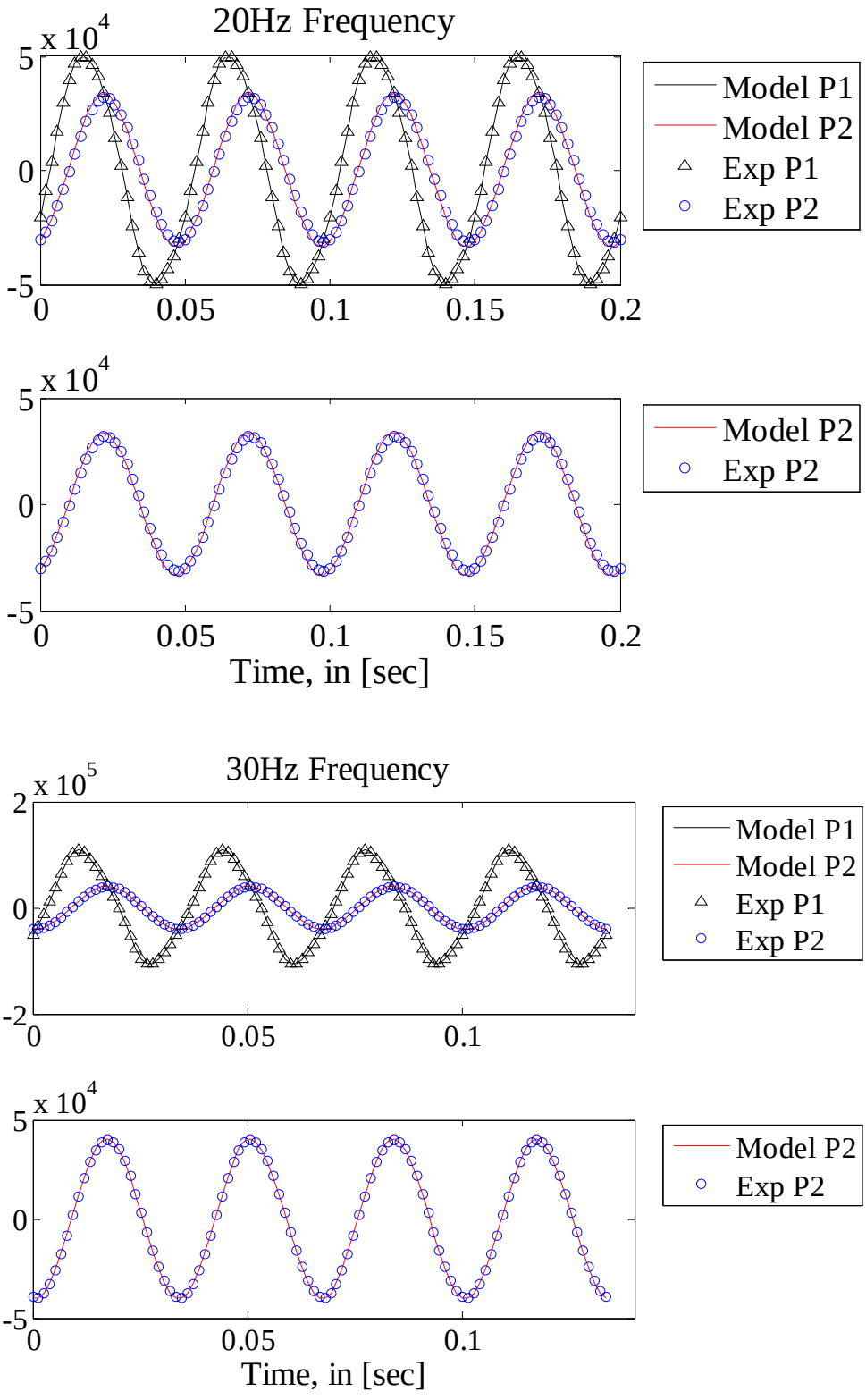

Figure 56. Prediction of pressure amplitude (P- P_{mean}), in [Pa] and phase at P_2, and their comparison to experimental data for SS 325 mesh.

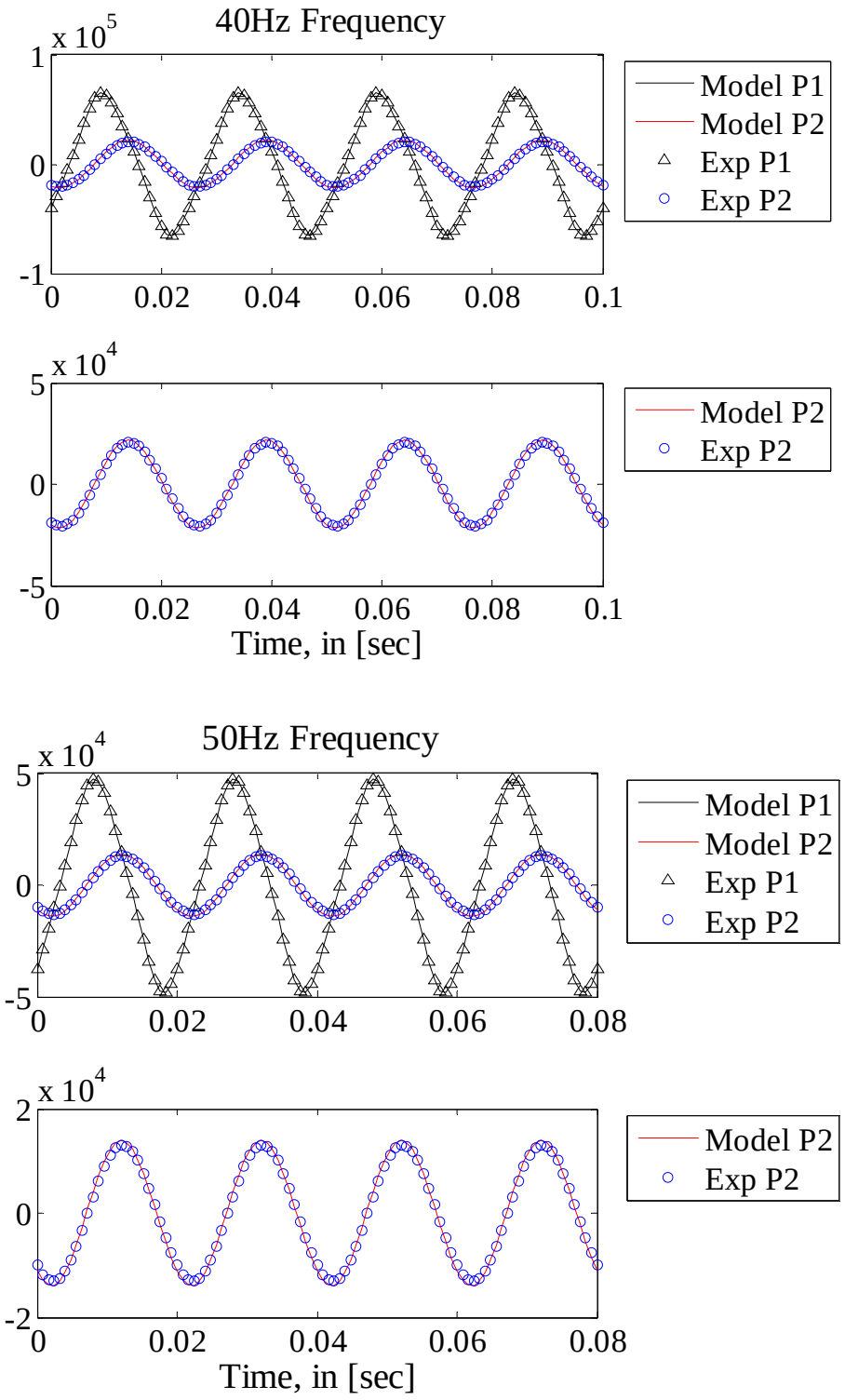

Figure 57. Prediction of pressure amplitude (P- P_{mean}), in [Pa] and phase at P_2, and their comparison to experimental data for SS 325 mesh.

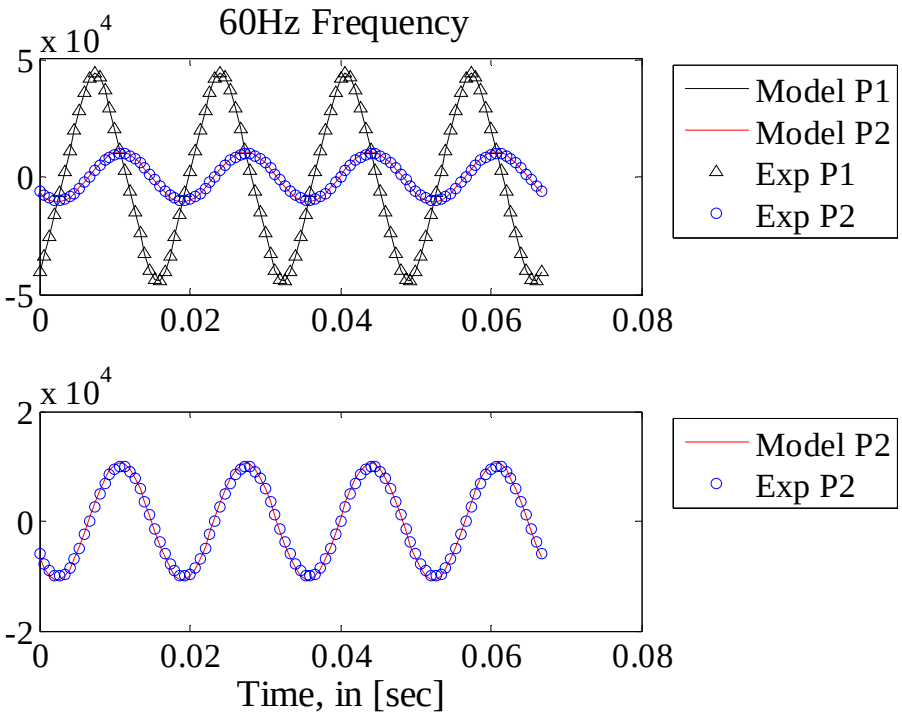

Figure 58. Prediction of pressure amplitude (P- P_{mean}), in [Pa] and phase at P_2, and their comparison to experimental data for SS 325 mesh.

The simulated results for the 325 mesh screen regenerator are depicted in Figures 55 through 58. These figures display the measured and predicted pressure amplitudes (P- P_{mean}), and the phase angle at location P_2 for different operating frequencies. All the predictions shown in the above-mentioned figures were obtained using the values viscous resistance coefficient β_x, and the inertial resistance coefficient C_x, for the 325 mesh screen summarized in Table 19. Excellent agreements between experimental data and model predictions of P_2 pressure amplitudes and phase angles were obtained for all the tested frequencies.

Figure 59 displays the predicted pressure distribution in the 325-mesh regenerator at a snapshot. The pressure gradient in the regenerator at the depicted snapshot indicates that fluid is flowing from left to right at this instant time of the cycle period. Figure 60

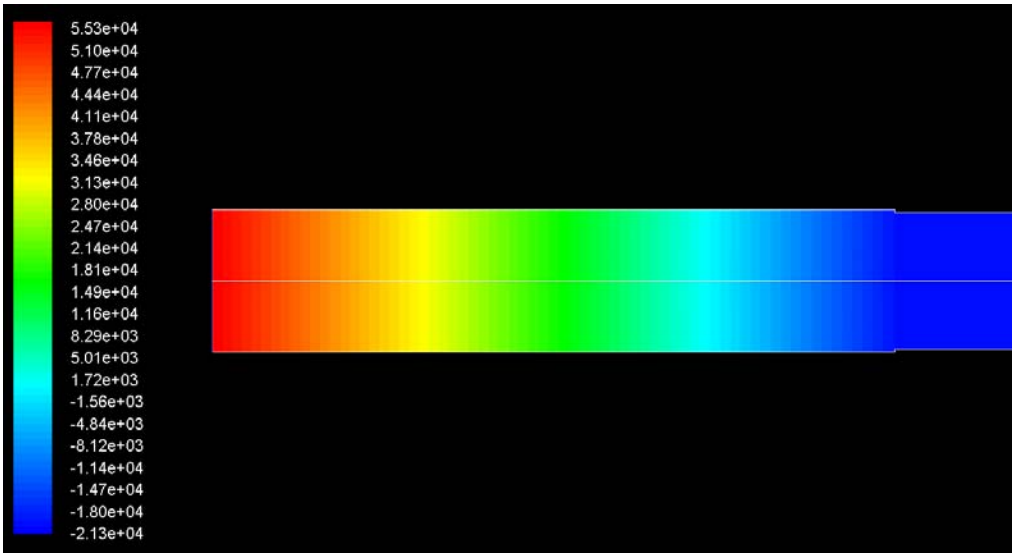

Figure 59. Instantaneous snap shot of static pressure in *325- mesh regenerator, in* [Pa].

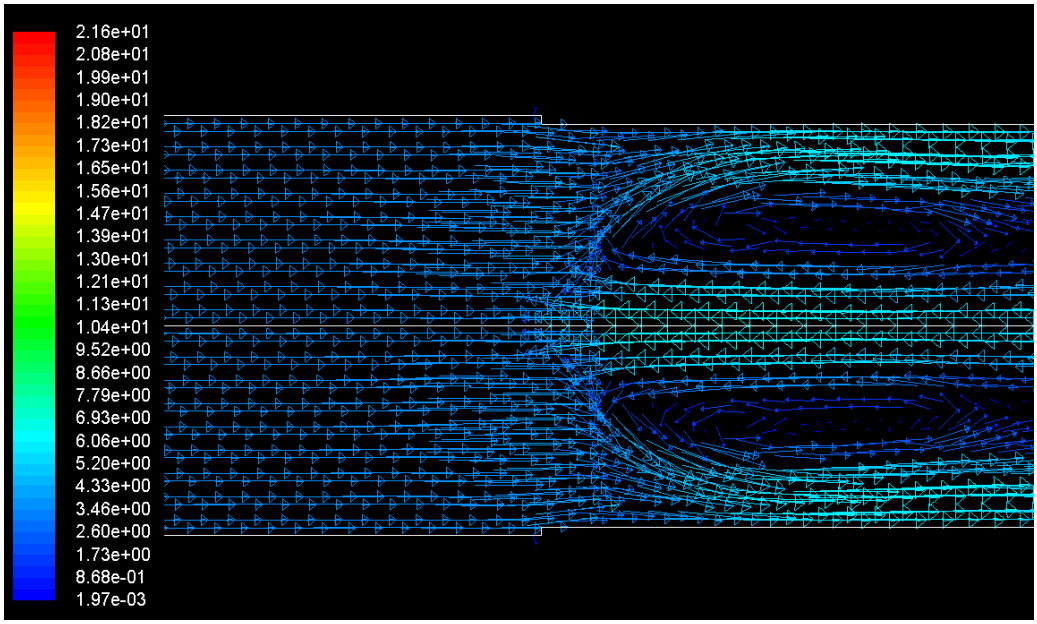

Figure 60. Instantaneous snap shot of velocity vectors at the exit of the *325- mesh regenerator, in* [m/s].

which illustrates the predicted local velocity vectors in the regenerator at the same snapshot, further confirms the flow direction in the regenerator. Careful review of the

simulation results indicates that, overall, the flow field in the entire regenerator is predominantly 1-D, as expected. Significant multi-D flow effects occurred at location where flow disturbance was present, however. A good example is the fluid space next to the regenerator, which showed significant flow multi-dimensionalities.

The above methodology for the analysis and correlation of the experimental data were pursued for other regenerator fillers as well. Similar to the 325 mesh results, the simulation results for all the other regenerator fillers showed excellent agreement with data. Only a few plots representing the metallic foam and the 400 mesh sintered regenerator matrices will be shown here (see Figures 61 and 62) in this section for brevity. The readers can refer to Appendix B for the detailed simulation results for other tested regenerators.

Figures 61 and 62 compares the measured and simulation results for sintered 400 and metallic foam metal regenerators for 5 Hz and 30 Hz frequencies, respectively.

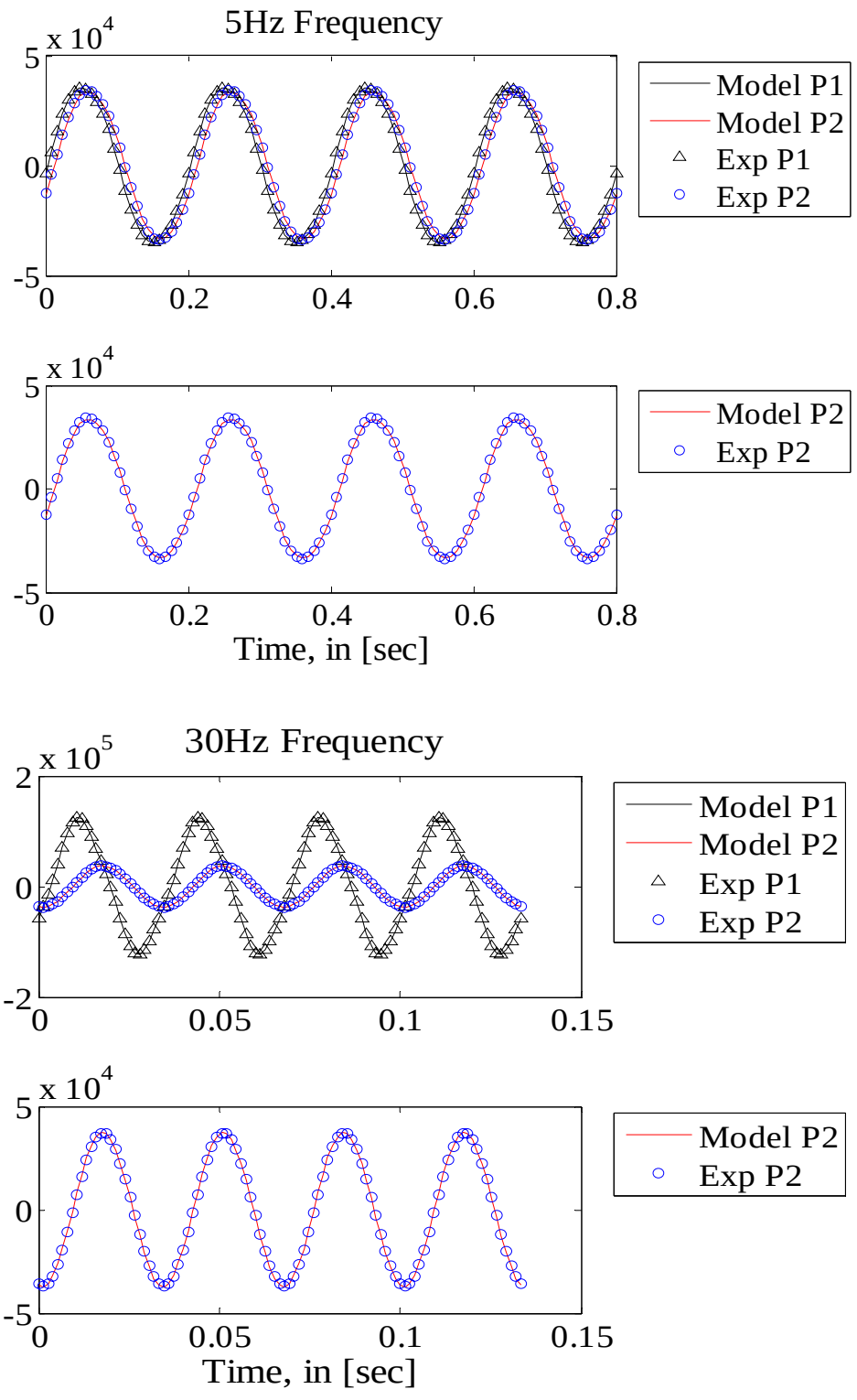

Figure 61. Prediction of pressure amplitude (P- P_{mean}), in [Pa] and Phase at P_2, and their comparison to experimental data for metallic foam

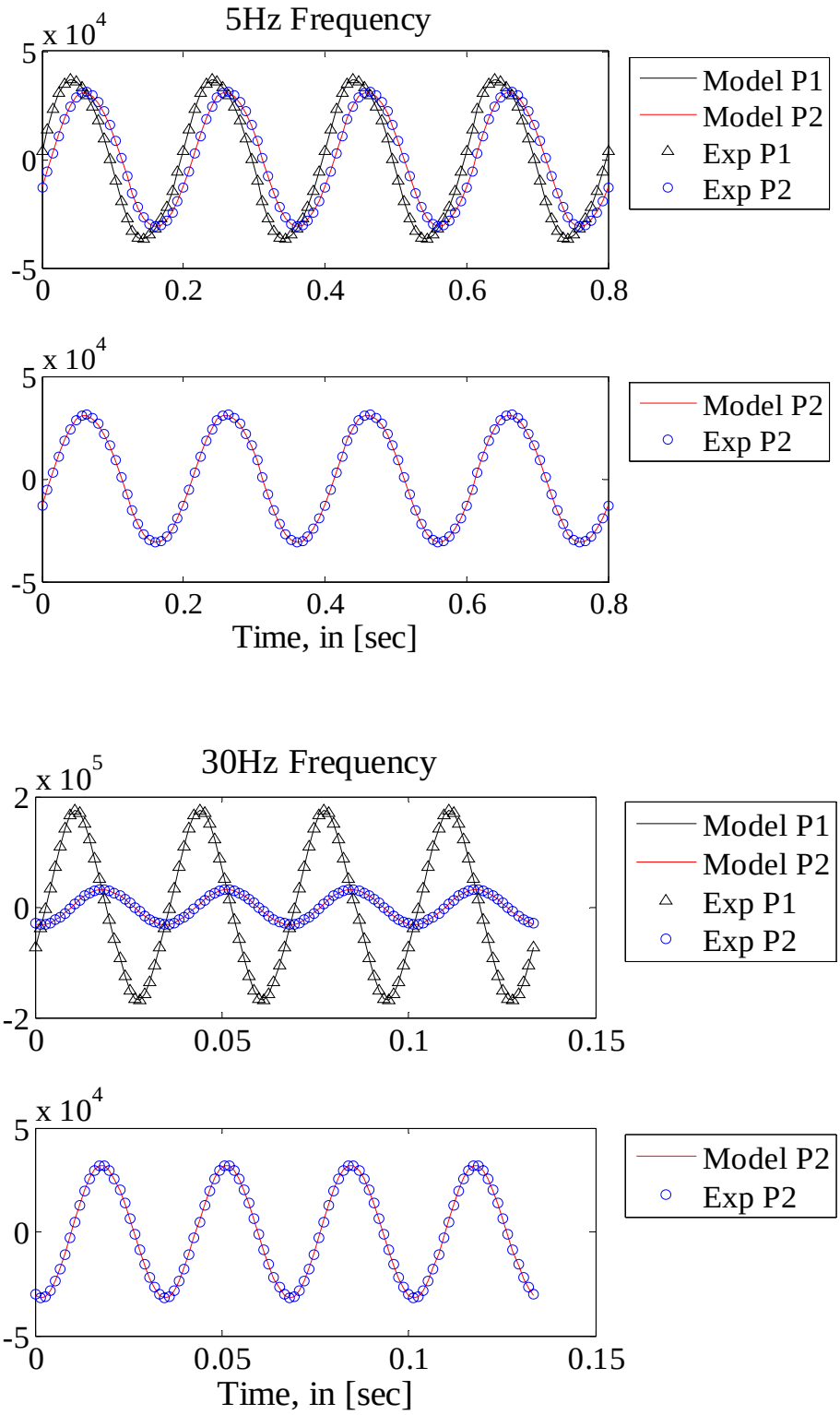

Figure 62. Prediction of pressure amplitude (P- P_{mean}), in [Pa] and Phase at P_2, and their comparison to experimental data for metallic foam (A) and SS 400 mesh sintered (B).

5.4 Axial Pressure Drop Test Results for Steady Flow

In a separate investigation, Clearman [41] performed experiments using the test apparatus depicted in Figure 19, and measured the axial pressure drops for all the afore-mentioned regenerator filler materials. He also analyzed and correlated his experimental results following a CFD-assisted methodology similar to the methodology used in this study. The details of Clearman's data can be found in [41]. Table 20 is a summary of the results of his data analysis. The table thus displays the steady, axial viscous resistance coefficient β_x and inertial resistance coefficient C_x, for all the regenerator filler materials of interest to this investigation.

Table 20. Results of steady flow axial hydrodynamic parameters.

Regenerator Type	β_x [m^2]*	C_x [m^{-1}]*	K_x [m^2]*	$c_{f,x}$ [-]*	K_x [m^2]*	$c_{f,x}$ [-]*
325 mesh Screens	4.2553e-11	47000	2.067e-11	0.316	3.53e-11	0.376
400 mesh Screens	3.6101e-11	73000	1.753e-11	0.452	2.69e-11	0.407
400 mesh Sintered	1.8018e-11	260000	6.848e-12	1.452	N/A	N/A
Metallic foam metal	3.7736e-11	99000	1.1611e-11	0.988	2.8e-11*	0.445*
Micro-machined disks	4.3478e-11	115000	3.123e-12	5.279	N/A	N/A

* based on 61% porosity, * based on experimental data of Harvey [1].
* based on experimental data of Clearman [41].

5.5 Comparison of Steady and Oscillatory Directional Hydrodynamic Parameters

An alternative to the definition of viscous resistance and inertial resistance coefficients is the friction factor defined in Eqn. (5-2).

$$0.5\frac{f_j}{\sqrt{\beta_j}}\rho|\vec{u}|u_j = \frac{\mu}{\beta_j}u_j + \frac{C_j\rho}{2}|\vec{u}|u_j \tag{5-2}$$

where $j = x$ and r. Thus, for axial and radial directional friction factors we have:

$$0.5\frac{f_x}{\sqrt{\beta_x}}\rho|\vec{u}|u_x = \frac{\mu}{\beta_x}u_x + \frac{C_x\rho}{2}|\vec{u}|u_x \tag{5-3}$$

$$0.5\frac{f_r}{\sqrt{\beta_r}}\rho|\vec{u}|u_r = \frac{\mu}{\beta_r}u_r + \frac{C_r\rho}{2}|\vec{u}|u_r \tag{5-4}$$

By non-dimensionalizing Eqn. (5-2) the friction factor can be recast as:

$$f_j = \frac{2}{\mathrm{Re}_{\beta_j}} + C_j\sqrt{\beta_j} \tag{5-5}$$

where Re_{β_j} is the local Reynolds number defined as

$$\mathrm{Re}_{\beta_j} = \frac{\rho|\vec{u}|\sqrt{\beta_j}}{\mu} \tag{5-6}$$

Figure 63 represents plots of friction factor versus local Reynolds number for the tested regenerator samples for the steady and oscillatory flow tests. As noted,

for $\mathrm{Re}_{\beta_x} \leq 1.0$, for both oscillatory and steady flow conditions, the friction factors of all filler materials are essentially the same. Deviation among the friction factors of different fillers occur at $\mathrm{Re}_{\beta_x} \geq 1.0$.

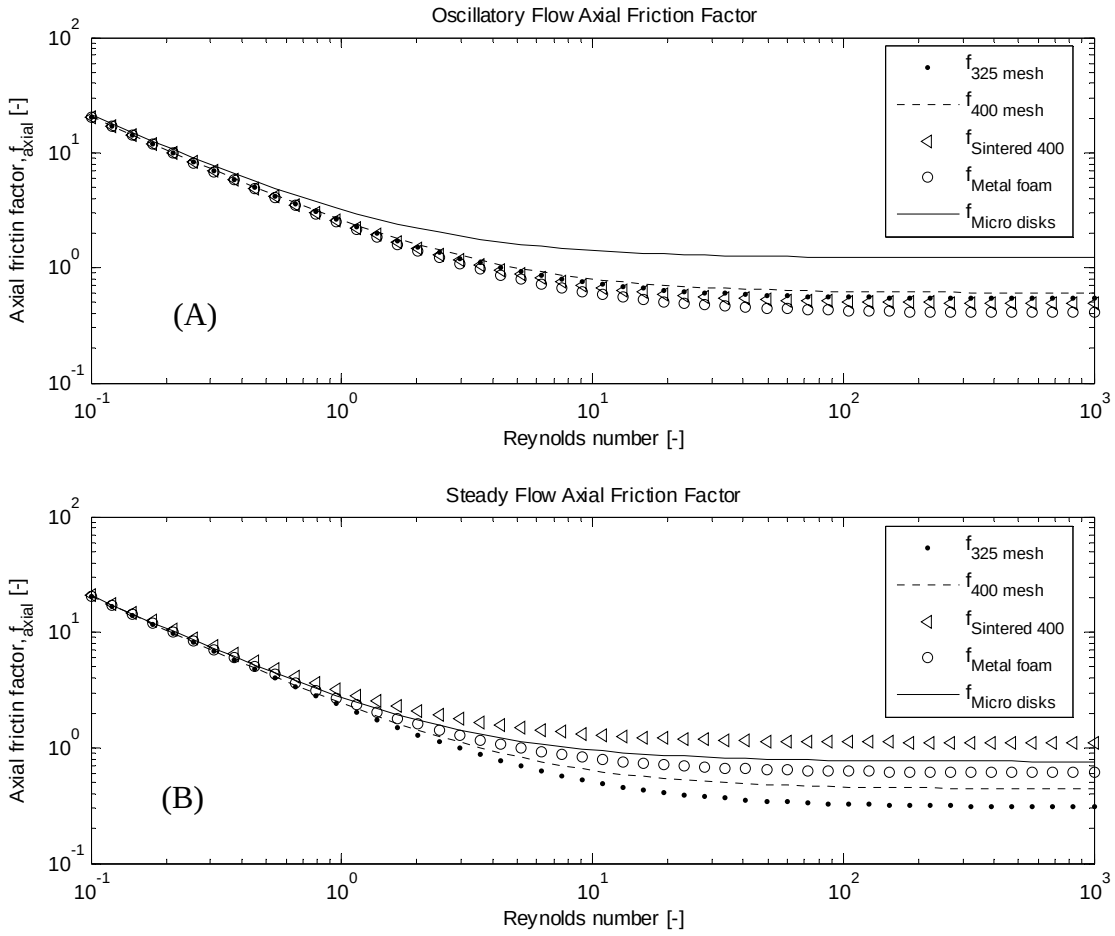

Figure 63. Oscillatory (A) and steady (B) friction factors.

The asymptotical behavior of Eqn. (5-6) is clearly observed in both parts of Figure 63, showing that in the limiting case of high Reynolds number the friction factor approached the value of $C_j\sqrt{\beta_j}$. For the oscillatory flow conditions, the micro machined disks showed the highest values of friction factor.

An important point must be made about Figure 63. The friction factor results shown in Fig. 63 evidently cover a Reynolds number range from 10e-4 to 10e6. However, the highest Reynolds numbers in the experiments were about 29. The portions of Fig. 63 where Reynolds number is greater than about 29 are thus mere extrapolations. The experimental maximum Reynolds number of approximately 28 is on the low side of typical cryocooler operating range. Experiments at higher Reynolds numbers were not possible in this investigation because of the relatively small swept volume of the compressor, and the limitations on the current in the drive electronics. A larger pressure wave generator will be needed to generate data representing high Reynolds numbers.

In the steady friction factor plot, sintered 400 mesh showed the highest friction factor results among the tested regenerators.

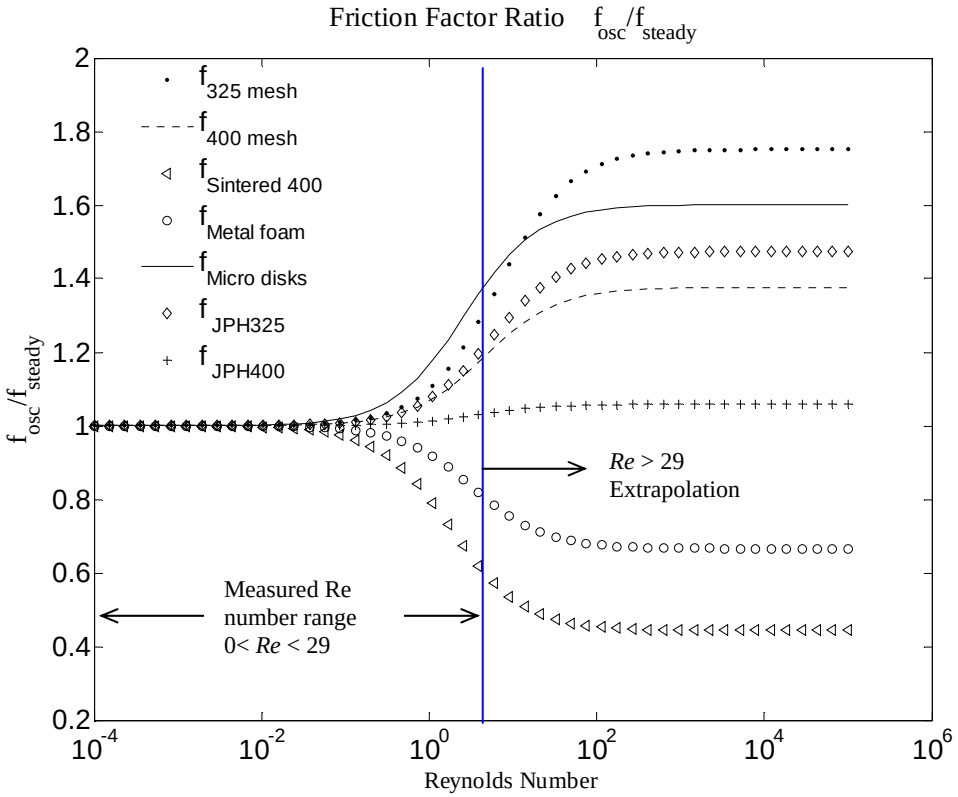

Figure 64. Oscillatory axial to steady axial friction factor ratio for various regenerator fillers.

Figure 64 displays the ratio between the friction factors representing oscillatory and steady flows (f_{osc} / f_{steady}) for all the tested regenerator samples. This ratio evidently quantifies the deviation of oscillatory flow friction value from the steady flow friction value. This is an important issue because, as mentioned earlier in Section 2.2, it is common practice to use steady-flow friction factors in the simulation of oscillatory flows. For the Reynolds numbers up to almost 0.1 the ratio is essentially one, and no significant deviations were observed. In other words, the steady friction factor values were virtually identical to the oscillatory friction factor. However, for Reynolds numbers greater than 0.1 significant deviations can be noted. This result agrees well with some reported observations in the open literatures [24-26]. All the meshed screens and perforated disk type regenerators showed higher oscillatory friction factors. However, for the foam metal and sintered 400 mesh fillers the oscillatory friction factors were smaller in comparison with steady friction factors.

The oscillatory friction factor for 325 and 400 mesh regenerator samples were also compared with the steady flow friction factor results of Harvey [1]. The results of this comparison are shown in Figure 65, where $f_{steady,JPH}$ represents the data of Harvey [1]. As noted, consistent with the results of this investigation, for both cases higher friction factor values occur for oscillatory flow. Among the tested regenerators the 325 mesh regenerator had the most deviations between steady and oscillatory friction factors

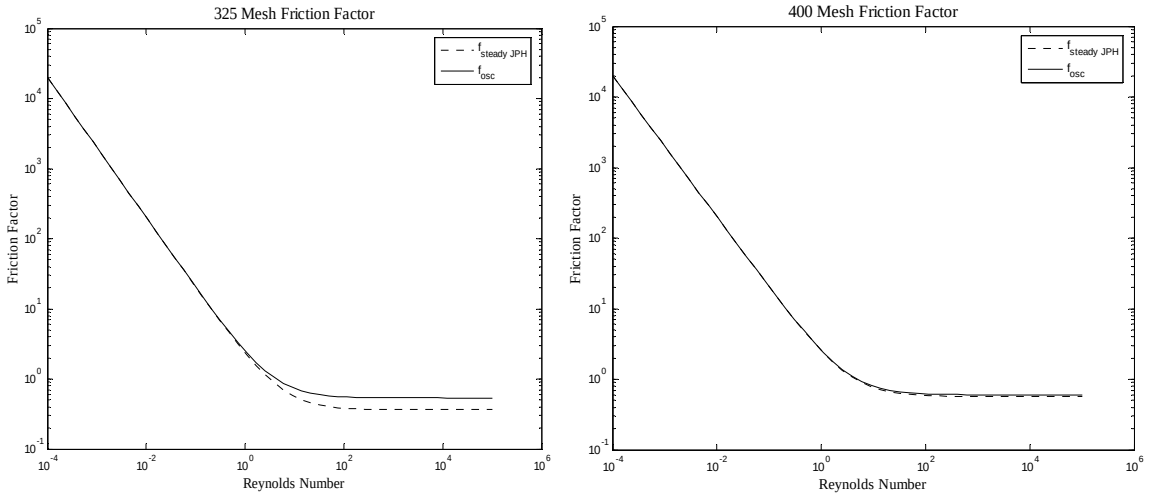

Figure 65. Comparison of axial oscillatory and steady friction factor.

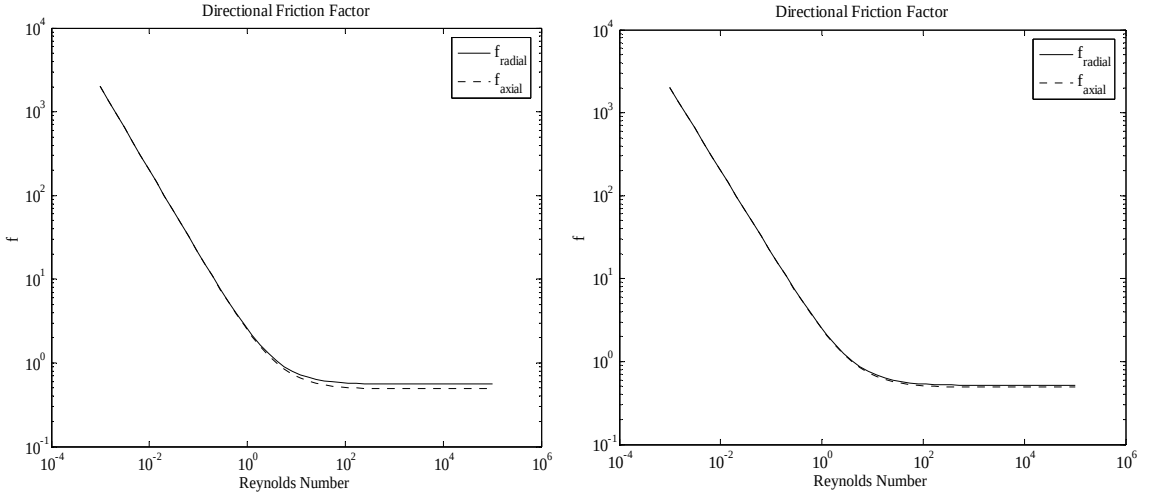

(A) (B)

Figure 66. Oscillatory directional friction factors for sintered 400 mesh. (A) charge pressures are 3.2 MPa for radial and 2.78 MPa for axial (B) charge pressures are 2.78 MPa for both radial and axial.

Two directional oscillatory friction factors are depicted in Figure 66. Both cases represent sintered 400 mesh regenerator filler. Figure 66 (A) compares the radial and axial friction factors. For this comparison radial and axial friction factors were correlated using different charge pressures, 3.2 MPa charge pressure for radial and 2.78 MPa for axial.

Figure 66 (B) shows the same comparison; however, for this comparison both radial and axial friction factors were correlated using 2.78 MPa charge pressure. As noted because of the relatively small difference between the two charge pressures, the friction factors at the two charging pressures are approximately identical. Furthermore, Figure 66 (B) shows that for the sintered 400 mesh filler, when the effect of charging pressure is eliminated, the radial and axial friction factors are essentially the same.

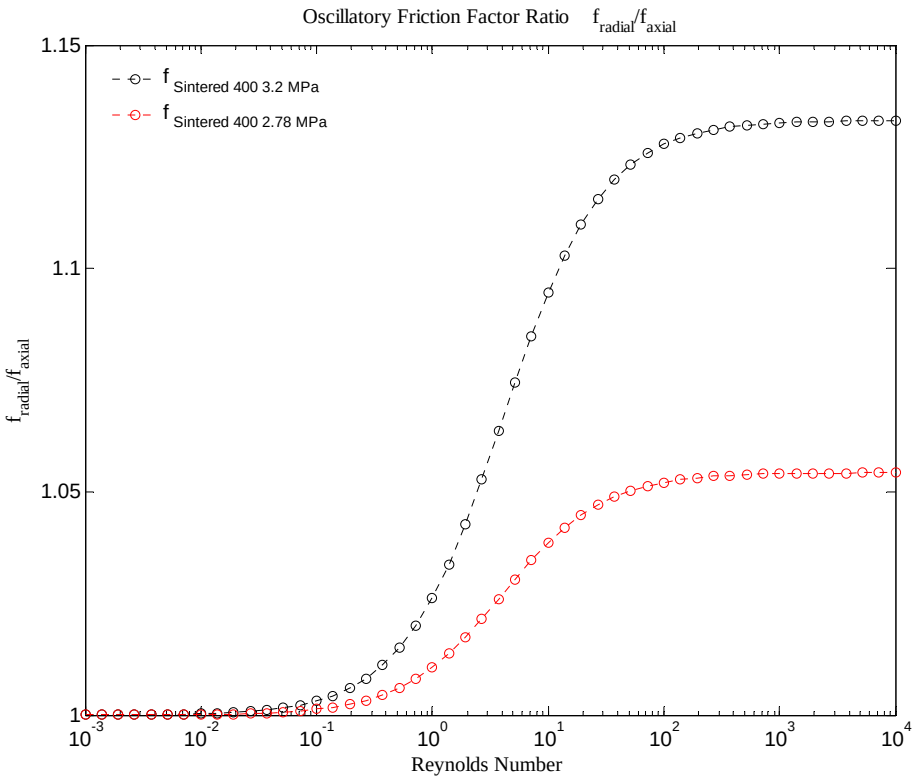

Figure 67. Oscillatory flow directional friction factor ratio for sintered 400 mesh.

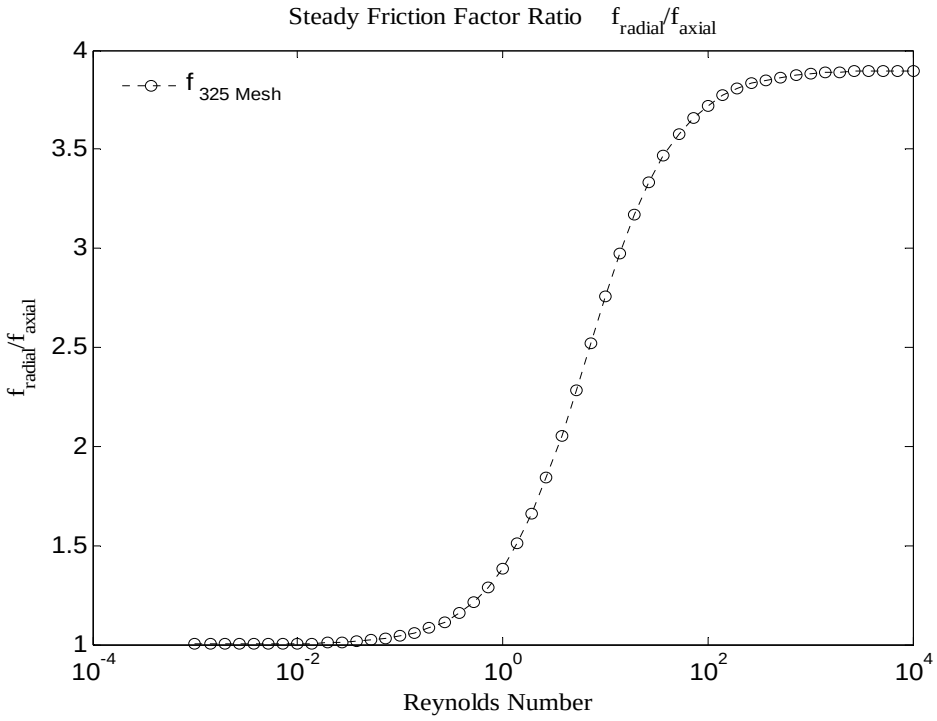

Figure 68. Steady directional friction factor ratios for 325 mesh.

Figure 67 displays the oscillatory directional friction factor ratio (f_{radial} / f_{axial}) for sintered 400 mesh sample. The radial friction factor is consistently higher than the axial friction factor. Furthermore, with higher charge pressure the difference between the two directional friction factors is larger. The results obtained with 325 mesh regenerator sample also showed similar trends (see Figure 68). Figure 69 displays the effect of the charging pressure on the axial friction factor for oscillatory flow in the sintered 400 mesh filler. The figure shows the variation of the ratio between the axial friction factors representing 2.78 MPa and 2.07 MPa charge pressures. The trends in this figure are consistent with the radial friction factor results. They show that a higher charge pressure leads to a higher friction factor.

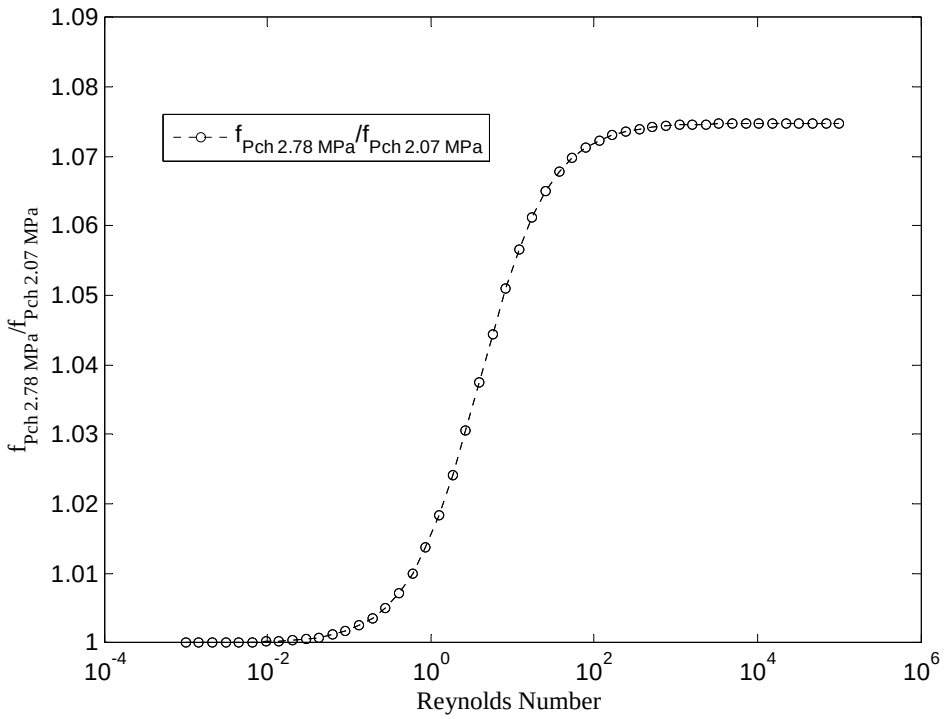

Figure 69. Oscillatory axial friction factor ratio for sintered 400 mesh using different charge pressures.

5.6 Model Validation Using Hot Wire Anemometry under Oscillatory Flow

The previous sections of this chapter dealt with a series of CFD simulations that were performed to obtain local anisotropic hydrodynamic friction parameters, based on experimentally measured pressure data. As mentioned earlier, the proposed methodology applied for the analysis and interpretation of the experimental data is based on a series of rational steps. Accordingly, local instantaneous pressures were experimentally measured at the inlet and exit of test sections that contained a porous regenerator filler. The measured inlet time dependent pressures were subsequently imposed directly to a CFD model of the test section as an inlet boundary condition. Then, the viscous resistance

coefficient β_x and the inertial resistance coefficient C_x were iteratively adjusted in the CFD code to match the experimental and CFD-predicted pressure amplitudes and phase angles at P_2, the exit of the porous structure in the test section. The hydrodynamic parameters obtained in this way could then be empirically correlated. The results presented and discussed thus far show that this procedure performs very well, and when the correlations representing the afore-mentioned hydrodynamic parameters are incorporated in the CFD code, the code predictions everywhere agree with all measurements very well. However, model validations were only based on experimentally measured exit pressure measurements, since pressure was the only parameter that was measured.

To further confirm the feasibility of this proposed methodology, it was decided that additional experimental validation using local flow properties such as mass flow or velocity is needed. Therefore, a hot wire anemometry (HWA) system was incorporated in the experimental apparatus and the anemometer probe was mounted at the inlet location of the regenerator. With this arrangement the local instantaneous velocities were measured, using TSI's Flow Point Velocity Transducer (Model 1500). The HWA that was used in this investigation is a two channel Constant Temperature Anemometer and required a steady flow velocity calibration. The procedures for calibrating the HWA are documented in Appendix D, where the plot voltage-to-velocity calibration curve is also shown.

The HWA probe was carefully mounted onto the experimental apparatus and into the flow stream at the inlet of the test section used for axial oscillatory flow measurements (Figure 70) and aligned at the center of the flow area. The local axial

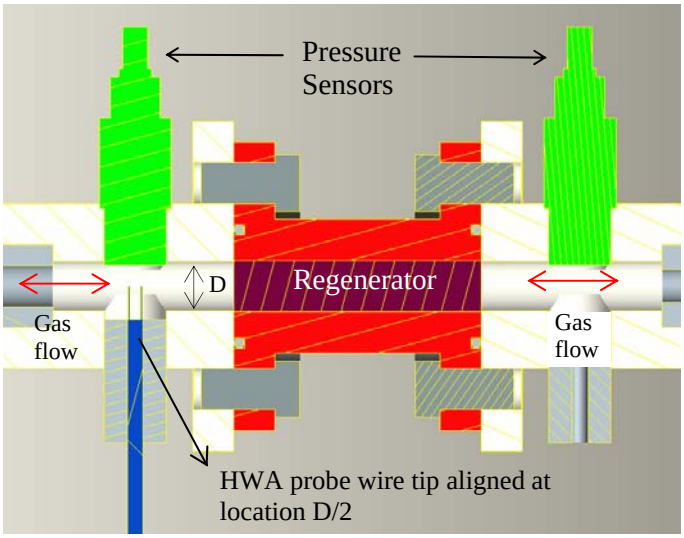

Figure 70: Detail view of hot wire probe location

point velocity was then measured with respect to time once steady periodic mode was obtained. Two regenerator samples, metallic foam metal and sintered 400 mesh, were chosen for the HWA measurement. For convenience, the measured velocity results are represented below in terms of mass fluxes which were calculated based on the local density. The measured mass fluxes compared with the mass flow rate predictions of the CFD model simulations in Figure 71 and 72. The model simulations results depicted in Figs. 71 and 72 were obtained using the viscous resistance coefficient β_x and inertial resistance coefficient C_x values for the metallic foam metal and sintered 400 mesh regenerator fillers, as summarized in Table 19.

The comparison between the simulation-predicted and measured local and instantaneous mass fluxes is depicted in Figure 71 for the metallic foam metal regenerator filler. A similar comparison for the sintered 400 mesh is shown in Figure 72.

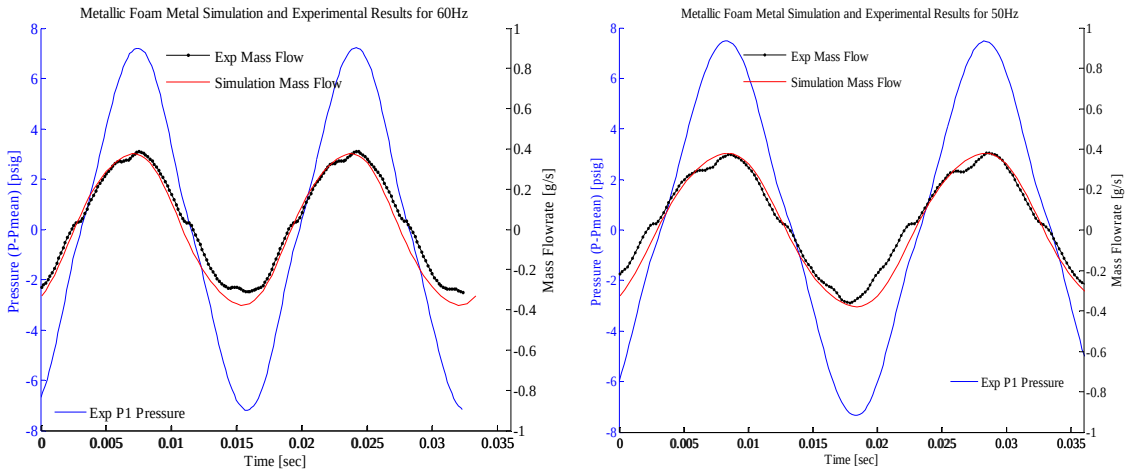

(A) (B)

Figure 71. Comparison of predicted regenerator inlet mass flow and experimentally measured regenerator inlet mass flow for metallic foam metal for 60 Hz (A) and 50 Hz (B).

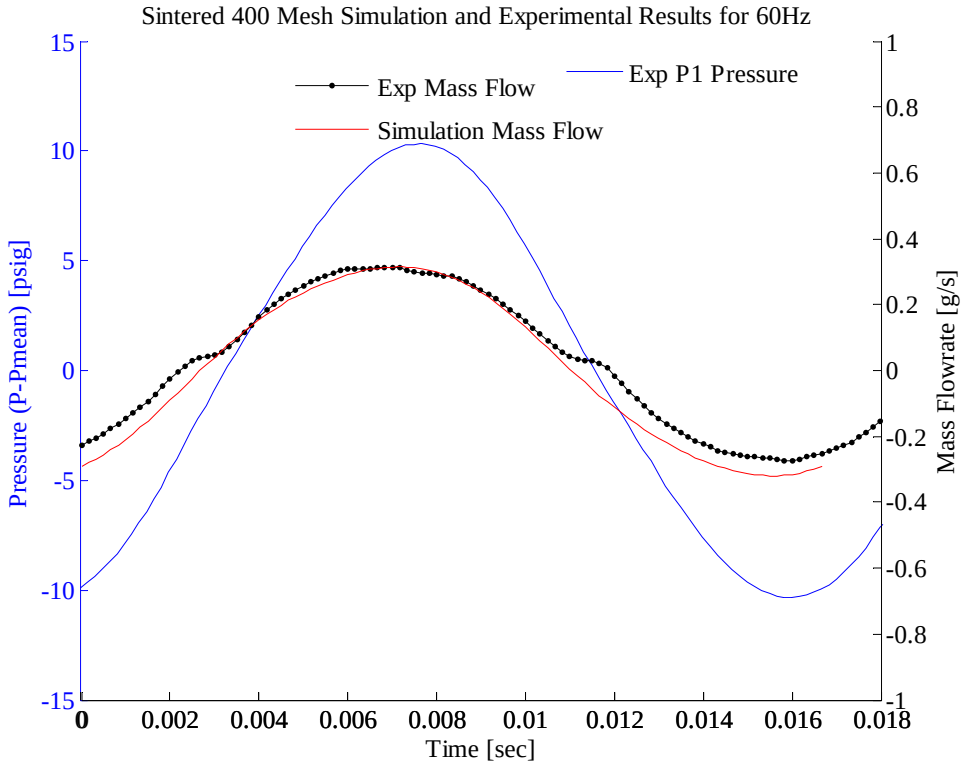

Figure 72. Comparison of predicted regenerator inlet mass flow and experimentally measured regenerator inlet mass flow for sintered 400 mesh for 60 Hz frequency.

These figures show excellent agreement between the measured data and predictions of the simulations. The simulation results also showed that mass flux was leading the pressure wave at the inlet to the regenerator. This agrees well with experimental data observations and intuition.

5.7 Parametric Study for ITPTC

As mentioned before in Section 2.2.2, reliable hydrodynamic and heat transfer closure relations are not scarce for periodic flow in porous structures, and closure relations representing steady flow are sometimes used in models dealing with periodic flow. The application of steady-flow parameters to periodic flow would evidently introduce a change in the performance results of a model. The objective of the parametric and sensitivity study that is discussed in this section was to obtain a quantitative estimate of the effect of uncertainties associated with the application of steady-flow hydrodynamic parameters on the results of CFD simulations dealing with periodic flow. Ten system level simulations were performed using an entire ITPTC model. The first five were simulated using oscillatory flow regenerator closure relations which were discussed in the previous section. The remaining five simulations were performed using steady flow closure relations. Figure 38 and Table 8 provide the physical dimensions and the characteristics of the simulated ITPTC system. The operating frequency of 40 Hz was used for all simulations for consistency. An initial temperature of 300 K was applied everywhere in the ITPTC system for all the simulations and transient simulations were

carried out using time increment of 0.0005 seconds. The convergence criterion of 1.0e-5 for the mass, *x*-velocity, *r*-velocity, and of 1.0e-7 for the energy were used for all simulations. The expectation is that the transient simulations will continue until steady periodic state is reached. However, certain important conclusions can be made by examining the transient time histories of various parameters even though steady periodic flow state has not been reached.

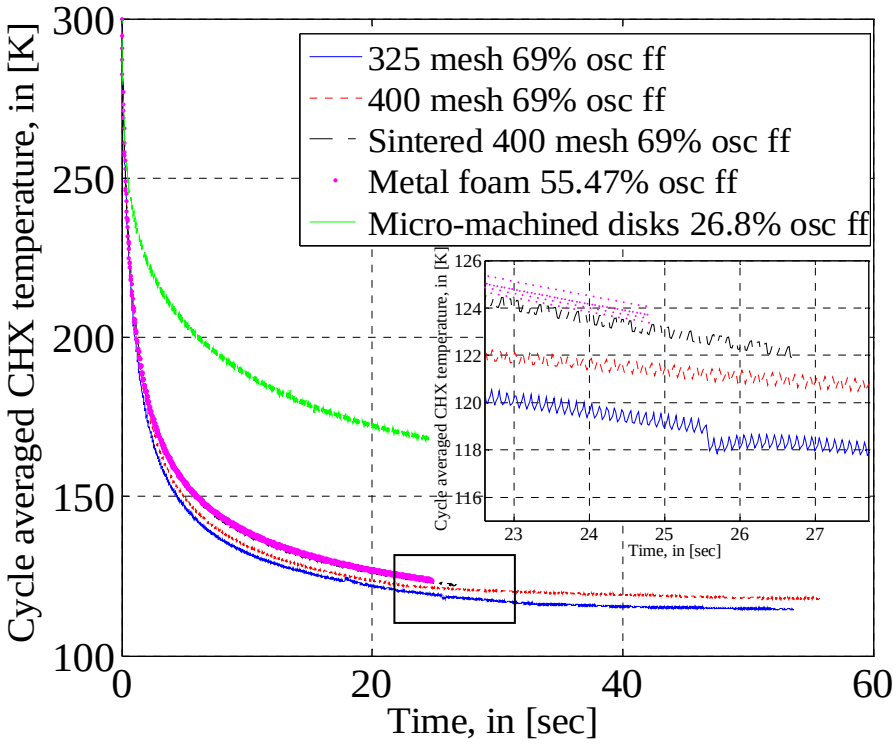

Figure 73. Cycle averaged CHX temperatures of ITPTC simulations using oscillatory closure relations.

The cycle average cold-heat exchanger (CHX) temperature results for the simulation using oscillatory closure relations are plotted in figure 73. As expected, gradual cooling was observed at the CHX component of the ITPTC system for all simulated model. After 60 seconds of simulation time, the 325 mesh regenerator model achieved the lowest cold tip temperature of about 114 ^{o}K, followed by 400 mesh, sintered

400 mesh, metallic foam metal, and the nickel perforated disks. The cooling rate as well as the difference among the quasi-steady cold tip temperatures, are evidently functions of the regenerator filler type. This is a further confirmation of the importance of the closure relations applied to the regenerator. The 325 mesh performed the best by reaching the lowest temperature among the simulated models and having the fastest cooling rate. The perforated disk, however, had the lowest temperature performance among the simulated models. Based on these results, and the simulation results dealing with friction factors in oscillating flow, the tested fillers can be ranked for their system-level performance. Table 21 displays the ranking of the fillers.

Table 21. Ranking of system level performance based on transient simulated time and oscillatory friction factor.

Simulated ITPTC Models	System level performance rank	Oscillatory friction factor rank
325 mesh	1 (114 ^{o}K @ 58 sec)	3 (f = 0.608 @ ~Re 29)
400 mesh	2 (118 ^{o}K @ 60 sec)	4 (f = 0.675 @ ~Re 29)
400 mesh sintered	3 (120 ^{o}K @ 33 sec)	2 (f = 0.561 @ ~Re 29)
Metallic foam metal	4 (121 ^{o}K @ 30 sec)	1 (f = 0.476 @ ~Re 29)
Micro-machined disks	5 (165 ^{o}K @ 30 sec)	5 (f = 1.285 @ ~Re 29)
	(1) Lowest Temperature Achieved (5) Highest Temperature Achieved	(1) Lowest Friction Factor (5) Highest Friction Factor

Clearly, performance rank does not correspond to the rank according to the friction factor results. The regenerator sample that had the second lowest friction factor had the third best performance with respect to cooling, and the regenerator that had the third lowest friction factor had the best system level performance. The micro machined disks had the worse performance with respect to cooling while having the highest friction factor as well. The uncertainties associated with using different closure relations apparently have a significant impact on the systems overall performance.

In order to better understand the performance of simulated models, simulations were performed and compared with a well defined baseline ITPTC model simulation. The baseline model used here is a replica version of MOD1 model in [44-46]. The baseline simulation thus considers an ITPTC that in terms of all physical characteristics is identical to the ITPTC system that was the subject of discussion so far, except for the regenerator length and filler matrix. Also the baseline ITPTC operates at 34 Hz instead of 40 Hz. Results of all the simulations are plotted in Figure 74. Although with exception of the baseline model the simulations have not reached quasi steady-periodic conditions, their trends are clear.

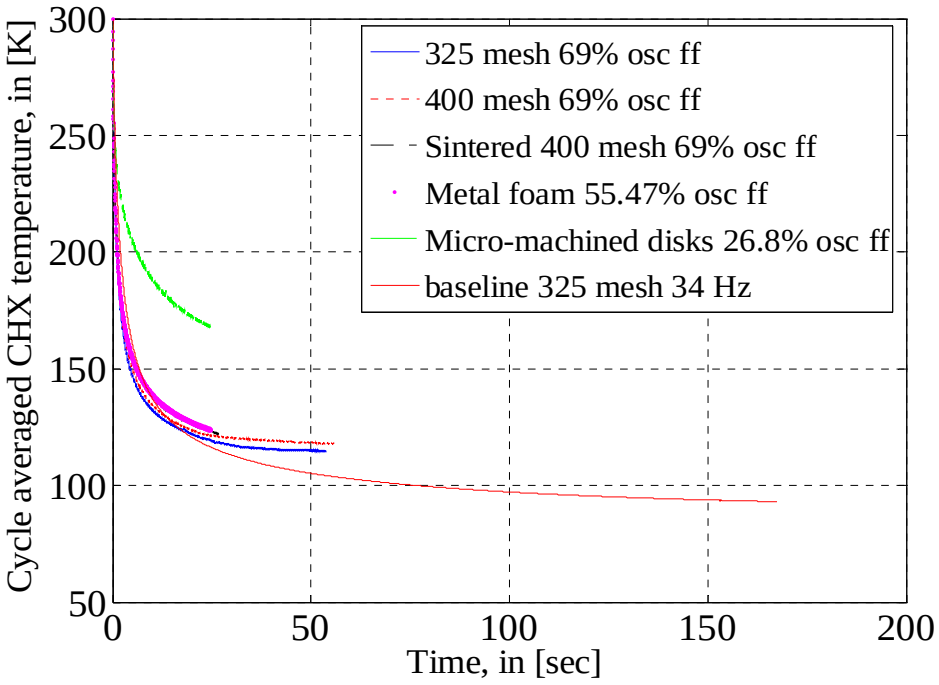

Figure 74. Cycle averaged CHX temperatures of ITPTC simulations using oscillatory friction factor relations and Cycle averaged CHX of baseline model simulation.

The baseline simulation in Figure 74 has approached the steady periodic operation. The CHX in the baseline system has cooled from 300 K to 92 K in approximately 190 seconds. All other simulated models except for the model with micro machined disk

regenerator closely follow the CHX temperature path of the baseline system. The CHX temperatures of all the simulated models are all only slightly higher compare to CHX temperature results of baseline case. For the model with micro machined disks, the predicted CHX temperature is significantly higher than the baseline model predictions. It appears that once all simulations reach the steady periodic state, their CHX temperatures will be higher than the baseline CHX temperature results.

Figure 75 displays the plot of cycle averaged values of the input compressor work, total surface heat rejection rate, and energy imbalance rate for the baseline model.

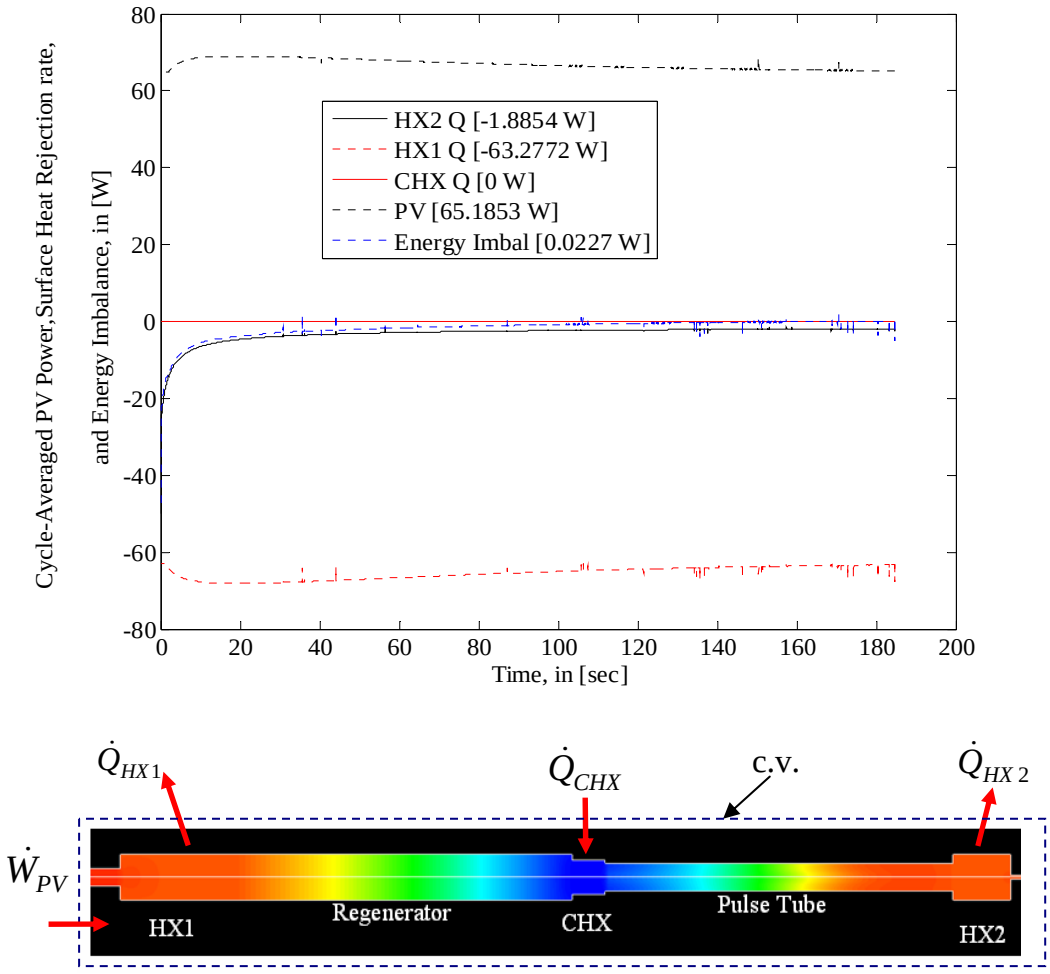

Figure 75. Cycle-averaged PV work, total heat surface rejection rate, and energy imbalance for the baseline model simulation.

The cycle averaged quantities and the energy imbalance rate are defined, respectively as:

$$\bar{\phi} = f \oint \phi \, dt \tag{5-7}$$

where ϕ is any property, and:

$$\left|\overline{\dot{E}_{imbalance}}\right| = \left|\overline{\dot{W}_{PV}}\right| + \left|\overline{\dot{Q}_{CHX}}\right| - \left|\overline{\dot{Q}_{HX\,1}}\right| - \left|\overline{\dot{Q}_{HX\,2}}\right| \tag{5-8}$$

As system approaches the steady periodic operation, the energy imbalance term of Eqn. (5-8) should asymptotically approach zero. According to figure 75 the energy conservation is nearly satisfied. The energy imbalance for the baseline simulations was

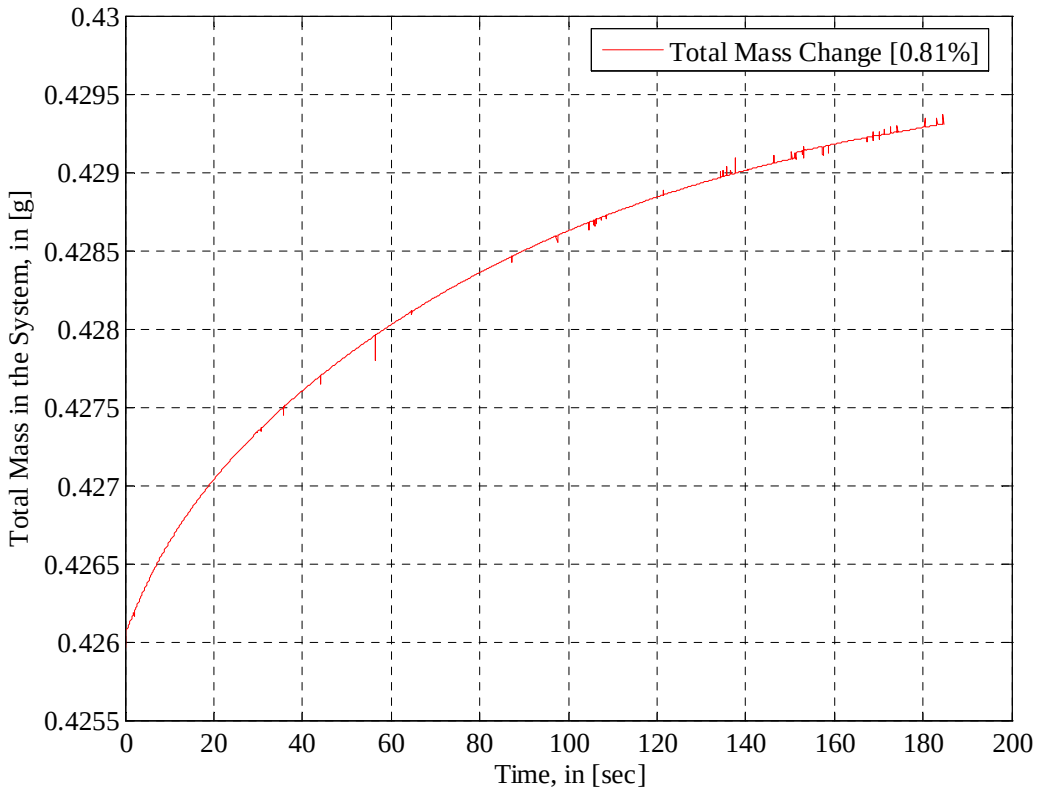

Figure 76. Cycle-averaged total mass in the entire system for baseline model simulation.

only 0.0227 W after 190 seconds. It appears that if simulation would to continue, the energy imbalance term would eventually reach an even lower value. Similar to energy balance the mass conservation was also checked. This was done by monitoring the total mass of the entire system. The total change in the mass was only 0.81% after 190 seconds.

The instantaneous snapshot of temperature and density contours of various components of the baseline ITPTC system are depicted in Figure 77. These contours correspond to 190 seconds. A cycle-average temperature drop of 200 ^{o}K can be observed across the regenerator and the CHX component reached the temperature of 92 ^{o}K without an applied heat load. When the cycle-average regenerator and pulse tube temperatures were plotted against the simulation time the regenerator component showed very small temperature fluctuations at near steady periodic operation, whereas for pulse tube significant temperature fluctuations were observed especially at the inlet and exit of the pulse tube locations. These large temperature fluctuations are believed to results from adiabatic compression and expansion. They are mainly due to the high frequency flows in pulse tube component, and the fact that there is no time for heat transfer between the periodically changing fluid and the surrounding solid structure.

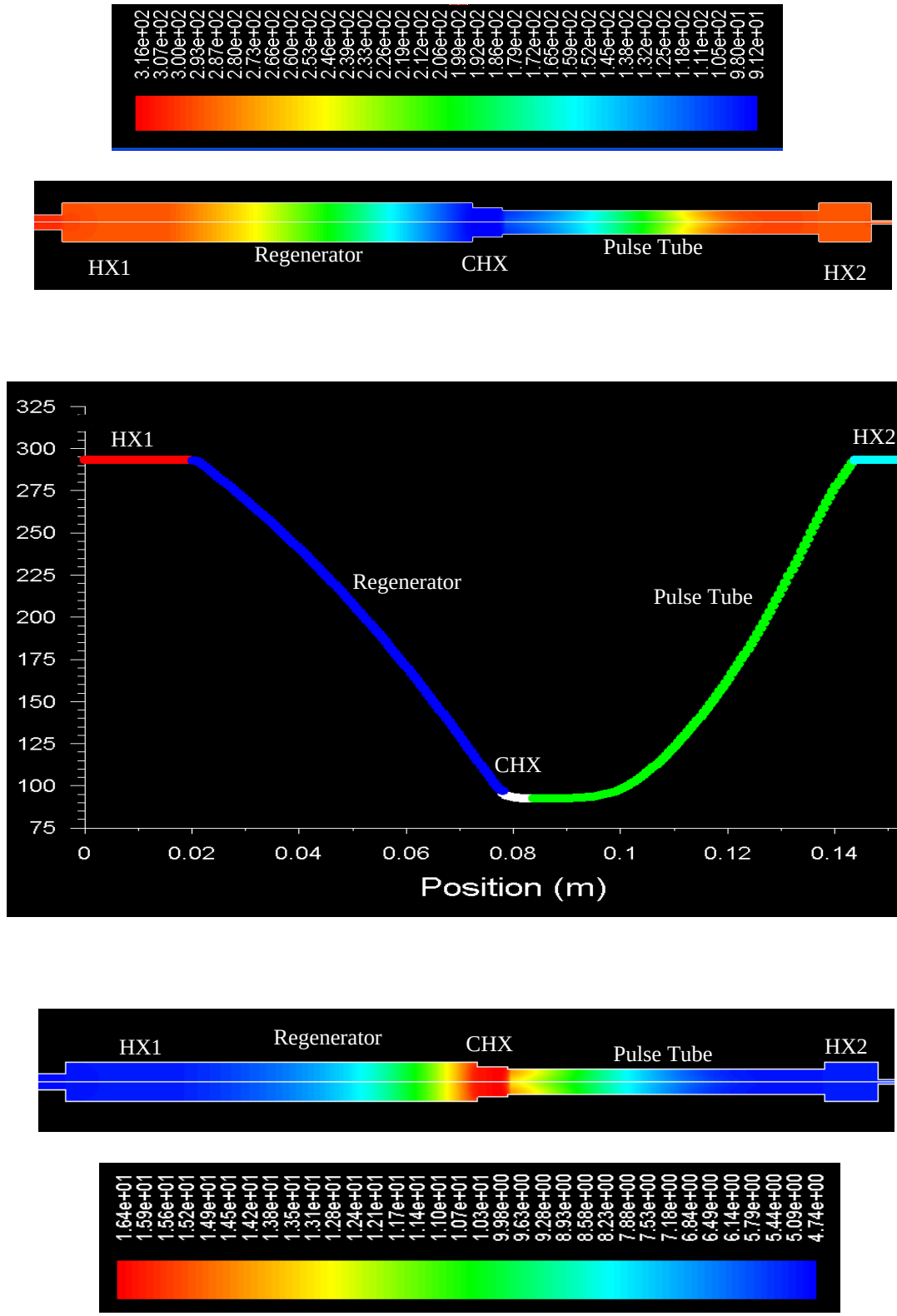

Figure 77. Baseline ITPTC model temperatures, in [K] (TOP) and density [kg/m3] (Bottom) contours.

The system level performance simulation results using steady friction closure relations are now discussed. The transient cycle-average CHX temperatures obtained in simulations representing five regenerator samples are shown in Figure 78.

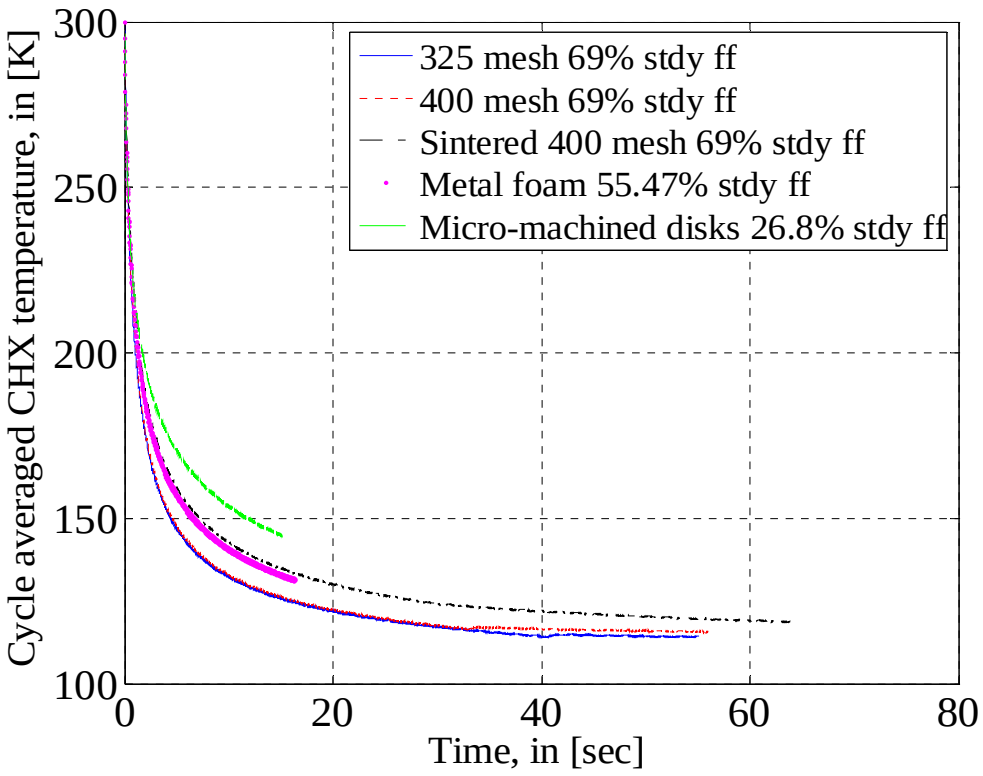

Figure 78. Cycle averaged CHX temperatures for the simulation of models with steady friction factor closure relations.

The transient cooling trend in Figure 78 is similar to the cooling trends in figure 74. The simulations evidently have not reached quasi-steady-periodic state. Nevertheless, the performance of the regenerator fillers can be compared based on the trends of the simulations results. Based on the results at 60 seconds simulation time the 325 mesh and 400 mesh simulations appear to have the best cooling performance followed by foam

metal, sintered 400 mesh, and micro-machined disk. The lowest CHX temperature, reached by 325 mesh regenerator simulation at approximately 60 seconds, is 115 ^{o}K.

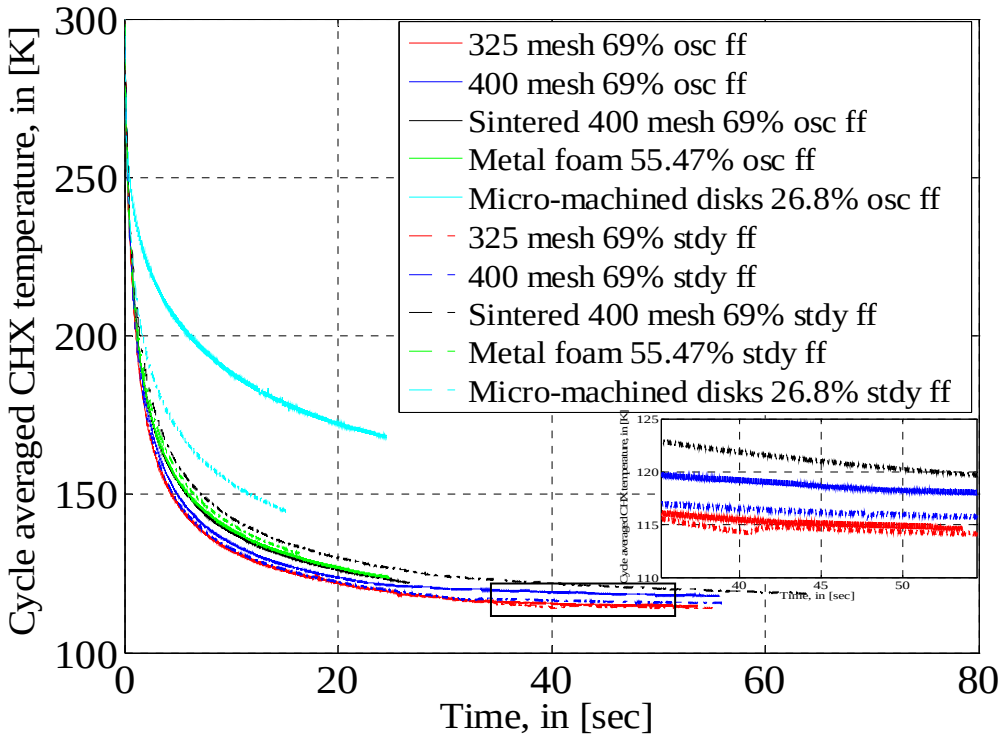

Figure 79. Cycle averaged CHX temperatures for the simulation of models with steady and oscillatory friction factor closure relations.

The transient, cycle-average CHX temperatures predicted by simulations using oscillatory and steady friction factor relations are plotted together in Figure 79. The cooling performance based on the cycle average CHX temperature, associated with using different regenerator closure relations can be clearly seen through figure 79. In general, all the simulated cases showed different quasi steady-periodic settling CHX temperatures. Among the simulated cases, the case that had the largest performance (temperature) deviation using oscillatory closure relation was the nickel micro-machined disks regenerator. For this case, the simulation using oscillatory closure relation had a

temperature difference of 35 degrees compared to the simulation using steady closure relation, after 16 seconds of simulation time. The sintered 400 mesh had the second largest performance deviation using oscillatory closure relations compare to steady friction factor. The above results clearly confirm that the uncertainties associated with using different closure relations significantly impact the overall cooler performance. Oscillatory friction factor should be used in all the ITPTC simulated models to more accurately predict the overall system level cooler performance.

It was noted earlier in Figure 74 that the nickel micro-machined disks regenerator had the worst cooling performance among the tested regenerator samples. This poor performance could be due to two reasons. The thermo-physical and transport properties of nickel could be one of the reasons. The high inertial friction coefficient in oscillatory flow conditions could also be the second reasons for the poor performance. In other words, the material properties and geometric characteristics of the regenerator can both contribute to its poor performance. In order to better assess the cause of this poor performance, an entire system level model was simulated again using different regenerator materials.

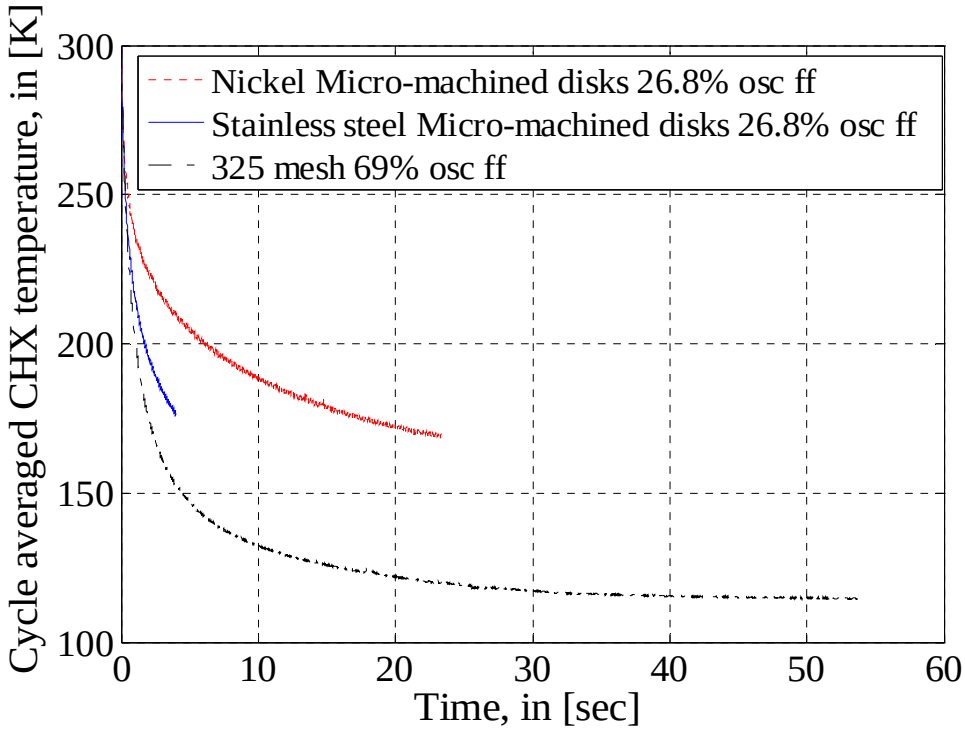

Figure 80. Cycle-averaged CHX temperatures of ITPTC simulations using steady friction factor relations.

The regenerator filler material was assumed to be stainless steel for this simulation, and the oscillatory hydrodynamic parameters were kept constant, therefore eliminating the effect of varying friction factors. As noted in Figure 80, the simulation with stainless steel material predicted significantly better performance in comparison with nickel. An additional temperature drop of 30 degrees in cold end temperature was predicted for stainless steel material. The main reason for the poor performance of the micro-machined disk regenerator is thus the unfavorable thermo-physical properties of nickel as the regenerator material. It is therefore recommended that stainless steel be utilized for the development of next generation regenerators.

CHAPTER 6

CONCLUSIONS

6.1 Conclusions

The anisotropic hydrodynamic parameters that appear in the volume-averaged momentum transport equation of the porous media/regenerator have been obtained through several series of experimental measurements and CFD-based empirical correlations. Experimental measurements were conducted using three different experimental test apparatuses. These apparatus were specially designed and built and were used for the measurement of macroscopic longitudinal and radial/lateral pressure drops across various regenerator fillers under steady and oscillatory flow conditions. Based on the measured pressure drop data either for steady or oscillatory flow, CFD-assisted model simulations were performed to correlate the anisotropic hydrodynamic parameters. As a result, dimensionless friction factors for both steady and oscillatory flow conditions were obtained for some of the most widely used regenerator fillers.

For the fine wire meshed type regenerators (325 and 400 mesh screens), and nickel micro-machined disks, the oscillatory dimensionless axial friction factors were significantly higher in comparison with the steady axial friction factors. However, for the metallic foam metal and sintered 400 mesh regenerators, the oscillatory-flow friction factors were smaller than the steady flow friction factors. The radial-to-axial directional

friction factor ratios (f_{radial} / f_{axial}) were also quantified and compared for the assessment of anisotropy in the regenerators. Based on the experimental measurements and model simulations, the 325 mesh screen (for steady flow) and sintered 400 mesh (oscillatory flow) regenerators have noticeably larger radial flow resistances compared to their axial flow resistances.

The system–level simulations were performed and the simulation results were compared with experimental measurements. The 325 mesh regenerator filler pressure drop simulations showed excellent agreement with data, in terms of the magnitudes of pressures and the phase angles between the inlet pressures and the exit pressures, for the frequency range covering 5 Hz to 60 Hz. Similarly, excellent agreement between simulation results and data was observed for all simulated regenerator samples. Furthermore, to verify the fidelity of the proposed methodology for determining the anisotropic hydrodynamic parameters, a hot wire anemometry (HWA) system was incorporated in the test apparatus to measure the local instantaneous velocities at the inlet to the porous test section in a series of test with the foam metal and sintered 400 mesh screens regenerator fillers. The measured local instantaneous velocity data were compared with the simulation predictions. In this way, the experimentally measured local and instantaneous mass flux at the inlet of the regenerator filler was directly compared with simulation predictions. The results showed excellent agreement between the experimental data and the model simulations.

After closure relations were found for the hydrodynamic interactions between the working fluid and the regenerator filler structures, parametric simulations were performed in order to compare the overall thermal performance of the tested regenerator

fillers under oscillatory flow conditions. The 325 mesh regenerator, which had the third lowest oscillatory friction factor among the five tested regenerator fillers, had the best system level performance among all simulated regenerator fillers. The nickel micro machined disks regenerator filler had the worst thermal performance. The poor performance of the micro machined disks was mainly due to the inferior thermal properties of nickel as a regenerator filler material, as compared to stainless steel. If stainless steel were to be used instead of nickel, the thermal performance of the perforated disks would be much improved. The results also showed that the regenerator having the lowest friction factor does not necessarily produce the best system level thermal performance.

6.2 Contributions

Two significant contributions have been made in this research. A significant contribution is the successful demonstration of the feasibility of CFD-based multi-dimensional modeling and simulation of the entire inertance tube pulse tube cryocooler systems in order to predict their overall system level performance. In fact, using this new proposed modeling methodology we were able to perform multi-D modeling and accurately predict the system level performance parameters in a series of cases. This first principle based modeling approach solves two-dimensional (and three-dimensional, when needed) transient flow and heat transfer conservation equations to simulate the actual experiment without any arbitrary assumptions. The method in fact replicates the actual experiment by performing system level transient analysis starting from an equilibrium

initial condition, and as a result, the actual cooling time can also be predicted by the method. In this study it was demonstrated that complete CFD simulations can indeed be performed with very little overall mass and energy imbalances.

The second contribution of this investigation was the successful measurement and correlation of anisotropic (axial and radial) hydrodynamic parameters under oscillatory flow conditions using a newly proposed CFD-assisted methodology. The proposed methodology simulates the experiments using exact measured pressure waveforms including up to three fundamental frequencies. Prior to this investigation, only the first fundamental frequency of pressures was generally used to impose the pressure boundary conditions at the inlet of the regenerator. The proposed methodology also has the capability of matching the magnitude and the phase angle of the measured pressures at the exit of the regenerator whereas for other correlations they could only match the magnitudes.

Three different experimental test apparatuses were designed, fabricated, and assembled by this author. These test apparatuses were designed with high modularity. They can be easily modified in order to carry out other high-end regenerator investigations.

6.3 Future Work

All the resistance simulated results shown in this investigation assumed local thermal equilibrium between the gas and solid matrix in the regenerator. In other words, the model assumed no heat transfer resistance between the gas and the solid matrix in the regenerator. The potential thermal non-equilibrium in real regenerators should be

considered in CFD models to more accurately predict the system level performance of the ITPTC system. Little is known about the details of solid-fluid thermal non-equilibrium interactions in regenerator fillers, however, in particular for periodic flows. Experimental and computational investigations aimed at understanding the solid-fluid thermal interactions in micro-porous filler structures under periodic flow are therefore are recommended.

With respect to the afore-mentioned solid-fluid thermal interactions in periodic flow, direct simulation at a pore level of the regenerator fillers can be a promising and helpful technique, since direct experimental measurements are very difficult. The feasibility of this approach has been demonstrated for steady flow, and simulations at pore level have already been done [48-50]. However, these were only limited to incompressible and steady state flow conditions. Direct simulations using compressible periodic flow conditions are needed. Such simulations will further enhance the fundamental theory about porous media.

As mentioned earlier, the test apparatus built in this investigation were designed to be modular and relatively easy to modify or enhance. Modification of experiment test apparatus for further validation of this investigation, and testing other relevant phenomena is strongly recommended. Some ideas in this line are as follows. Implementation of a second hot wire probe at the exit of the regenerator could further validate the CFD predictions. Constant current anemometers can also be incorporated in the test apparatus to measure the transient temperatures at both ends of the regenerator. The additions of these sensors would completely characterize the thermal fluid properties of the regenerator. Lastly, an investigation essentially identical to that reported in this

thesis should be repeated at cryogenic operating temperatures. The current investigation was performed at temperatures of almost 300 K. Repeating these experiments at cryogenic temperatures would provide hydrodynamic parameters directly applicable to cryogenic temperatures.

Further equipment improvements are needed at the GT Cryogenic Laboratory in order to carry out more advance cryocooler research. Equipment enhancement can start with most important equipment, namely the compressor. The current compressor, which has 4.29 cc swept volume, was originally designed for the purpose of studying tactical coolers. In all of our experiments this same compressor was used to simulate the oscillatory flow conditions and generate pressure oscillation. With this compressor we were very limited and could not achieve higher mass flow rates in our experiments. A much larger swept-volume compressor is needed for higher mass flows. A new data acquisition system would also improve the data collecting capability.

APPENDIX A

USER DEFINE FUNCTIONS

User Defined Functions for Piston Velocity and Transient Pressures.

Piston Velocity

```
#include "udf.h"
DEFINE_CG_MOTION(vel_comp, dt, vel, omega, time, dtime)
{
  real freq=40.0;                    // [Hz]
  real w=2.0*M_PI*freq;              // [rad/s]
  real Xcomp=0.0065;                 // [m]
  /* reset velocities */
  NV_S (vel, =, 0.0);
  NV_S (omega, =, 0.0);
  vel[0] = w*Xcomp*cos(w*time);
}
```

Transient Pressure Boundary Conditions

```
/*************************************************************************
unsteady_pressure.c
UDF for specifying a transient pressure
*************************************************************************/
#include "udf.h"
#define freq 30                                  // [Hz]
#define Po 0                                     // [Pa]
#defineP1 103109.1655                            // [Pa]
#defineP2 1039.75895                             // [Pa]
#defineP3 6963.877075                            // [Pa]
#definePhi1 -122.3259594                         // [Degree]
#definePhi2 94.90892385                          // [Degree]
#definePhi3 51.22300525                          // [Degree]
DEFINE_PROFILE(unsteady_pressure_inlet, thread, position)
{
  face_t f;
  real t = CURRENT_TIME;
          real omega = 2*M_PI*freq;
          real B=1.001;
  begin_f_loop(f, thread)
    {
      F_PROFILE(f, thread, position) =
          (Po +
P1*cos(1*omega*t+Phi1*M_PI/180)+P2*cos(2*omega*t+Phi2*M_PI/180)+P3*cos(3*o
mega*t+Phi3*M_PI/180))*B;
```

```
  }
end_f_loop(f, thread)
}
```

APPENDIX B

PRESSURE SIMULATION RESULTS FOR TESTED REGENERATOR FILLERS

Prediction of pressure amplitude ($P\text{-}P_{mean}$), in [Pa] and phase at P_2, and their comparison to experimental data.

Metallic Foam Metal (MFM)

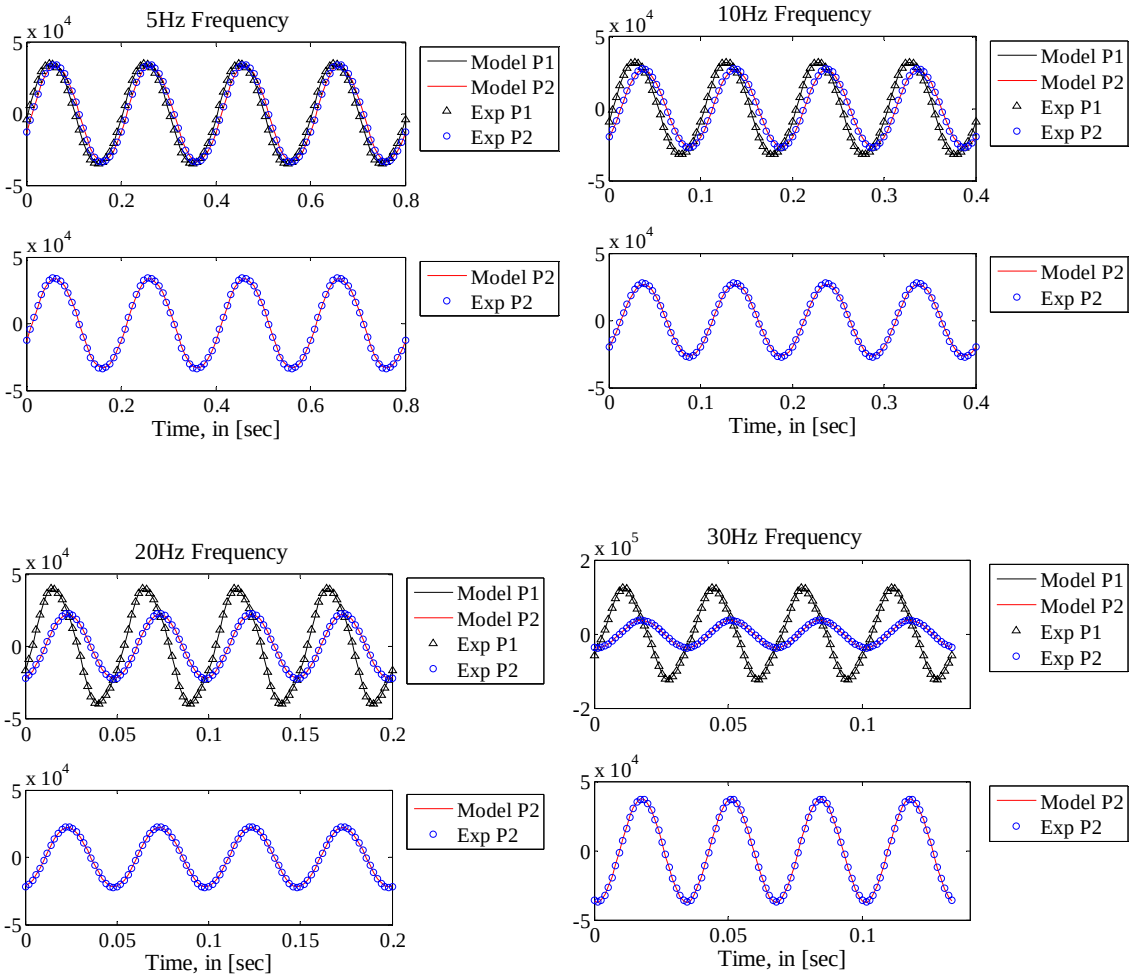

Figure B.1. Prediction of pressure amplitude ($P\text{-}P_{mean}$), in [Pa] and phase at P_2, and their comparison to experimental data for MFM, 5 Hz, 10 Hz, 20 Hz, 30 Hz.

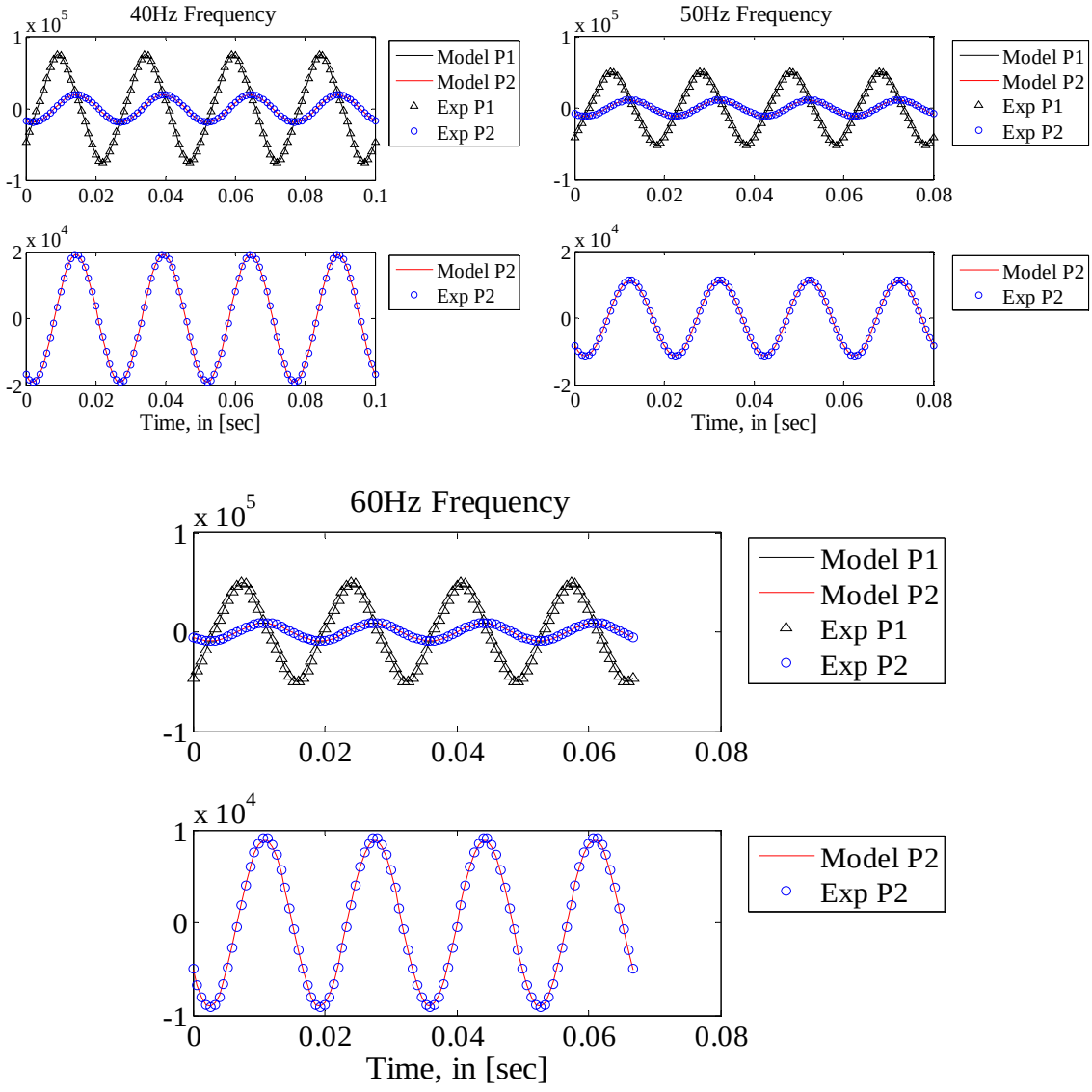

Figure B.2. Prediction of pressure amplitude (P- P_{mean}), in [Pa] and phase at P_2, and their comparison to experimental data for MFM, 40 Hz, 50 Hz, 60 Hz.

Sintered 400 Mesh (S4M) Results.

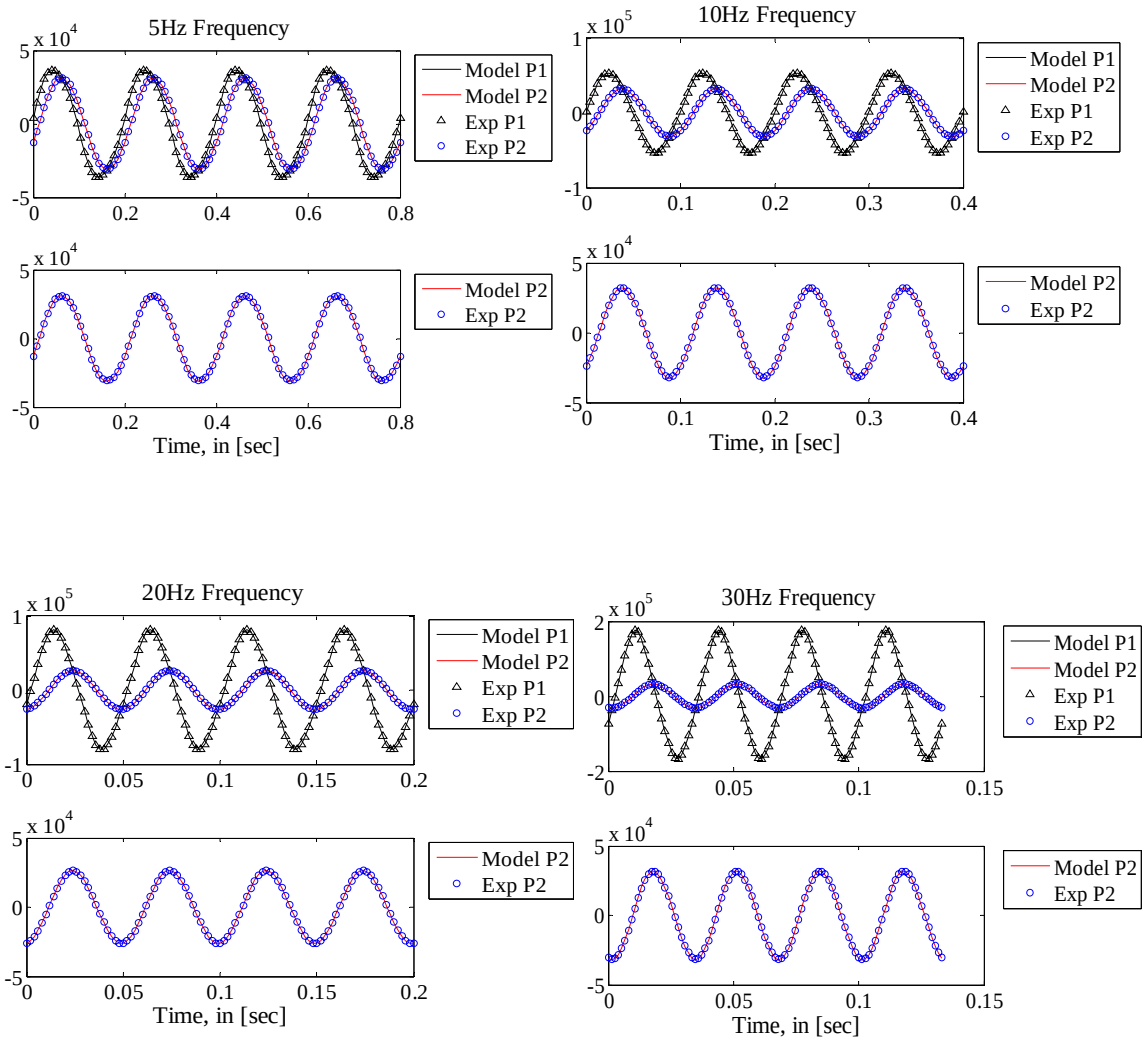

Figure B.3. Prediction of pressure amplitude (P- P_{mean}), in [Pa] and phase at P_2, and their comparison to experimental data for S4M, 5 Hz, 10 Hz, 20 Hz, 30 Hz.

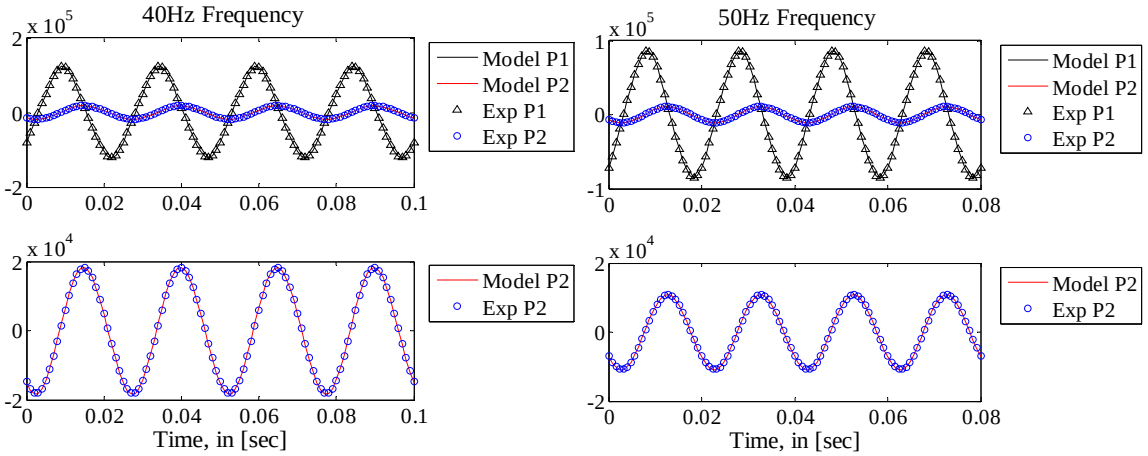

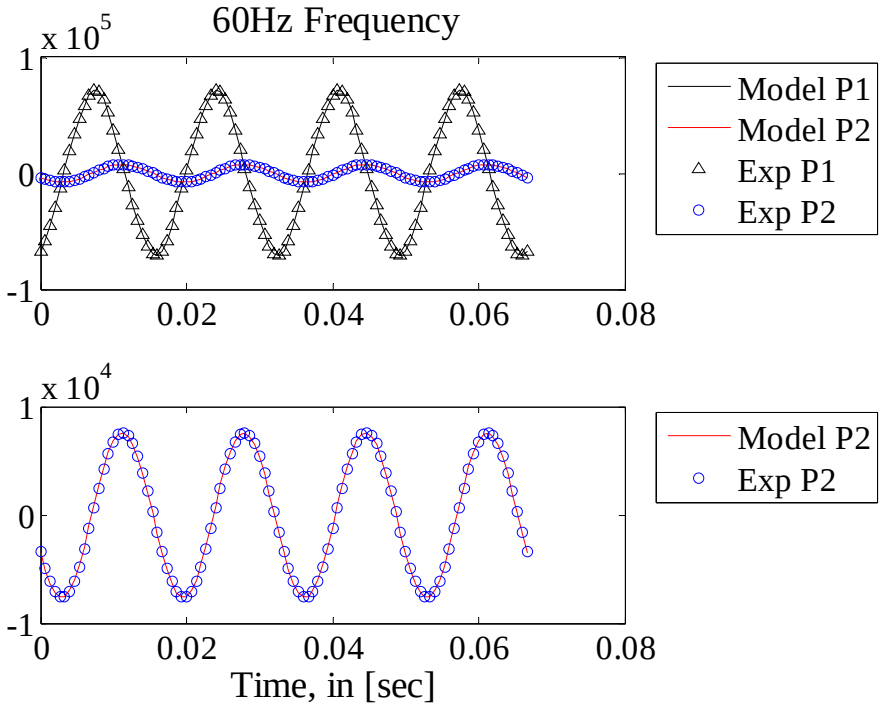

Figure B.4. Prediction of pressure amplitude (P- P_{mean}), in [Pa] and phase at P_2, and their comparison to experimental data for S4M, 40 Hz, 50 Hz, 60 Hz.

400 Mesh Screens (4MS)

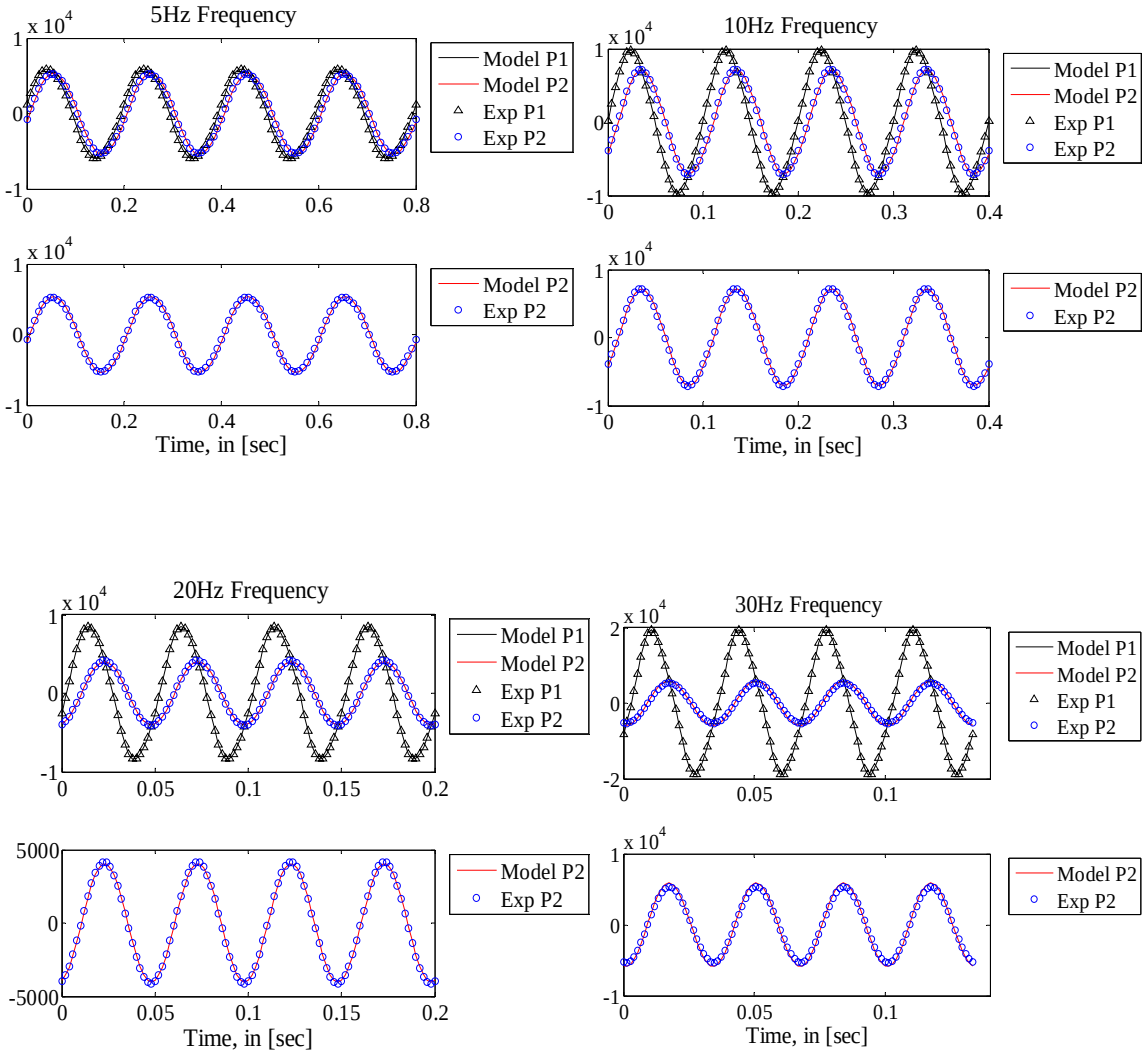

Figure B.5. Prediction of pressure amplitude (P- P_{mean}), in [Pa] and phase at P_2, and their comparison to experimental data for 4MS, 5 Hz, 10 Hz, 20 Hz, 30 Hz.

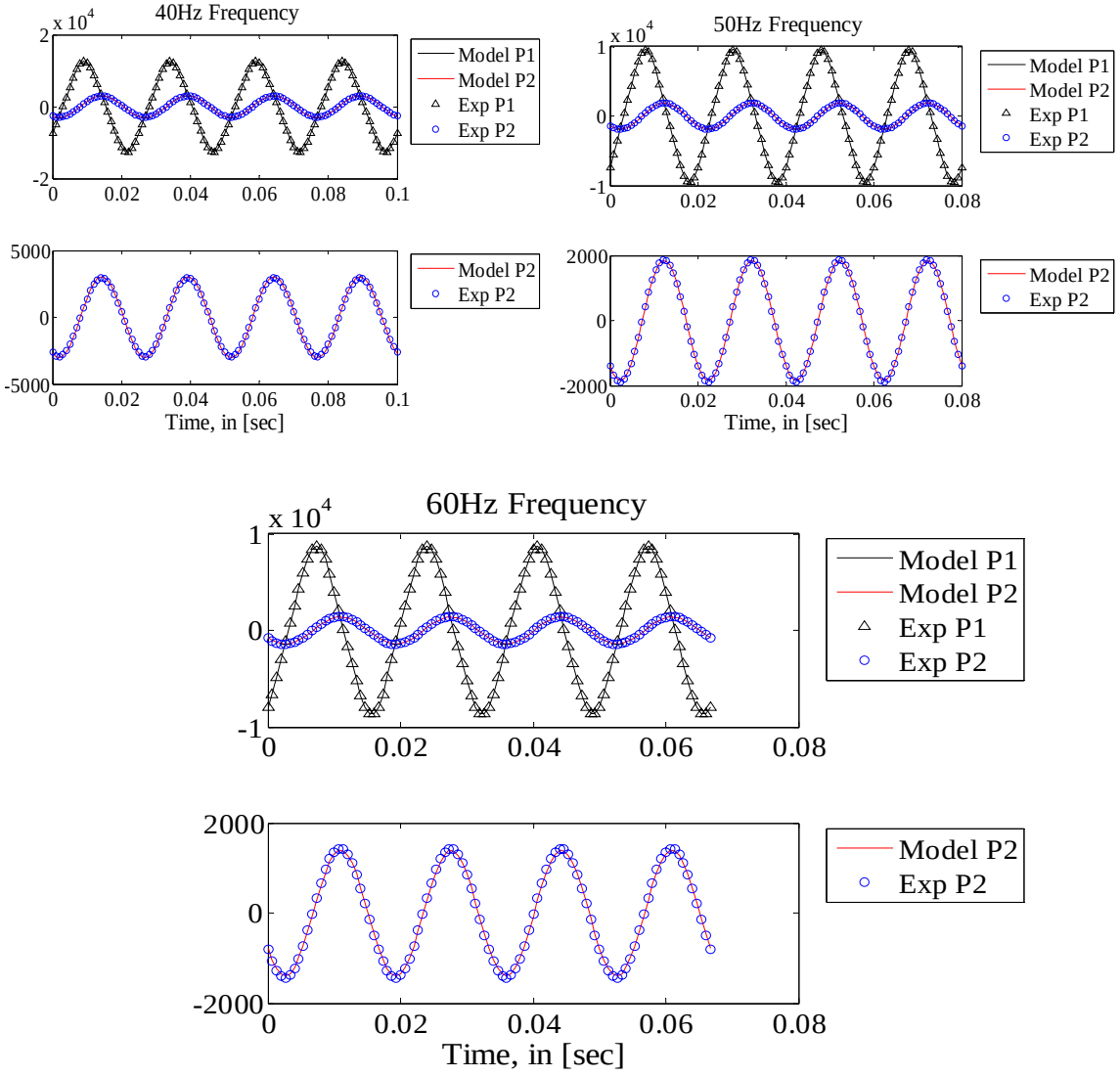

Figure B.6. Prediction of pressure amplitude (P- P_{mean}), in [Pa] and phase at P_2, and their comparison to experimental data for 4MS, 40 Hz, 50 Hz, 60 Hz.

325 Mesh Screens (3MS)

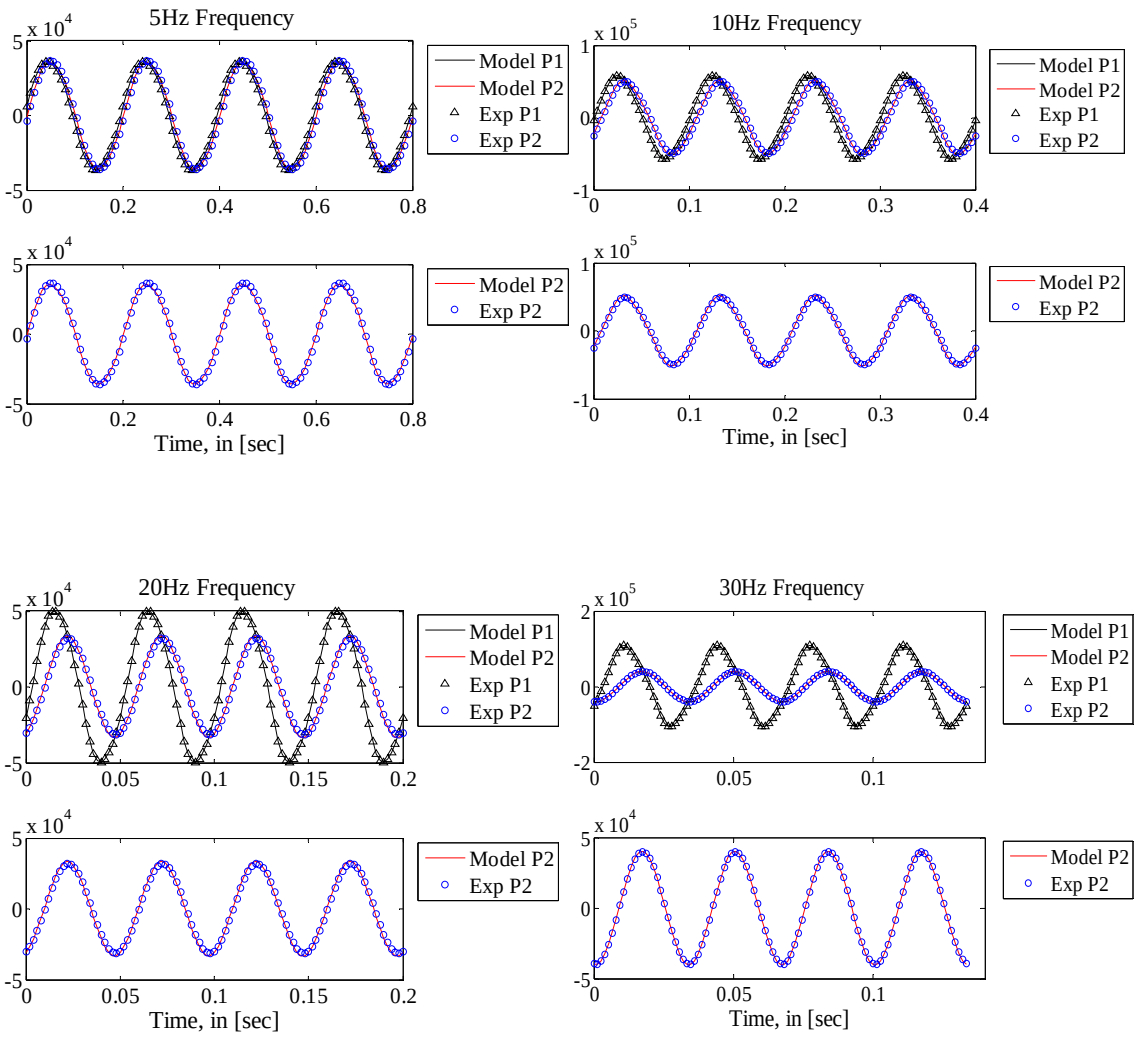

Figure B.7. Prediction of pressure amplitude (P- P_{mean}), in [Pa] and phase at P_2, and their comparison to experimental data for 3MS, 5 Hz, 10 Hz, 20 Hz, 30 Hz.

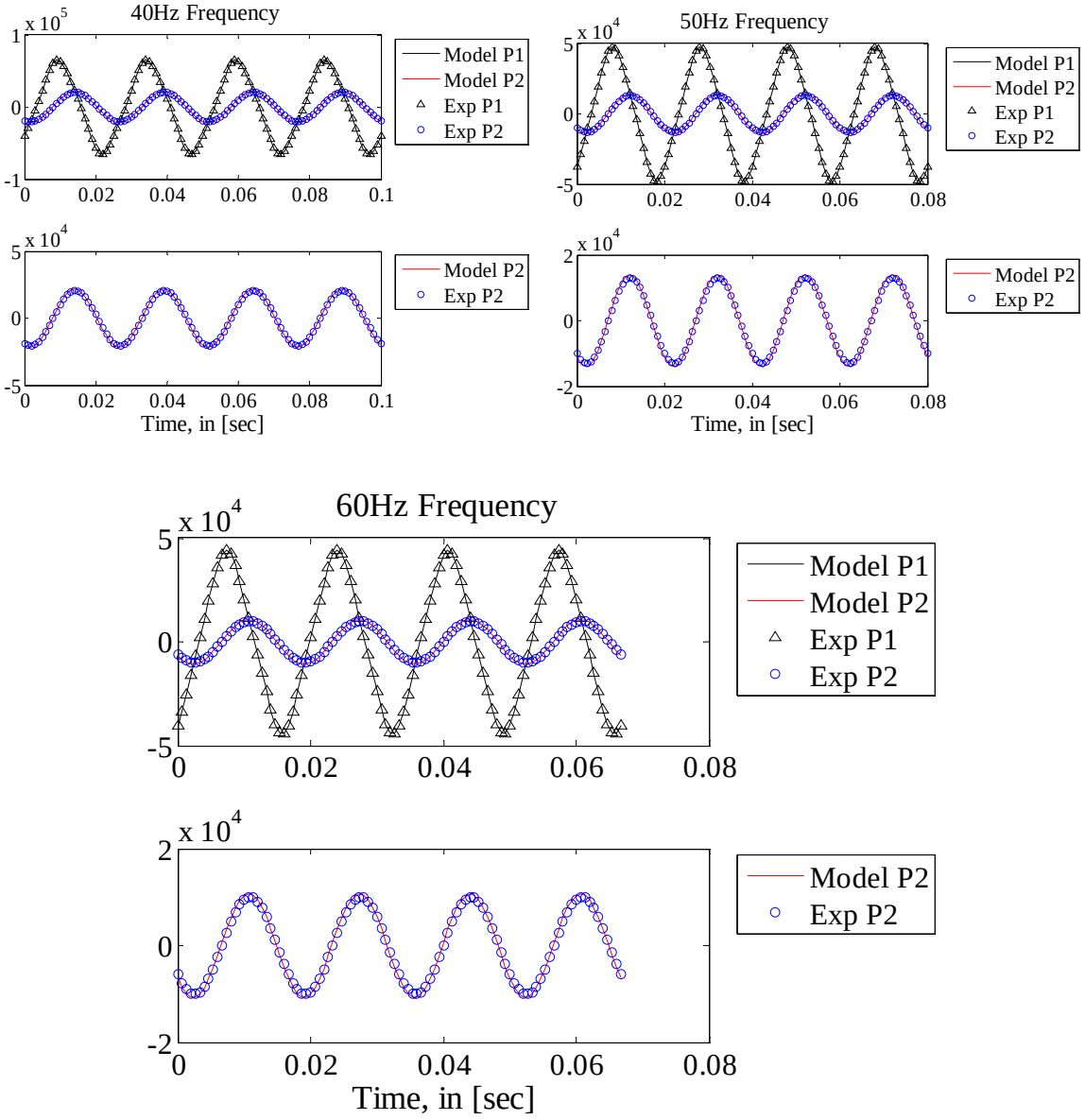

Figure B.8. Prediction of pressure amplitude (P- P_{mean}), in [Pa] and phase at P_2, and their comparison to experimental data for 3MS, 40 Hz, 50 Hz, 60 Hz.

Nickel Micro-machined Disks (NMD)

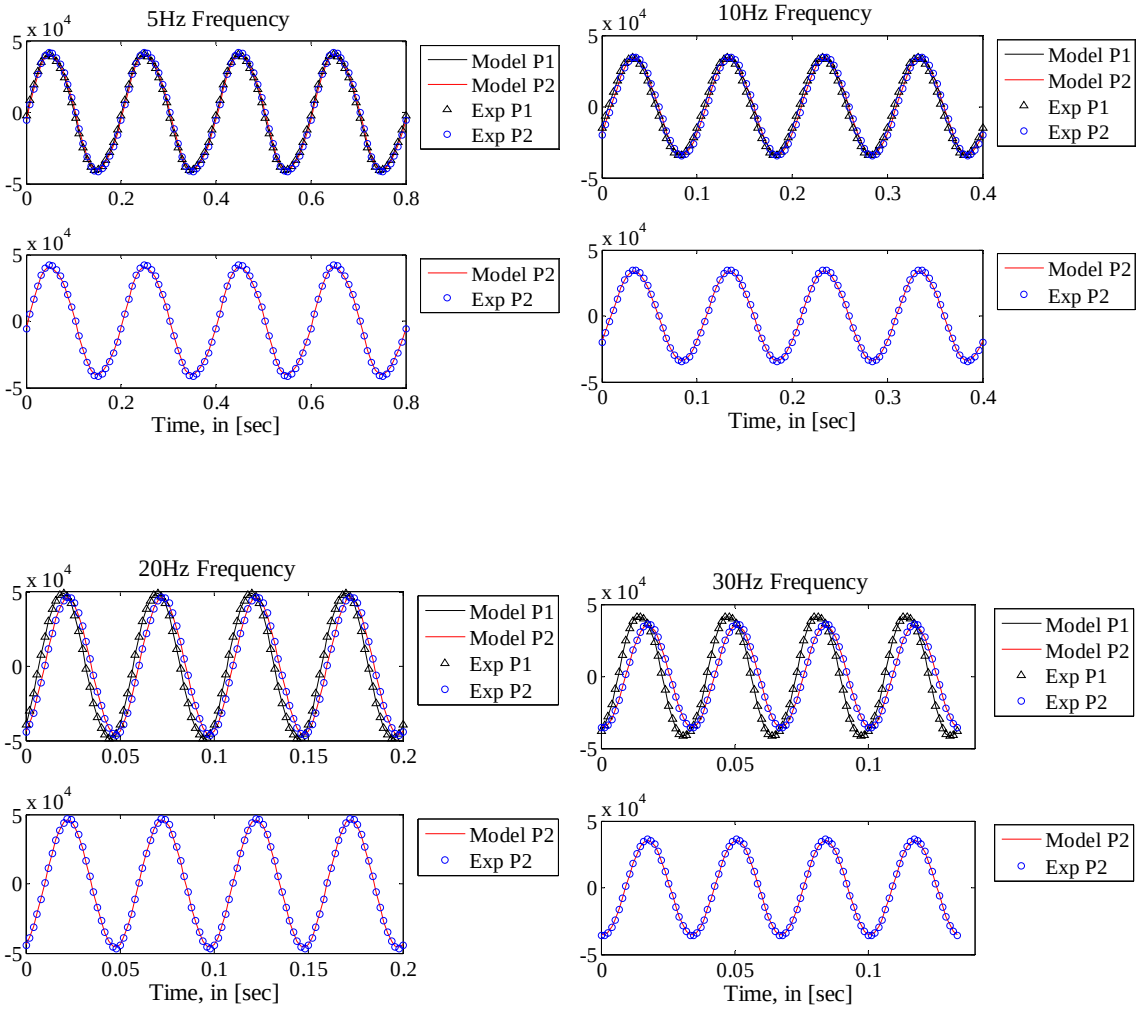

Figure B.9. Prediction of pressure amplitude (P- P_{mean}), in [Pa] and phase at P_2, and their comparison to experimental data for NMD, 5 Hz, 10 Hz, 20 Hz, 30 Hz.

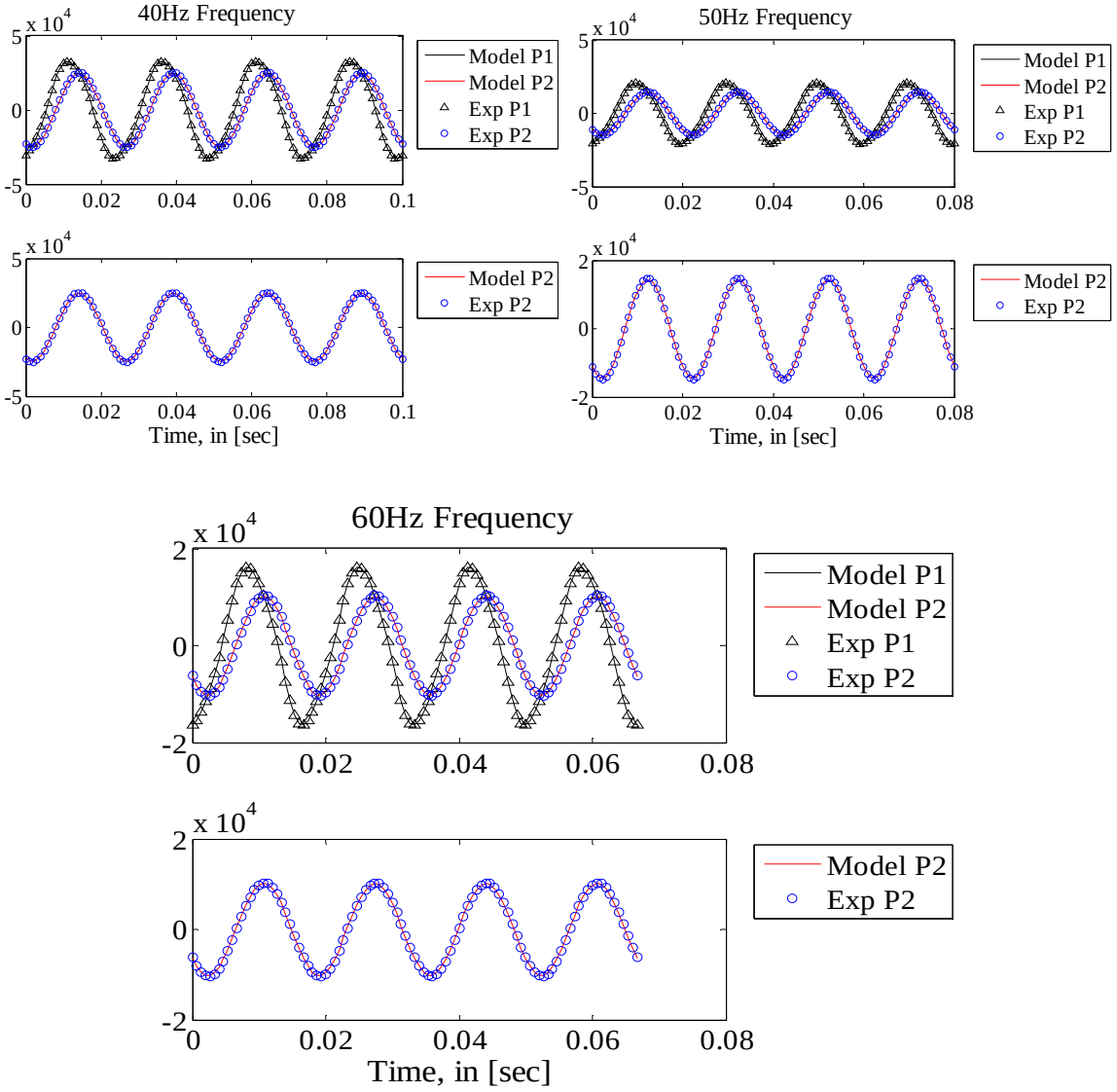

Figure B.10. Prediction of pressure amplitude (P- P_{mean}), in [Pa] and phase at P_2, and their comparison to experimental data for NPD, 40 Hz, 50 Hz, 60 Hz.

400 Mesh Screens 300 psig (4MS300)

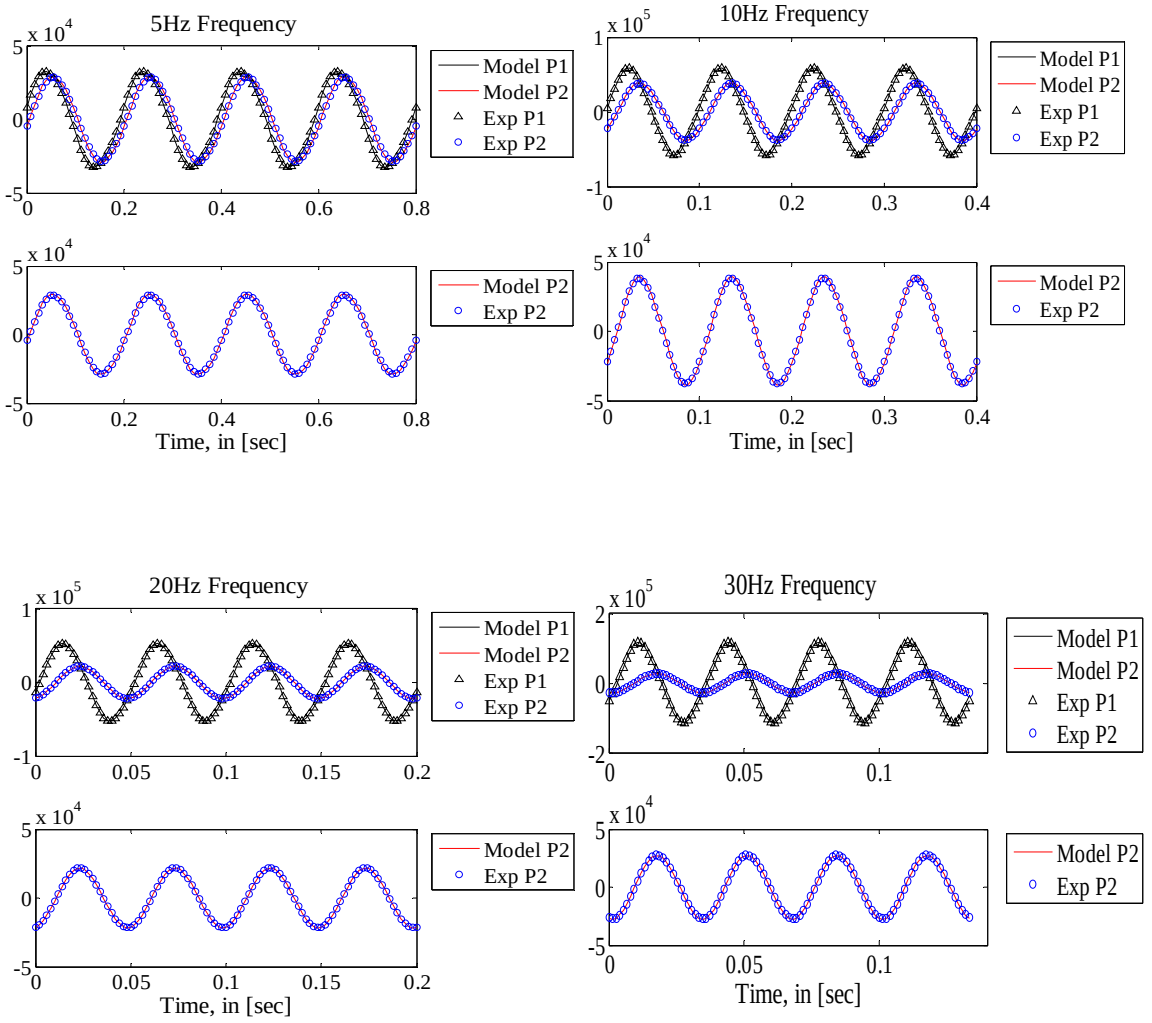

Figure B.11 Prediction of pressure amplitude (P- P_{mean}), in [Pa] and phase at P_2, and their comparison to experimental data for 4MS300, 5 Hz, 10 Hz, 20 Hz, 30 Hz.

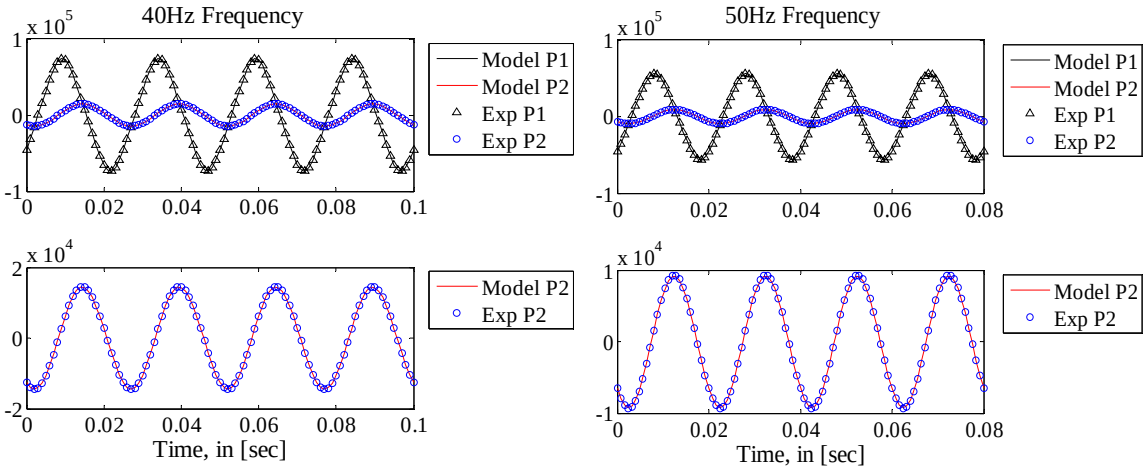

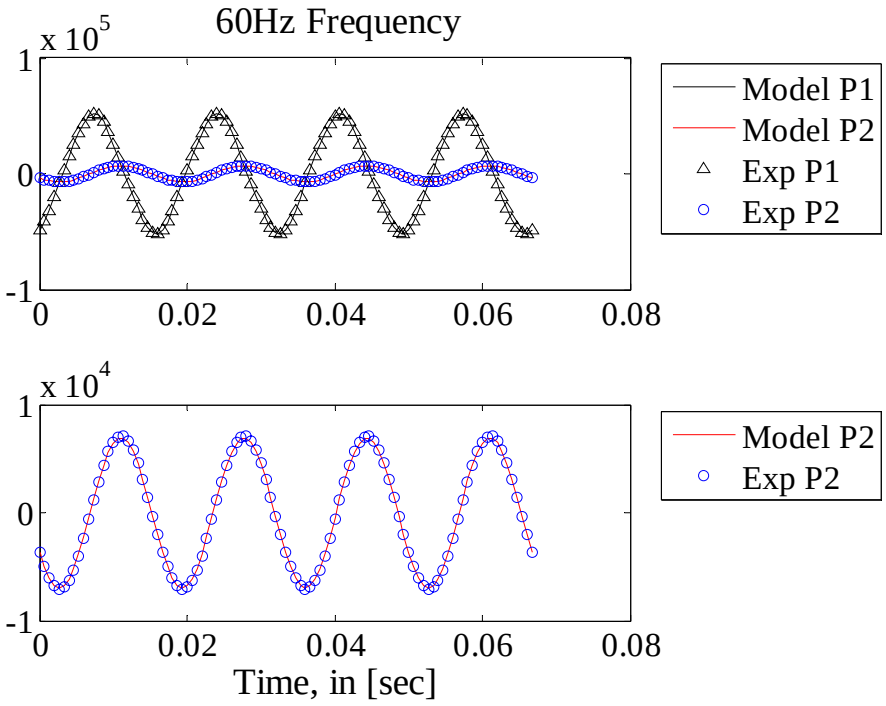

Figure B.12. Prediction of pressure amplitude (P- P_{mean}), in [Pa] and phase at P_2, and their comparison to experimental data for 4MS300, 40 Hz, 50 Hz, 60 Hz.

325 Mesh Screens without Forchheimer inertial effect (3MSNI)

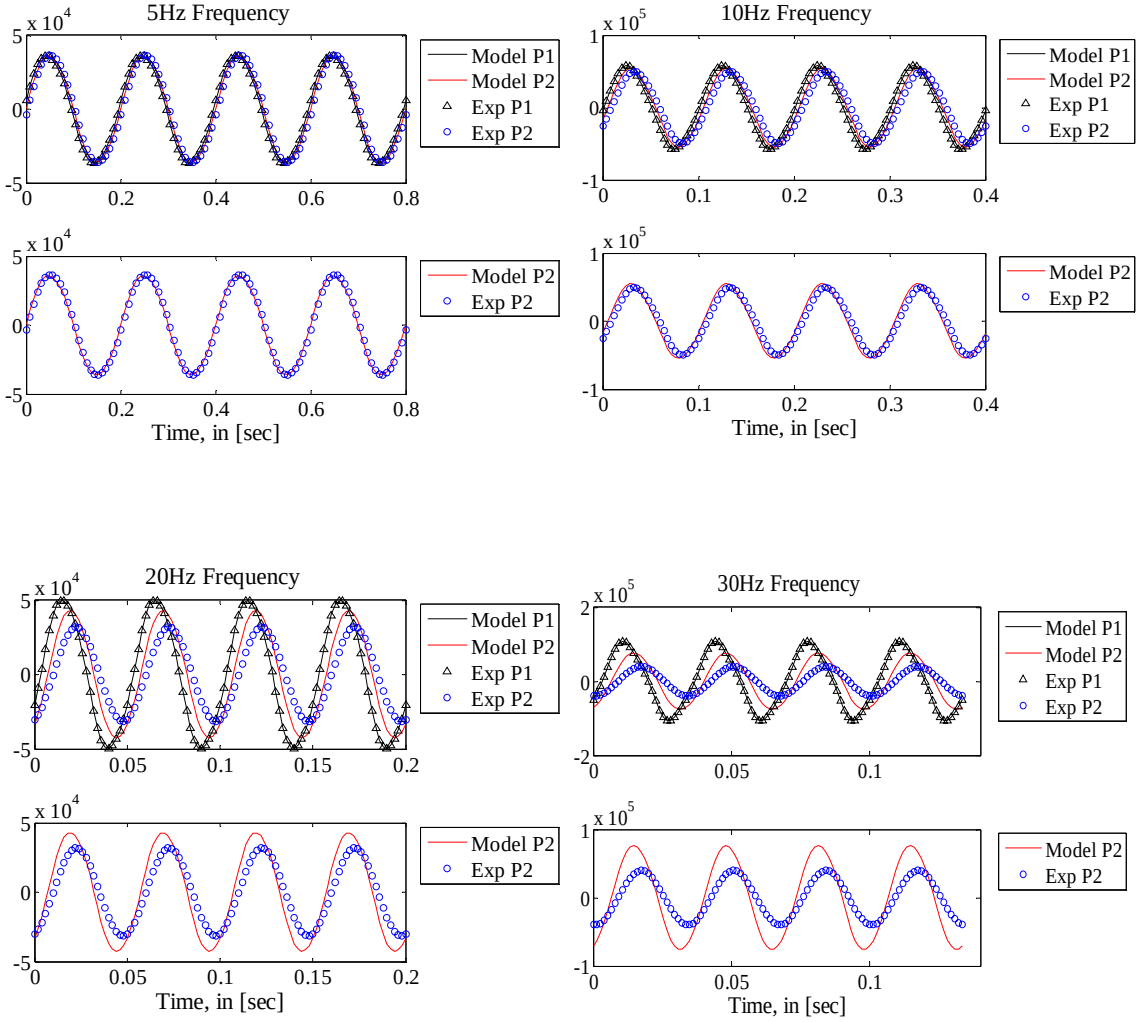

Figure B.13. Prediction of pressure amplitude (P- P_{mean}), in [Pa] and phase at P_2, and their comparison to experimental data for 3MSNI, 5 Hz, 10 Hz, 20 Hz, 30 Hz.

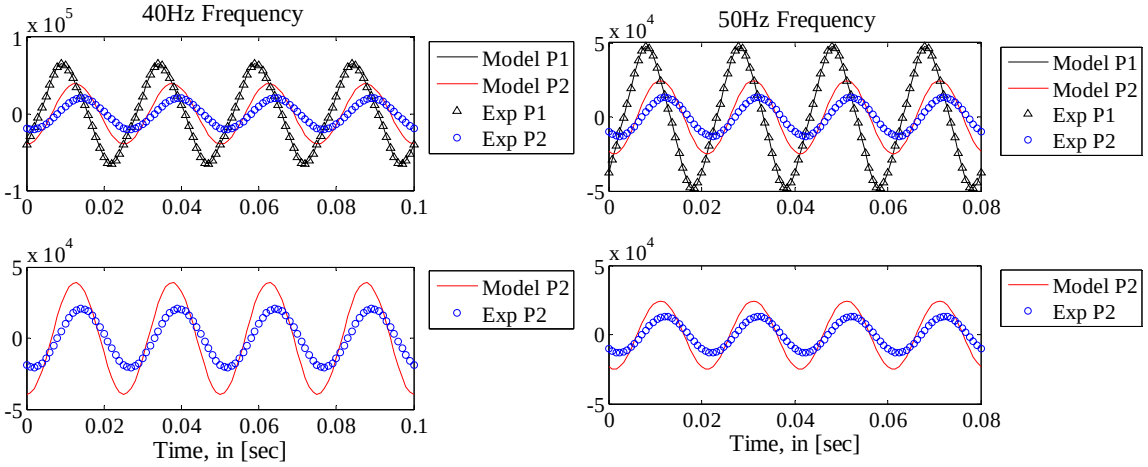

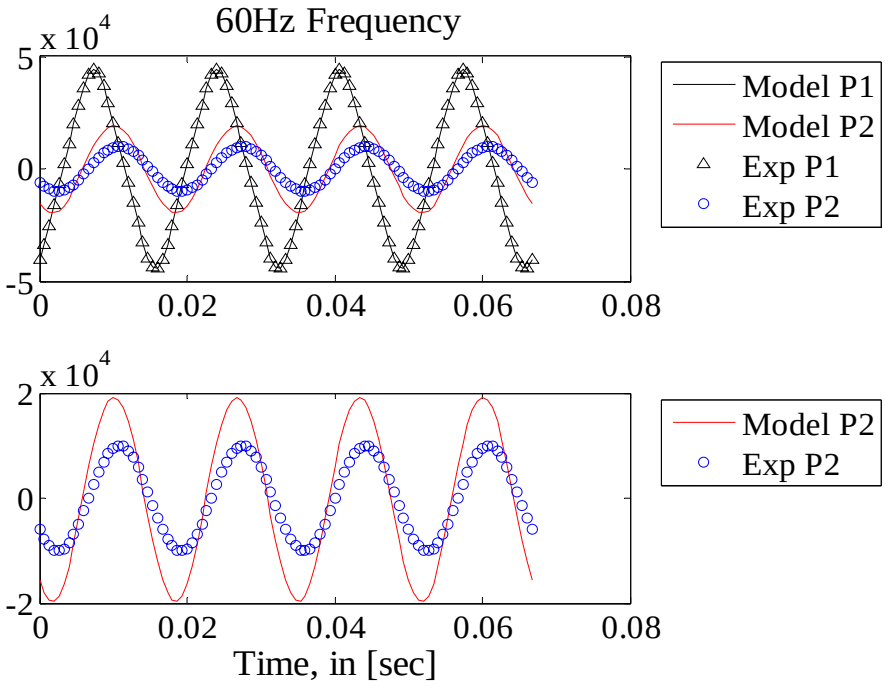

Figure B.14. Prediction of pressure amplitude (P- P_{mean}), in [Pa] and phase at P_2, and their comparison to experimental data for 3MSNI, 40 Hz, 50 Hz, 60 Hz.

APPENDIX C

MINIATURIZATION OF PULSE TUBE CRYOCOOLERS

In this section, system level performance of miniature ITPTC systems are described and presented.

C.1 CFD Model for the Preliminary Assessment of PTC Miniaturization

As explained earlier in section 2.3 miniaturization of cryocoolers in order to facilitate their application in weight and size-sensitive systems is a major challenge. Given the complexity of the coupled thermal-fluid phenomena in PTCs, it is not evident at all whether significant miniaturization of current PTC designs is feasible. A preliminary assessment of this issue has been performed in this study. To this end, the system level performance associated with ITPTC component miniaturizations was investigated by modeling and simulating entire miniature ITPTC systems. A well defined fully working baseline ITPTC model was chosen for this purpose. The ITPTC model (MOD1) previously used in this author's Master Thesis [44] is chosen as a baseline model and, using this model three miniature ITPTC systems were developed. For the first model, the length and diameter of all components in the baseline model were reduced to 80 % of their original baseline model dimensions. For the second and the third models the lengths and diameters were all reduced to 50% and 20%, of their original baseline values, respectively. Using linear scaling feature in Fluent the lengths and diameters were easily reduced to the desired dimensions.

Modeling procedures that were used in section 4.4 were applied here to model the three miniature ITPTC systems. All the necessary components such as compressor, heat exchangers, regenerator, pulse tube, buffer volume, and inertance tube were modeled, and simulations were performed using transient analysis. All three models were simulated

using approximately 4000 mesh nodes and using residual convergence criteria of 0.001 for the mass, *x*-velocity, and *r*-velocity; and the 1e-6 for energy. The physical dimensions and total volumes of the modeled systems are summarized in Table C.1.1.

Adiabatic wall boundary condition is assumed for all the walls in the models except for the ones that are listed in Table C.1.1. The boundary conditions and initial temperatures for the afore-mentioned systems are summarized in Table C.1.2.

Table C.1.1 Physical dimensions and total volumes of the miniature ITPTC models.

Model index	% of Baseline Model	Components	Length, [mm]	Diameter, [mm]	L/D, [-]	Wall thickness WT, [mm]	Total fluid volume [cc]
M100BL	100%	REGENERATOR	58	8	7.25	0.2	78.07
M100BL WT		PULSE TUBE	60	5	12	0.2	
M80BL	80%	REGENERATOR	46.4	6.4	7.25	0.16	39.72
M80BL WT		PULSE TUBE	48	4	12	0.16	
M50BL	50%	REGENERATOR	29	4	7.25	0.1	9.77
M50BL WT		PULSE TUBE	30	2.5	12	0.1	
M20BL	20%	REGENERATOR	11.6	1.6	7.25	0.04	0.636
M20BL WT		PULSE TUBE	12	1	12	0.04	

Table C.1.2 Boundary and initial conditions of miniature ITPTC models.

Miniaturization models	Models			
Study cases	M20BL	M50BL	M80BL	M100BL
HX1 Wall [^{o}K]	293	293	293	293
HX2 Wall [^{o}K]	293	293	293	293
Regenerator Type	325 Mesh	325 Mesh	325 Mesh	325 Mesh
Regenerator Material	Stainless Steel	Stainless Steel	Stainless Steel	Stainless Steel
β [m^2]*	1.061e-10	1.061e-10	1.061e-10	1.061e-10
C [1/m]*	76090	76090	76090	76090
Regenerator Porosity	0.692	0.692	0.692	0.692
CHX, HX1, and HX2 material	Copper	Copper	Copper	Copper
β_c [m^2]	1.061e-10	1.061e-10	1.061e-10	1.061e-10
C_c [1/m]	76090	76090	76090	76090
CHX, HX1 and HX2 Porosity	0.68	0.68	0.68	0.68
Initial CHX Temperature [^{o}K]	300	300	300	300
CHX LOAD (W)	0	0	0	0

*These values are obtained from the experiment data of Harvey [1] and for all simulations hydrodynamic parameters were assumed isotropic.

C.2. System Level Performance Results of Miniature ITPTC

A brief discussion of the problems associated with miniaturization of PTCs was presented in Sect 2.3. As mentioned, miniaturization of PTCs is highly desirable because it facilitates the application of PTCs in area where weight and size are critical. The miniaturization of PTCs is not a straightforward matter, however, because several scale-sensitive phenomena tend to deteriorate the performance of PTCs as their size is reduced. In this section the results of a preliminary simulation-based assessment of the effect of

miniaturization on the performance of an ITPTC is reported. The objective is to show that a simple uniform size reduction of all the major components of a PTC is unlikely to lead to a properly functioning PTC. The preliminary nature of the study should be emphasized, since a proper miniaturization of a PTC system requires in-depth study of all important component level processes. CFD-assisted ITPTC models were thus developed and simulated for the assessment of system level performance based on ITPTC component miniaturization. The model MOD1 appearing in [44-46], which had a total fluid volume of approximately 80 cc is chosen as a baseline model. Using this model as the basis, a series of system miniaturizations were performed. The simulations addressed scaled-down versions of the MOD1 ITPTC system, using the linear scaling feature in Fluent. The scaled-down models represented a total volume of approximately 40 cc (M80BL), 10cc (M50BL), and 0.7 cc (M20BL), respectively. These systems thus represented scaled-down replicas of the MOD1 system with length and diameter of 80 %, 50 % and 20 % of the original MOD1 system dimensions. The simulations were all transient, and started from a uniform temperature of 300 ^{o}K. Furthermore, everywhere the same operating conditions as the baseline model were used for the simulation of the miniature ITPTC models. The frequency in these simulations was 34 Hz everywhere. The cycle averaged CHX temperatures of the simulated miniature models and the baseline model are plotted with respect to time in figure C.2.

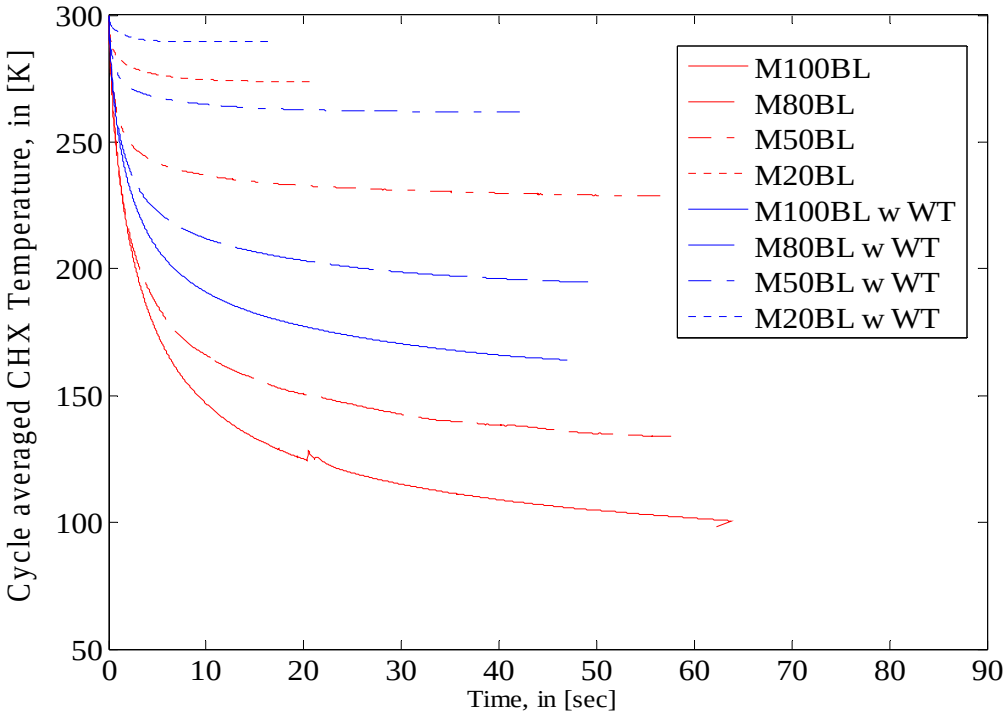

Figure C.2. Cycle-averaged CHX temperatures, in [^{o}K] for miniature ITPTC models.

Two groups of simulations were performed. In one group, the solid boundaries of the simulated ITPTCs were assumed to be adiabatic. Thus, heat conduction in the solid structures was neglected everywhere except for the porous matrix in the regenerator. The curves in figure 81 that are designated with M100BL, M80BL, etc., represent simulations where adiabatic boundary was assumed. In the second group of simulations, the pulse tube solid structure (aluminum) was included in the CFD analysis. The pulse tube and regenerator wall thicknesses were 0.2 mm in the baseline case. The wall thicknesses in the miniaturization simulations are listed in Table C.1.1. The nodalization of the solid wall was done using a similar meshing scheme as shown in Figure 37, and square meshing was applied to the additional regenerator and pulse tube walls. The curves designated with “M100BL WT”, “M80BL WT”, etc., represent simulations where solid conduction in the pulse tube and regenerator was included in the model. The reason why

heat conduction in the pulse tube and regenerator were modeled in a group of simulation is as follows. Axial heat conduction in the solid structures generally tends to deteriorate the performance of a PTC because it opposes the heat pumping. In commonly-applied PTCs, it is known that axial heat conduction effect is typically insignificant. In miniature scales, however, it may play an important role due to the very large axial temperature gradients. Let us consider the simulations that did not include conduction in the solid walls. According to results shown in Figure C.2, it is clear that simple, linear component miniaturizations will lead to significant system level performance deteriorations. As the total volume is reduced the steady periodic CHX temperatures tend to settle at higher temperatures than the baseline temperature (M100BL). The M80BL case, which represents a 20% linear reduction in all component dimensions so that only 50% overall system volume reduction is achieved, shows only relatively small deterioration in cooling capability in comparison with the baseline case. The cycle-averaged CHX temperature at quasi steady periodic condition is 134 ^{o}K for this case. The CHX temperature for the M20BL model, however, settles near 273 ^{o}K, thus producing very little cooling. Similarly, for the M50BL case the cycle-average CHX temperature reached a near steady periodic temperature of 229 ^{o}K. Although the cooling in this case is much better than the M20BL case, it is not sufficient for common cryocooler applications.

We will now discuss the result of simulations where axial conduction in the pulse tube and regenerator walls was included. As mentioned above, in typical sized cryocoolers a number of parasitic effects such as axial heat conduction in the component walls are at least an order of magnitude smaller than the net enthalpy flow in the pulse tube. As a result, cryogenic cooling and cryogenic temperatures are easily achieved at the

cold finger of these systems. However, as system components get miniaturized the axial heat conduction through the regenerator and pulse tube walls could potentially grow and reach the same order of magnitude as the net enthalpy flow in the pulse tube. The growth of the conduction heat transfer rate will deteriorate the system thermal performance, and will make the system completely ineffective once it becomes comparable in magnitude with the enthalpy flow rate. Thus, the previously-discussed simulated miniature systems models were remodeled, this time with wall thicknesses and heat conduction. The wall heat conduction was only modeled in the regenerator and pulse tube components, however, due to the presence of large temperature gradients in these components. The results of the simulation with wall thicknesses are shown in figure 81 and in Table C.2. with "WT" designation.

Table C.2. Miniature ITPTC model simulation results and their total volumes

Model index	Total volume, [cc]	CHX Temperature, in [^{o}K]
M100BL	~80	98
M80BL	~40	134
M50BL	~10	229
M20BL	~0.7	273
M100BL WT	~80	164
M80BL WT	~40	195
M50BL WT	~10	262
M20BL WT	~0.7	289

The results show that heat conduction in the pulse tube and regenerator walls has a significant impact on the system level performance. According to Table C.2 the inclusion of wall heat conduction resulted in an increase of about 66 degree Kelvin in the temperature of the cold end of the baseline system. The magnitude of the cold end

temperature increase is smaller for the smaller simulated systems. However, one should note that the much smaller total cooling is achieved as the ITPTC overall size is reduced, to begin with. Thus, the relative deterioration of performance caused by the parasitic heat conduction in the walls actually grows with size reduction. The above simulation results clearly suggest that a uniform size reduction of current PTCs while their overall layout and design features are maintained is not the right way for miniaturizing PTCs, since such a linear and uniform size reduction only lead to increasingly larger parasitic losses and adverse thermal effects which tend to deteriorate the performance of the PTC. Miniaturization of PTCs thus requires careful optimization with respect to component sizes and aspect ratios, frequency, charging pressure, and other relevant parameters. It may also require consideration of novel ideas for mitigating the fundamental processes that tend to deteriorate the heat pumping effects as the PTC size is reduced, and consideration of new and out of the box component and system configuration.

C.3. System Level Performance Conclusion of Miniature ITPTC

Preliminary simulations were performed in order to examine the effect of simple linear miniaturization on the performance of ITPTCs. A well-tested ITPTC system was used as the baseline case, and the effect of size reduction on the system's performance was tested. As the total volume of ITPTC cooler was reduced using component miniaturization the system's overall performance significantly deteriorated. The smallest ITPTC system, which represented a reduction of all dimensions of the baseline system by a factor of five, had a total a fluid volume of 0.7 cc. This system only reached a steady periodic CHX temperature of 273 ^{o}K. It thus was unable to even approach cryogenic temperatures. It must be emphasized, however, that the size reduction method here was

overly simple. Obviously the size reduction must be accompanied with detailed optimization for better cooling performance. However, the ITPTC system with a total volume of 40 cc showed some promising results by nearly reaching a steady periodic CHX temperature of approximately 130 ^{o}K. These simple miniaturization study indicate that size reduction of PTCs, while in principle possible, requires careful assessment of system and component-level scale-sensitive phenomena.

APPENDIX D

HOT WIRE ANEMOMETER CALIBRTION FOR VELOCITY MEASUREMENT

A hot wire anemometer calibration was performed using a mass flow meter, two DC pressure transducers, a DAQ, fine hot wire probe, and a constant temperature anemometer. Steady pressure drop test apparatus flow loop was used to calibrate the hot wire probe.

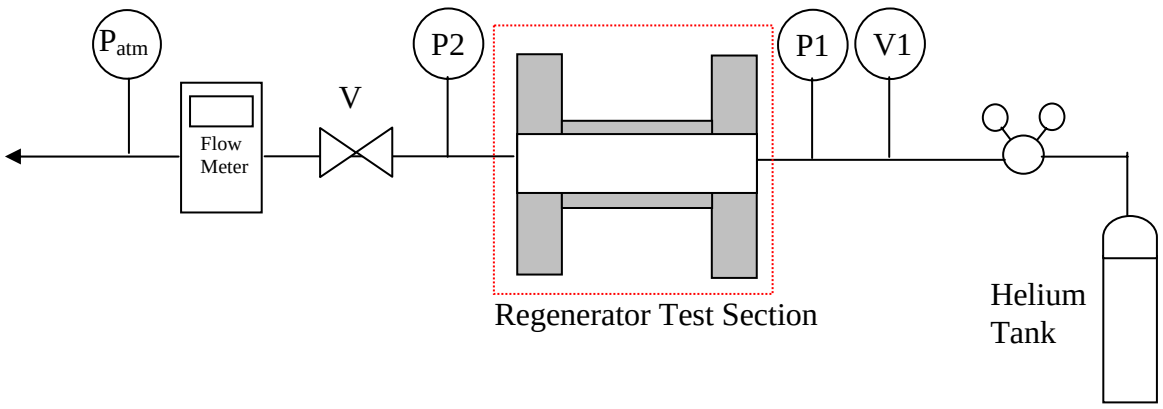

Figure D.1. Schematic of hot wire calibration test apparatus.

Anemometer calibration was conducted by varying the steady state mass flow rate with valve V, starting from a very low value and increasing the flow rate by increments, and measuring the pressure at P1 and the velocity voltage at V1. The measured mass flow rate was then converted to velocity through the local density relationship at P1. As a result, velocity to voltage relationship is obtained. Maximum Velocity of 11 m/s was obtained using 400 psig supply pressure. If supply pressure is set to much lower pressure then

maximum velocity up 50 m/s could be achieved using this calibration setup. The velocity versus velocity transducer voltage output curve is shown in Figure D2. A polynomial regression fit was applied to the calibration curve and velocity was represented as a function of voltage. This function was then implemented into the DAQ program to measure the local instantaneous velocities.

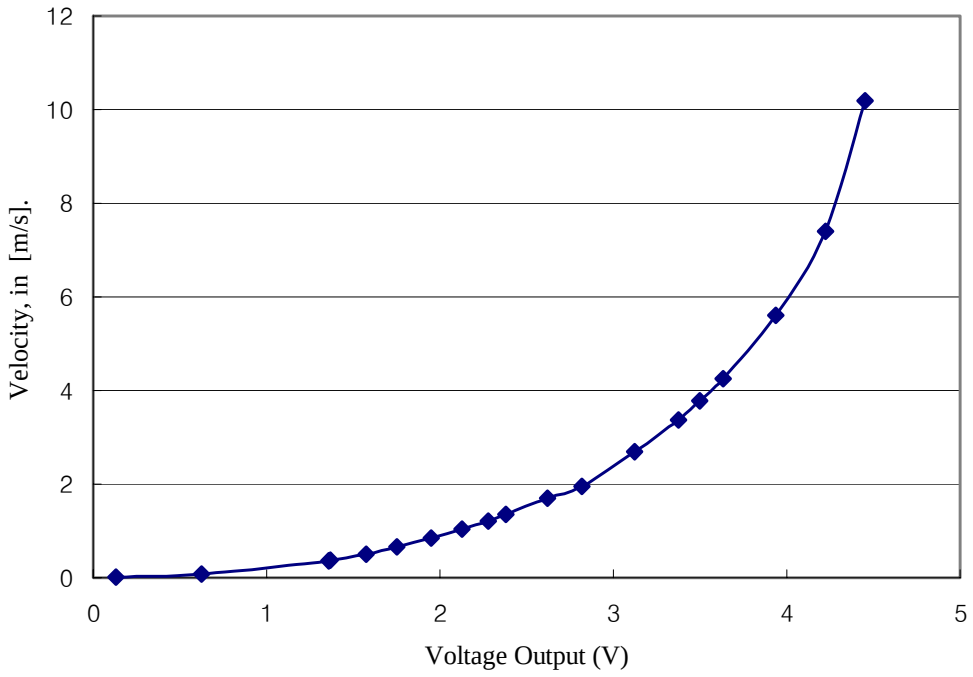

Figure D.2. Hot Wire Anemometer calibration curve for axial velocity measurement.

APPENDIX E

SENSIVITY ANALYSIS FOR HYDRODYNAMIC PARAMETERS

E.1 Sensitivity and uniqueness analysis of hydrodynamic parameters

The uniqueness and sensitivity of the hydrodynamic parameter values reported in Table 19 is described and presented. For the SS 325 mesh, series of periodic flow simulations at 60 Hz frequency were conducted for nine different combinations of viscous resistance coefficient, β and inertial resistance coefficient, C. The nine combinations of β and C were created by changing the values of coefficients by +/- 25% from its original (100%) reported values in Table 19. For each of these simulations the percent deviation or error (E) between the simulated pressure drop and measured pressure drop are calculated, and these calculated values are shown in Table E.1 and Figure E.1

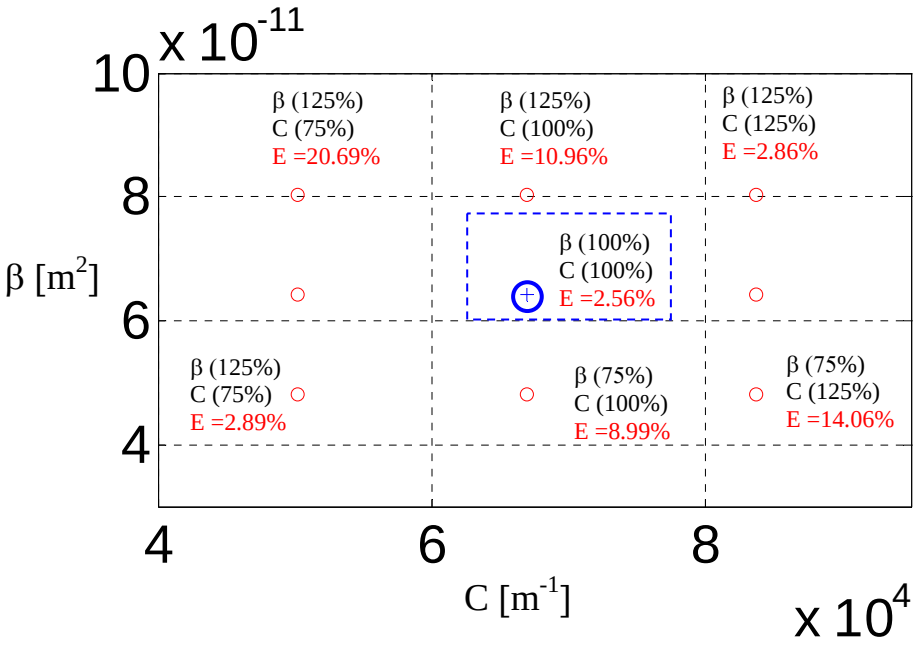

Figure E.1. Percent deviation between simulated and measured pressure drop for 325 mesh regenerator varying hydrodynamic parameters, β [m^2] and C [1/m].

Table E.1. Percent deviation error (E) between model and measured pressure drop for SS 325 mesh screen filler at 60 Hz frequency.

Varying β and C by +/- 25% from 100%	β (75%) 4.82E-11	β (100%) 6.42E-11	β (125%) 8.03E-11
C(75%)= 50250 [1/m]	2.89%	10.96%	20.69%
C(100%)= 67000 [1/m]	8.99%	⊕2.56%	10.60%
C(125%)= 83750 [1/m]	14.06%	4.00%	2.86%

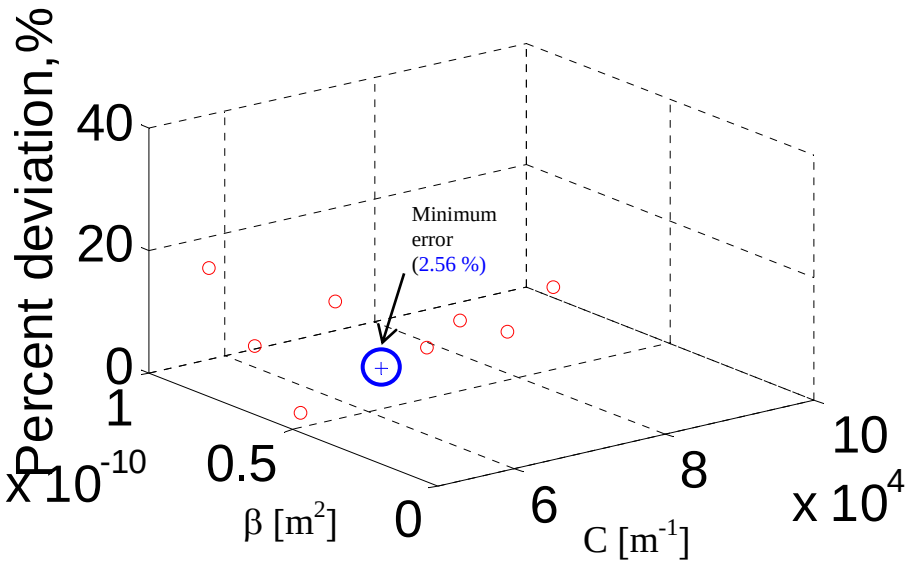

Figure E.2. Percent deviation between simulated and measured pressure drop for 325 mesh regenerator varying hydrodynamic parameters, β [m^2] and C [1/m].

The simulation results using the values of β = 6.42e-11 [m^2] (100%) and C = 67000 [1/m] (100%) in Table E.1. which represents obtained hydrodynamic parameters for 325 mesh, showed smallest percent deviation error (2.56%) among all the simulated combination of β and C. This further confirms that the values of β and C reported in Table 19 are the most accurate prediction of empirically obtained hydrodynamic parameters compare to other hydrodynamic parameter combinations.

Sensitivity of these parameters can also be seen through Table E.1 and Figure E.1. For the sensitivity of inertial resistance coefficient C, we fixed the value of β to 6.42e-11 [m^2] (100%) and only adjusted coefficient parameter C, by +/- 25% from its initial value of 67000 [1/m]. For the viscous resistance coefficient β the value of C was kept constant and value of β was only adjusted by +/-25%. The 25% change in hydrodynamic parameter values of β and C resulted in maximum solution change of about 7%.

REFERENCES

[1] Harvey, J. P. 2003. *Oscillatory Compressible Flow and Heat Transfer in Porous Media – Application to Cryocooler Regenerators*. Ph.D. Thesis, Georgia Institute of Technology, Atlanta, Ga.

[2] Radebaugh R. 2000. *Pulse Tube Cryocoolers for Cooling Infrared Sensors*. Proceedings of SPIE, The International Society for Optical Engineering, Infrared Technology, and Applications XXVI, Vol. 4130, pp. 363-379.

[3] Dunmire H. 1998.*U.S. Army Cryocooler Status Update, Military and Commercial Applications for Low Cost Cryocoolers*, San Diego, 1/1998, Electronic Industries Association (EIA), Arlington, VA.

[4] Gifford, W. E. and Longsworth, R. C. 1963. *Pulse-Tube Refrigeration*. ASME paper No. 63-WA-290 presented at Winter Annual Meeting of the American Society of Mechanical Engineers, Philadelphia, Pennsylvania (November 17-22).

[5] Harvey, J. P. 1999. *Parametric study of cryocooler regenerator performance*. Master's Thesis, Georgia Institute of Technology, Atlanta, Ga.

[6] Mikulin, E. I., Tarasov, A. A., and Shrebyonock, M. P. 1984. *Low-temperature expansion pulse tubes*. Advances in Cryogenic Engineering, Vol. 29, 629.

[7] Ross, R.G. 1997. *Cryocoolers 9*. Plenum Press, New York

[8] Ackermann, R. A. 1997. *Cryogenic Regenerative Heat Exchangers*. Plenum Press, New York.

[9] Roach, P. R. and Kashani, A. 1998. *Pulse tube cryocoolers with an Inertance tube: Theory, Modeling and Practice*. Advances in Cryogenics Engineering, Vol. 43, Plenum Press, New York, 1895-1902.

[10] Ochoa-tapia, J. and Whitaker, S. 1997.*Heat transfer at the boundary between a porous medium and a homogeneous fluid*. Int. J. Heat and Mass Transfer. Vol 40, No 11, pp. 2691-2707.

[11] Ochoa-tapia, J. and Whitaker, S. 1995. *Momentum transfer at the boundary between a porous medium and a homogeneous fluid – I. theoretical development*. International Journal of heat and Mass Transfer, Vol. 38, No. 14, 2635-2646.

[12] Ochoa-tapia, J. and Whitaker, S.1995. *Momentum transfer at the boundary between a porous medium and a homogeneous fluid-II. Comparison with experiment*. Int. J. Heat and Mass Transfer. Vol 38, No 14, pp. 2647-2655.

[13] Whitaker, S.1999. *The Method of Volume Averaging*. Kluwer Academic, Dordrecht.

[14] Whitaker 1996. *The Forchheimer equation: a theoretical development*. Transport in Porous Media, Vol. 25, Kluwer Academic Publishers, Netherlands, 27-61.

[15] Kaviany, M. 1995. *Principles of heat transfer in porous media*. New York: Springer-Verlag.

[16] Whitaker, S. 1967. *Diffusion and dispersion in porous media*. AIChE Journal, Vol. 13, No. 3, 420.

[17] Whitaker, S. 1973. The *transport equations for multi-phase systems*. Chemical Engineering Science, Vol. 28, 139.

[18] Ju, Y., Jiang, Y., and Zhou, Y. 1998. *Experimental study of the oscillating flow characteristics for a regenerator in a pulse tube cryocooler*, Cryogenics, Vol. 38, pp. 649-656.

[19] Kuwahara, F., Nakayama, A., and Koyama, H. 1996. *A numerical Study of Thermal Dispersion in Porous Media.* Journal of Heat Transfer. Vol. 118, pp. 756-761.

[20] Patankar, S. and Spalding, D. 1972. *A Calculation Procedure for Heat Mass and Momentum Transfer in Three-Dimensional Parabolic Flows* Int. J. Heat Mass Transfer, Vol. 15, pp. 1787-1806.

[21] Nakayama A., Kuwahara, F., Umemoto, T., Hayashi, T. 2002. *Heat and Fluid Flow Within an Anisotropic Porous Medium, Journal of Heat Transfer,* Vol. 124, pp. 746-753.

[22] Forchheimer, P.H. 1901. *Wasserbewegung durch Boden*. Z. Ver. Dtsch. Ing., 45,pp. 1782-1788.

[23] Gedeon, D. and Wood, J. 1997. *Oscillatory-flow Regenerator Test Rig: Hardware and Theory with Derived Correlations for Screens and Felts.* NASA Contractor Report 198442.

[24] Jeong, S., Nam, K. and Jung, J. 2002. *Regenerator Characterization under Oscillating Flow and Pulsating Pressure.* Cryocoolers 12. pp. 531-537.

[25] Nam K. and Jeong S. 2002. *Experimental Study on the Regenerator under Actual Operating Conditions*. Advances in Cryogenic Engineering. Vol. 47. pp. 977-984.

[26] Roberts, T. and Desai P. 2004. *Working Fluid State Properties Measurements in Medium and High Frequency Cryocoolers*. Advances in Cryogenincs 49. pp. 1146-53.

[27] Hsu C. T., Fu H. 2004, *Measurements of Pressure Drop of High Frequency Oscillating Flows through a Packed Column*, (in manuscript).

[28] Gary, J. O'Gallagher, A. and Radebaugh, R. 1994. A Numerical Model for Regenerator Performance, Technical Report, NIST-Boulder.

[29] Ward, W.C. and Swift, G.W. 1994. Design Environment for Low Amplitude Thermoacoustic Engines. J. Acoustic. Soc. Am, Vol. 95: pp. 3671.

[30] Kashani, A. and Roach, P. 1997. *A Simple Modeling Program for Orifice Pulse Tube Coolers. Cryocooler 9,* Plenum Press, New York, 327.

[31] Kashani, A. and Roach, P. 1998. *An Optimization Program for Modeling Pulse Tube Cryocoolers*. *Advances in Cryogenics Engineering,* Vol. 43, 1903.

[32] Ju, Y. L., Wang, C., and Zhou, Y. 1998. *Numerical simulation and Experimental Verification of the Oscillating Flow in Pulse Tube refrigerator*. *Cryogenics*, Vol. 38, 169-176.

[33] Gedeon, D. 1999. *Sage Pulse Tube Model-Class Reference Guide,* Gedeon Associates.

[34] Harvey J, Kirkconnell C, Desai P. 2003. *Comparison of Entropy Generation Rates in Various Stirling-Class Cryocooler Configurations*. Proceedings of the International Cryogenics Engineering Conference, September, p.1519-1526.

[35] Hsu C.T., Fu, H.L, and Cheng P. 1999. *On Pressure Velocity Correlation of Steady and Oscillating Flows in Regenerators made of wire-screens*. ASME J. Fluid Engineering 121:52-56.

[36] Hsu C.T. 2005. *Dynamic Modeling of Convective Heat Transfer in Porous Media*. In: K. Vafai, ed., Hand Book of Porous Media 2nd Edition, pp.39-80.

[37] Tanaka, M., Yamasihita, I., Chisaka, F., JSME International Journal of Series II, 33, pp. 283-289- (1990).

[38] Zhao, T.S. and Cheng P., Cryogenics, 36, 1998. pp. 1619-1626.

[39] Rawlins, W. 1992. *The Measurement and Modeling of Regenerator Performance in an Orifice Pulse Tube Refrigerator*, PhD Thesis, University of Colorado, Boulder.

[40] Radebaugh, R. Gary, J., Marquardt, E., Louie, B. Daney, D., Arp, V., and Linenberger, D. 1992. Measurement and Calculation of Regenerator Ineffectiveness for Temperatures of 5 to 40 K, Wright Laboratory, WPAAFB, OH, USA WL-TR-92-3074.

[41] Clearman W.M. 2007. *Measurement and Correlation of Directional Permeability and Forchheimer's Inertial Coefficient of Micro Porous Structures Used in Pulse – Tube Cryocoolers*. Masters Thesis, Georgia Institute of Technology, Atlanta, Ga.

[42] Fluent INC. 2003. *Fluent 6 User Manual*. pp. 8-1.

[43] Fluent INC. 2003. *Gambit User Manual*.

[44] Cha, J. S. 2004. *CFD Simulations of Multi-Dimensional Effects in an Inertance Tube Pulse Tube Cryocoolers.* Masters Thesis, Georgia Institute of Technology, Atlanta, Ga.

[45] Cha, J., Ghiaasiaan, S., Desai, P., Harvey, J., and Kirkconnell, C. 2006. *Multi-Dimensional Effects in Pulse Tube Refrigerators.* Journal of Cryogenics. Vol. 46, pp 658-665.

[46] Cha, J., Ghiaasiaan, S., Harvey, J., Desai, P., and Kirkconnell, C. 2004. *CFD Simulation of Multi-Dimensional Effects in an Inertance Tube Pulse Tube Refrigerator*. *Cryocooler 13*. pp. 285-292.

[47] Cha, J., Ghiaasiaan, S., Desai. P. 2005. *Measurement and Correlation of Anisotropic Hydrodynamic Parameters of Pulse Tube Cryocooler Regenerators*. Advances in Cryogenics Engineering, Vol. 51. pp. 1911-1918.

[48] Kuwahara F. and Nakayama A. 2005. *Three Dimensional Flow and Heat Transfer within Highly Anisotropic Porous Media, Numerical Determination of Permeability Tensor, Inertial Tensor, and Interfacial Heat Transfer Coefficient.* In: K. Vafai, ed., Hand Book of Porous Media 2nd Edition, pp.235-265.

[49] Nakayama A., Kuwahara F., Kawamura Y., and Koyama, H. 1995. *Three Dimensional Numerical Simulation of Flow Through a Microscopic Porous Structure.* Proceedings of ASME/JSME Thermal Engineering Conference, Hawaii, Vol.3, pp. 319-318.

[50] Nakayama A., Kuwahara F. 2000. *Numerical Modeling of Convective Heat Transfer in Porous Media using Microscopic Structures*. In: K. Vafai, ed., Hand Book of Porous Media pp.441-488.